A Mathematical Study of Complex Oscillatory Behaviour in an Excitable Cell Model

Submitted by **Harun Baldemir,**
to the University of Exeter as a thesis for the degree of
Doctor of Philosophy in Mathematics, in **February 2018.**

I certify that all material in this thesis which is not my own work has been identified and that no material has previously been submitted and approved for the award of a degree by this or any other University.

Signature: . . . . . .

ABSTRACT

Inner hair cells (IHCs) are the actual sensory receptors in hearing. Immature IHCs generate spontaneous calcium-dependent action potentials. Changing the characteristic of the Ca^{2+} signals modulates the amplitude and duration of the action potentials in these cells. These spontaneous action potential firing patterns are thought to be important for the development of the auditory system. The aim of this thesis is to gain a deeper understanding of the electrical activity and calcium signalling during development of IHCs from a mathematical point of view.

A numerical bifurcation analysis is performed to delineate the relative contributions of the model parameters to the asymptotic behaviour of the model. In particular, we investigate the pattern of periodic solutions including single (normal) spiking, pseudo-plateau burstings and complex solutions using two-parameter sections of the parameter space.

We also demonstrate that a simplified (three-dimensional) model can generate similar dynamics as the original (four-dimensional) IHC model. This reduced model could be characterised by two fast and one slow or one fast and two slow variables depending on the parameters' choice. Hence, the mechanisms underlying the bursting dynamics and mixed mode oscillations in the model are studied applying 1-slow/2-fast and 2-slow/1-fast analysis, respectively.

ACKNOWLEDGEMENTS

Firstly, I would like to express my sincere gratitude to my supervisor, Prof. Krasimira Tsaneva-Atanasova, for her patient guidance, continuous support and invaluable advice throughout my PhD research. She gave me the opportunity to enter an exciting scientific field, Mathematical Biology, which was totally new to me. Without her guidance and support, this thesis would not have been possible. It was a real honour for me to study under her supervision.

Many thanks also to my second supervisor, Prof. Peter Ashwin, for his scientific advice, many insightful discussions and suggestions to improve my knowledge of nonlinear dynamical systems theory. He always encourages students to extend their knowledge based on their need. I would like to thank him for helping me organise a series of lectures on Mathematical Biology in the summer term 2014-2015.

I want to express my special thanks to Prof. Vadim N. Biktashev, Assoc. Prof. Jan Sieber and Dr. Joel Tabak for inspiring academic discussions. My appreciation also goes to all researchers and colleagues in CEMPS and the Living System Institute at the University of Exeter for creating such a delightful academic environment, especially Sohaib Talal Hasan, Saad Almuaddi, Lauric Ferrat, Harry Green, Paul Ritchie, Jennifer Creaser, Piotr Slowinski, Marinho Antunes Lopes, Kevin Doherty and many others.

I am indebted to many Turkish friends in Exeter for their wonderful friendship, care and the many social activities we had together which greatly helped me to manage my homesickness. I also would like to thank Ms. Jannettja Longyear for being such a

great host, for proof reading and helping me to improve my language skills.

Finally, I want to express my special thanks to my beloved parents, my brother and sisters for their sincere wishes, love and encouragement. Words cannot describe how grateful I am to my family for their prayers and good wishes during my years abroad.

TABLE OF CONTENTS

LIST OF TABLES

TABLE **Page**

LIST OF FIGURES

FIGURE **Page**

CHAPTER 1

INTRODUCTION

Inner hair cells (IHCs) are the actual sensory receptors in hearing. During development, IHCs generate spontaneous calcium-dependent action potentials [49, 63]. The Ca^{2+} signals in immature IHCs trigger neurotransmitter release that generates action potentials of auditory neurons [8, 39]. Changing the characteristic of the Ca^{2+} signals modulates the amplitude and duration of the action potentials in immature IHCs. These spontaneous action potential firing patterns in immature IHCs are thought to be important for the development of the auditory system such as tonotopic organisation, a spatial representation of sounds in the auditory system according to frequencies, and maturation of synaptic connections [35, 49].

In order to gain further insight into these earlier signaling in IHCs, a mathematical model, called the *IHC model*, was originally proposed in [90] taking into account the experimental data recorded from developing IHCs. In addition to the earlier studies [31, 90] of the IHC model, the aim of this thesis is to attain deeper knowledge of the electrical activity and Ca^{2+} signalling during development of IHCs from a mathematical point of view.

In this chapter, we briefly discuss the hearing process with a particular focus on the developing inner hair cells (IHCs). Prior to reviewing the IHC model, we also discuss earlier mathematical models to give an introduction to the fundamental aspects of mathematical modeling of excitable cells as well as techniques that are used to study the mechanisms underlying oscillatory dynamics of such models.

1.1 Hearing and Inner Hair Cells

In this section, we give an overview of the hearing process and physiology of the ear. We focus on the inner hair cells that are the actual sensory receptors in hearing and explain the differences between the physiology of mature and immature IHCs. We also discuss why immature IHCs demand special attention as a motivation for this thesis.

1.1.1 The Physiology of an Ear

Hearing is one of the major mammalian senses and the organ of hearing is the ear. An ear can be divided into three parts: the outer ear, the middle ear and the inner ear.

The **outer ear** consists of the *auricle*, or *pinna*, and the *external auditory meatus*, or the *ear canal*. Sound waves are collected and amplified by the auricle, and then travel through the ear canal [72]. These sound waves reach the *tympanic membrane*, or the *ear drum*, causing vibrations.

The ear drum is the border of the **middle ear**, which hosts the *auditory ossicles*. The role of the ossicle bones, namely the *malleus*, the *incus* and the *stapes*, is to transfer and amplify movements of the ear drum towards the inner ear. Therefore, incoming sound waves are converted into mechanical vibrations.

The **inner ear** consists of three parts; the *cochlea*, the *vestibule* and the *semicircular canals*. We will focus on the cochlea, where the mechanical vibrations of the ossicles are converted into fluid waves and neural signals, which are then passed to the brain.

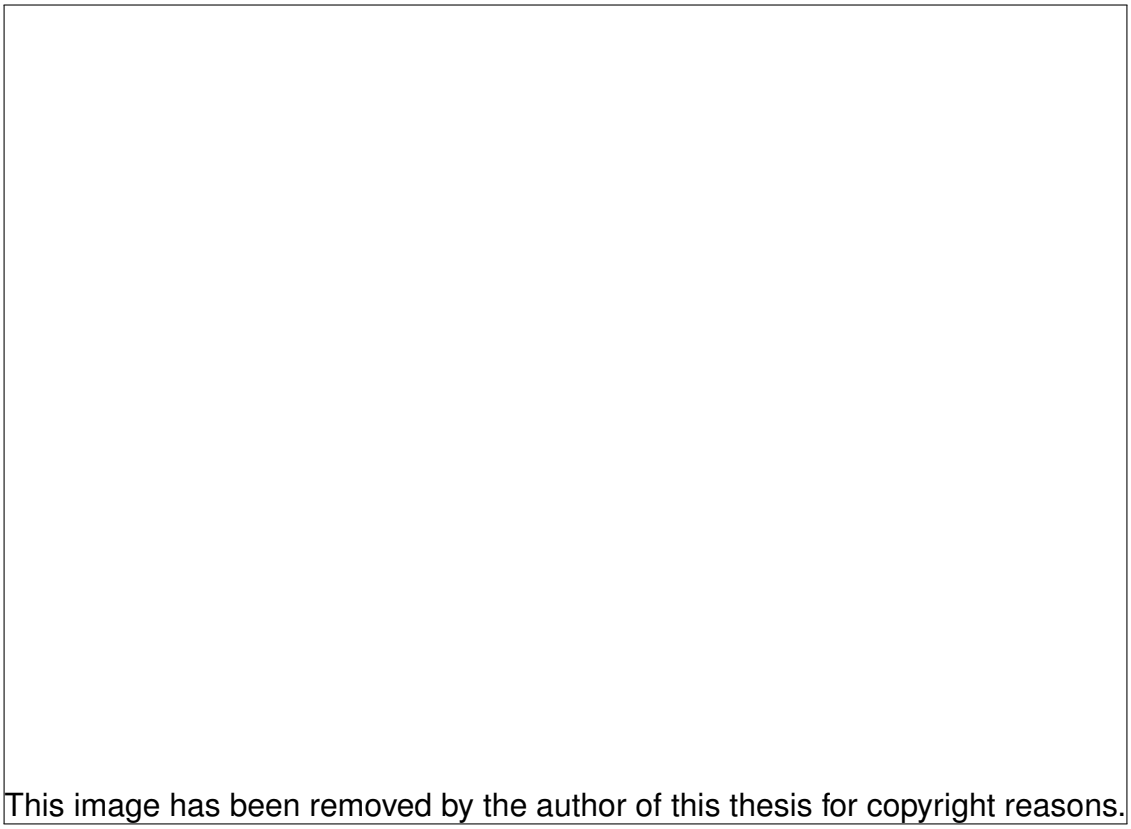

FIGURE 1.1. Structures of the cochlea, its cross section and the organ of Corti. Image from [76].

The cochlea in the inner ear is a fluid-filled, coil shaped organ (shown in Figure 1.1), which converts the mechanical vibrations of the ossicles into fluid waves. The cochlea consists of three fluid-filled chambers: the *scala vestibuli*, the *scala media* and the *scala tympani*, which are seen in the cross-section shown at the upper right corner of Figure 1.1. The scala vestibuli and scala tympani are separated by the *organ of Corti*, an illustration of which is depicted at the lower part of Figure 1.1.

The organ of Corti lies on the basilar membrane and continues along the entire cochlea. It consists of supporting cells and sensory cells (or hair cells). These sensory cells are organised as three rows of outer hair cells (OHCs) and one row of inner hair cells (IHCs), both of which are connected to the auditory nerves. Although the OHCs amplify mechanical vibrations, the IHCs are the actual sensory receptors mediating hearing

that are connected to the afferent nerves [76].

1.1.2 Action Potentials

Excitable cells such as neurons, muscle cells, endocrine cells and cochlear hair cells, display a transient change in their membrane potentials. These rapid changes are called *action potentials* or *spikes* [21]. We show a typical action potential trace of a neuron in Figure 1.2.

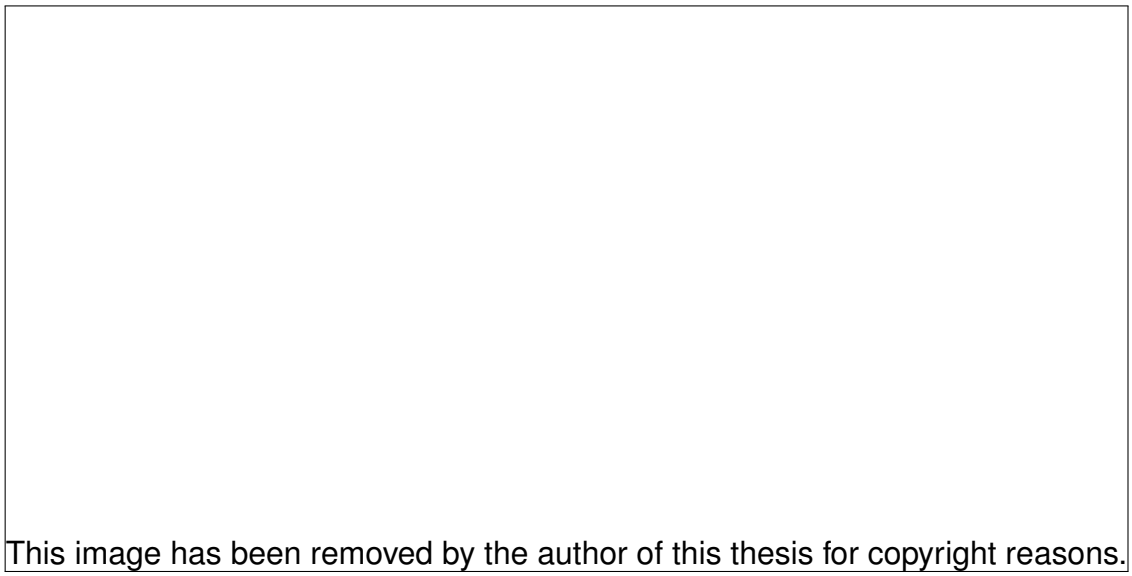

FIGURE 1.2. Sketch of an action potential. Image from [103].

The resting membrane voltage is about -70 mV, which describes the steady state of the cell. When the cell is at rest, the ion channels are closed and distributed across the membrane. The concentration of sodium (Na^+) ions outside the cell is greater than inside. Also, the concentration of potassium (K^+) ions inside the cell is greater than outside. The difference in charge is measured about -70 mV with the ions distributed across the membrane.

During an action potential, the membrane potential reaches a critical value called the threshold, which is about -55 mV. If the membrane potential does not reach this

critical level, then no action potential will fire. Once the membrane potential reaches the threshold, it increases rapidly from negative to positive due to the rapid influx of Na^+ from the extracellular environment into the cell through the voltage gated Na^+ channels. This is called depolarisation. Reaching the peak value, Na^+ channels begin to inactivate and K^+ channels open. Therefore, K^+ ions leave the cell which causes the membrane voltage to move back to its resting potential. This is known as repolarisation. After the peak of the action potential, the membrane becomes more negative than its resting potential for a brief moment. This portion of the action potential is called hyperpolarisation or the undershoot. After hyperpolarisation, the deactivation of K^+ channels restores the membrane potential from the undershoot to its resting potential.

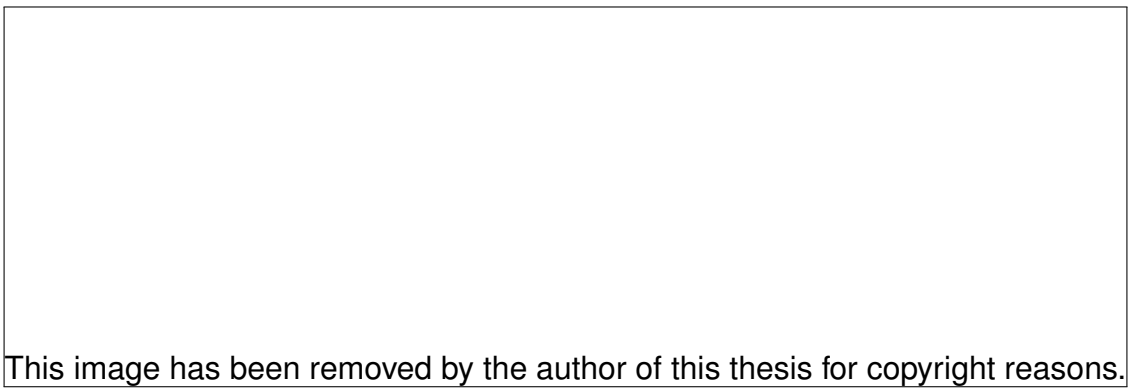

FIGURE 1.3. Electrical activity in the form of spiking (a) and bursting (b). Image from [100].

Excitable cells fire action potentials in the form of single (normal) spikes, bursts with several spikes and a mixed firing pattern, which is a combination of single spikes and bursts [31, 78, 90, 93]. We show two distinct patterns of action potentials in Figure 1.3. The first of which is generated in the single spike mode shown in Figure 1.3(a). Another typical pattern of electrical activity commonly seen in excitable cells is called *bursting* [78, 94, 99], which forms as a group of spikes. An example of a mixed firing pattern, where single spikes are interrupted by prolonged oscillations or bursts, is shown in Figure 1.5 in Section 1.1.4. This type of solution will be studied extensively throughout this thesis.

Bursting patterns are characterised by a transition between an active (depolarised) phase and a silent (repolarisation) phase (Figure 1.3(b)). Bursts are prolonged oscillations, which are more efficient than spikes in hormone and neurotransmitter release [14, 39]. Since different ionic mechanisms of bursting may result in different mathematical mechanisms, we will discuss the underlying mechanisms of different types of bursting in detail in Section 1.2.4.

1.1.3 Inner Hair Cells

IHCs are responsible for sound transduction since 90-95% of the afferent fibres of the auditory nerve connect to IHCs [61]. The mature IHC does not fire action potentials, which are the rapid rise and subsequent fall in the membrane potential in a characteristic pattern (see panel c in Figure 1.5). Since the organ of Corti lies on the basilar membrane, any movement of the basilar membrane causes a displacement of the organ of Corti. Therefore, *stereocillia* of the hair cells are deflected. Ion flows of IHCs are the result of the deflection of the MET channels. Opening the MET channels allows positively charged potassium (K^+) ions into the cell, which cause depolarisation i.e. the membrane potential becomes less negative. Due to the depolarisation, the voltage-gated calcium (Ca^{2+}) channels open resulting in a Ca^{2+} influx. This Ca^{2+} influx triggers neurotransmitter release from the basal end of the IHCs (see Figure 1.4) [34, 76]. Then, neurotransmitters bind to the receptors [27], which causes the generation of an action potential of the afferent nerve. Thus, the mechanical vibrations are converted into electrical signals to be sent to the brain.

In contrast to the mature IHCs, immature IHCs do not respond to sound but fire calcium-based action potentials close to the onset of hearing, which is around postnatal day 12 in mice [49, 63]. These action potentials trigger neurotransmitter release from the cells due to the Ca^{2+} influx [39]. Additionally, the Ca^{2+} influx into the cell cytosol activates Ca^{2+}-activated K^+ currents, which are expressed in immature IHCs [61, 62, 77].

It has been suggested that these spontaneous action potentials in immature IHCs are

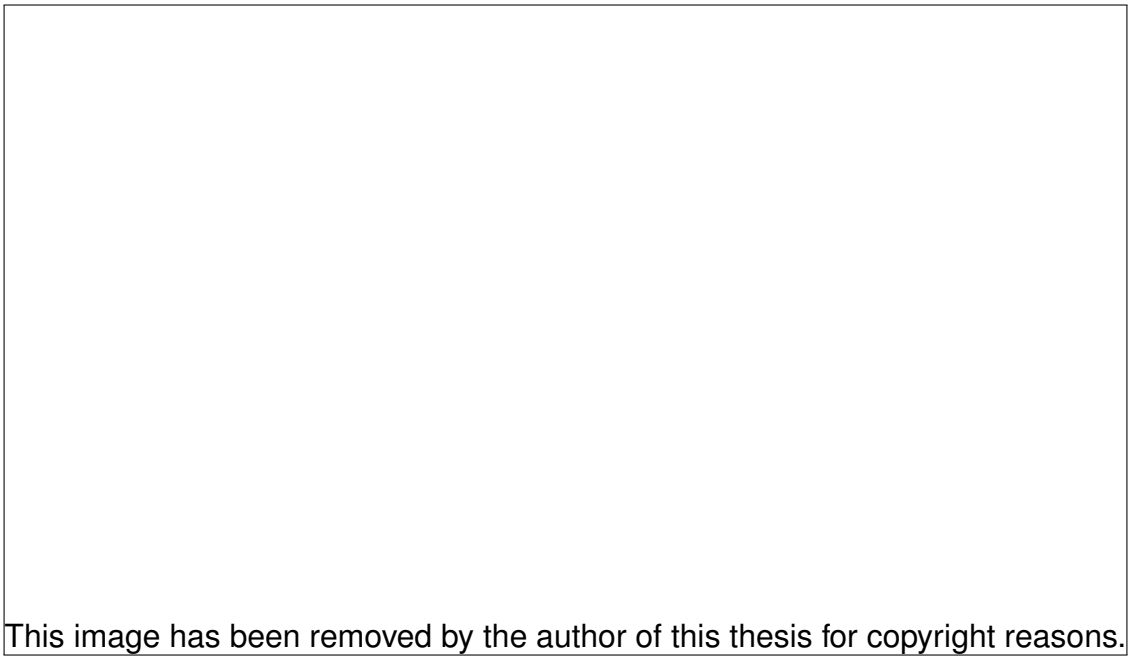

FIGURE 1.4. Structure of inner hair cells and function of the mechano-electrical transducer (MET) ion channels. Image from [76].

important for the development of the auditory system such as tonotopic organisation and maturation of synaptic connections [24, 35–37, 41, 49, 81, 97]. We will now discuss such action potentials in greater detail.

1.1.4 Ca^{2+}-based Action Potentials of Immature IHCs

Calcium is responsible for generating action potentials in Ca^{2+} the immature IHCs until the onset of hearing [49, 63]. When the membrane potential of these cells is constant and near its equilibrium value, Ca^{2+} channels of the immature IHCs are closed when the membrane potential is near its equilibrium. Additionally, Ca^{2+}-activated K^+ channels are closed due to the low intracellular Ca^{2+} concentration. During action potential firing [40, 98, 102], the membrane potential increases and the voltage-gated Ca^{2+} channels (VGCC) open which allows Ca^{2+} entry and release of neurotransmitters [8, 39]. In addition to the Ca^{2+} influx via VGCC, the level of the intracellular calcium ($[Ca^{2+}]_i$) is increased by the Ca^{2+} release from intracellular stores

such as endoplasmic reticulum (ER), which is know as Ca^{2+}-induced Ca^{2+} release (CICR), through ryanodine receptors (RyRs) [46]. The increase of $[Ca^{2+}]_i$ results in the activation of Ca^{2+}-activated K^+ (K_{Ca}) channels. This generates an outflow of K^+ ions. Additionally, the voltage-gated K^+ channels are activated by the change in membrane potential, which also generates an outflow of K^+ ions. Therefore, the IHCs repolarise due to the outflow of K^+ ions. During repolarisation, the voltage gated Ca^{2+} channels close and the levels of intracellular Ca^{2+} concentration and neurotransmitter release decreases.

These successive processes in immature IHCs described above result in oscillations on the membrane potential in different forms, such as single (normal) spikes, pseudo-plateau bursting and mixed type electrical activity (also called complex oscillations) [31, 90]. Prolonged action potentials that feature plateau oscillations are called pseudo-plateau bursting [87, 99], which differs notably from square wave bursting (also called plateau bursting) [87, 94], which is probably the most studied bursting form. For example, the active phase of square wave bursting is characterised by larger spikes, although it is characterised by smaller oscillations in pseudo-plateau bursting. Another characteristic of pseudo-plateau bursting is that it has a smaller number of oscillations and a shorter period than square wave bursting [94] (see Figure 1.9 for an example of these two types). We will discuss the square wave bursting and pseudo-plateau bursting in detail from the mathematical point of view in Section 1.2.4. Complex oscillations are another form of action potentials of immature IHCs. This mixed firing pattern is formed by the combination of single (normal) spikes and bursts with several small spikes (see the bottom panel in Figure 1.5). We will study this type of solution in greater detail throughout this thesis focusing on the underlying mechanism using dynamical systems theory.

The Ca^{2+} signals of immature IHCs trigger transmitter release that generates action potentials of auditory neurons [8, 39]. As seen in Figure 1.5, prolonged action potentials generate Ca^{2+} signals having larger amplitude and longer duration than normal action

FIGURE 1.5. Calcium signals during normal and prolonged action potential of immature IHCs. (a) Line-scan image taken through the basal pole (1 μm). Fluorescence indicates the changes in the intracellular calcium. Changes in fluorescence (ΔF) were used to estimate the effect of depolarising voltage commands on Ca^{2+}. (b) Analysis of fluore near the plasma membrane Ca^{2+} signals from the line-scan image. (c) Whole-cell current clamp simultaneous recording of membrane potential showing both brief and oscillating action potential waveforms. Image from [31].

potentials. Therefore, a greater amount of calcium entry results in a larger amount of neurotransmitter release [14, 39].

The pattern of action potentials in developing IHCs differs along the cochlea as the tonotopic frequency map develops [35, 61]. Therefore, the different firing patterns that are formed tonotopically could promote the tonotopic differentiation of auditory neural

circuits to and from the brain [37, 41, 55, 56, 66, 96]. Also, these early signalling events that occur during the development of IHCs are thought to be important in guiding and refining the initial stages of the auditory circuits [45] as observed in the visual system [10].

The changes in Ca^{2+} current amplitude and exocytic behavior during the development of IHCs cause changes in number and arrangement of presynaptic active zones of IHCs [8]. In particular, the action potential activity present in the developing IHCs is crucial for the maturation of their ribbon synapses [37] due to the major biological and functional refinements of the ribbon synapses during development from pre-hearing to hearing [105].

In order to gain further insight into the immature IHCs electrical activity and intracellular Ca^{2+} signalling, a mathematical model, called the *IHC model*, was originally developed in [90] based on experimental data obtained by recording various ion channel current found in immature IHCs [25, 38, 61–63, 108].

The IHC model [90] is of a specific type proposed by Chay and Keizer, the so-called the Chay-Keizer model [13], that represents a modification of the Hodgkin-Huxley model equations [30] including ionic currents and an additional equation to describe the intracelullar Ca^{2+} dynamics. Therefore, we will overview the Chay-Keizer model and summarise the primary findings, which will provide a basis to understand the IHC model equations and to analyse the dynamics of the oscillations of the IHC model.

1.2 Review of the Chay-Keizer Model

Since the IHC model is a specific type of the Chay-Keizer model, in this section we review the Chay-Keizer model [13], which is the first biophysical model of bursting electrical activity in pancreatic β-cells as the electrical activity in pancreatic β-cells is based on Ca^{2+} regulation as is the action potentials of the immature IHCs. In

Section 1.2.3, we also overview the Rinzel's slow-fast analysis [78, 79], a technique broadly used to study the underlying dynamics of different type of burstings [71, 78, 87, 91, 93, 94], which we apply to the IHC model in Chapter 4.

1.2.1 Description of the Chay-Keizer Model Equations

The Chay-Keizer model is an early minimal model due to the basic representation of the intracelullar Ca^{2+} dynamics and consisting of a few ionic currents. Over the years, other models have been proposed by modifying the Chay-Keizer model equations; including the addition of extra currents into the voltage equation [91], reducing the number of gating variables [78, 79] and more complicated Ca^{2+} dynamics due to new experimental findings [88]. These modifications were used to study different type of bursting activity [71, 93] and to understand the transition between them [87, 94]. The IHC model can also be considered as a modification of the Chay-Keizer model, which will be reviewed in Section 1.3.2.

Atwater et al. [3] proposed, based on their experimental results, that calcium dependent potassium channels (K_{Ca}) play a crucial role in the control of membrane porential in pancreatic β-cells. Chay and Keizer [13] developed a mathematical model to describe the interactions between ionic currents and intracellular calcium concentration of the pancreatic β-cells, generating the *bursting* electrical activity observed in experiments as shown in Figure 1.6.

Bursting is a specific firing pattern that is significantly different from regular spiking. A bursting consists of two phases; the *active phase* where the rapid spike-like consecutive oscillations (also called the *bursts*) occur and the *silent phase* that represents the quiescent time intervals between two sequential bursts (see Figure 1.6). From a mathematical point of view, bursting activity is characterised by the transitions between the active phase and the silent phase. Additionally, a regular bursting requires at least two timescales [47]. The repetitive oscillations during the active phase correspond to the passage of a trajectory near a manifold of periodic solutions of the fast subsystem

[84], which is obtained by considering the slowest variable as a constant. We will give an overview of the slow-fast analysis in Section 1.2.2. Bursting is usually caused by a slow process that can modulate fast spiking activity [32]. We now introduce the Chay-Keizer model [13] to review the mechanisms underlying the bursting pattern in Section 1.2.3.

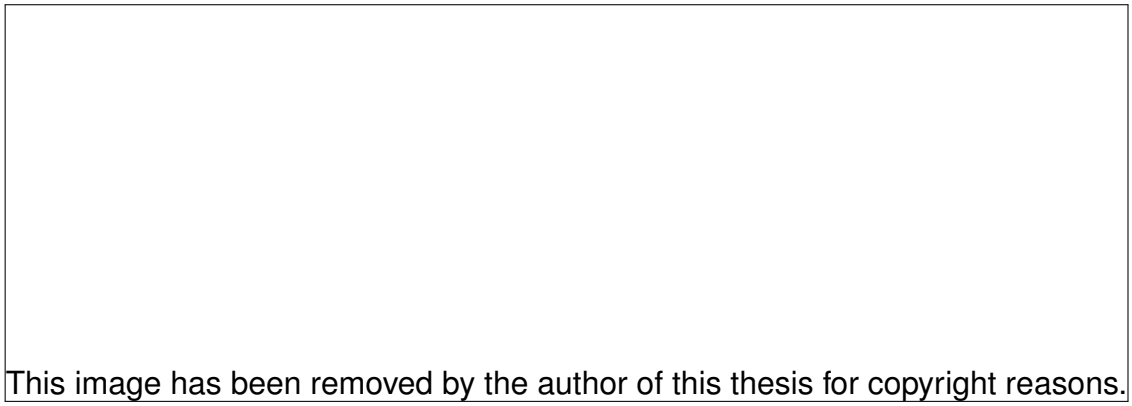

FIGURE 1.6. Experimental recording of the bursting electrical activity in pancreatic β-cells. Image from [65].

Chay and Keizer used the Hodgkin-Huxley model equations [30] as a basis for their minimal model because of the similarity of the membranes of different cells. Therefore, excitable cell membranes can be modelled using ionic current models introduced by Hodgkin and Huxley [65]. Additionally, they made three major modifications to the classical Hodgkin-Huxley model in order to take into account the dynamics of the intracellular Ca^{2+} concentration. These are:

- an inward sodium current (I_{Na}) was replaced by an inward calcium current (I_{Ca}),
- a calcium activated potassium current ($I_{\text{K}_{\text{Ca}}}$) was added,
- an ordinary differential equation (ODE) was also added to describe the dynamics of the intracellular calcium concentration.

The rate of change for the membrane potential (V_{m}) of the Chay-Keizer model satisfies

$$C_{\mathrm{m}}\frac{\mathrm{d}V_{\mathrm{m}}}{\mathrm{d}t} = -[I_{\mathrm{Ca}}(V_{\mathrm{m}},m,h) + I_{\mathrm{K}}(V_{\mathrm{m}},n) + I_{\mathrm{K_{Ca}}}(V_{\mathrm{m}},Ca) + I_{\mathrm{leak}}(V_{\mathrm{m}})] \tag{1.1}$$

where I_{Ca}, I_{K}, $I_{\mathrm{K_{Ca}}}$ and I_{leak} are the currents of the voltage-gated Ca^{2+} current, the voltage-gated K^+, Ca^{2+}-activated K^+ current and the leakage current, respectively.

Hodgkin and Huxley introduced the equation of the voltage-gated K^+ current as

$$I_{\mathrm{K}}(V_{\mathrm{m}},n) = \bar{g}_{\mathrm{K}} n^4 (V_{\mathrm{m}} - V_{\mathrm{K}}) \tag{1.2}$$

where V_{K} is the Nernst potential, $\bar{g}_{\mathrm{K}}$ is the maximum conductance and n is the activation variable of K^+ channel. The variable n obeys the differential equation

$$\frac{\mathrm{d}n}{\mathrm{d}t} = \frac{n_\infty(V_{\mathrm{m}}) - n}{\tau_{\mathrm{n}}(V_{\mathrm{m}})} \tag{1.3}$$

where

$$n_\infty(V_{\mathrm{m}}) = \frac{\alpha_n(V_{\mathrm{m}})}{\alpha_n(V_{\mathrm{m}}) + \beta_n(V_{\mathrm{m}})} \quad , \quad \tau_{\mathrm{n}}(V_{\mathrm{m}}) = \frac{1}{\alpha_n(V_{\mathrm{m}}) + \beta_n(V_{\mathrm{m}})} \tag{1.4}$$

The functions $n_\infty(V_{\mathrm{m}})$ and $\tau_{\mathrm{n}}(V_{\mathrm{m}})$ are in the same form as the Hodgkin-Huxley model but the voltage V_{m} is shifted by $V_{\mathrm{m}}^* = 30$ mV [30].

Chay and Keizer replaced the voltage-gated sodium current (I_{Na}) by the voltage-gated calcium current given as

$$I_{\mathrm{Ca}}(V_{\mathrm{m}},m,h) = \bar{g}_{\mathrm{Ca}} m^3 h (V_{\mathrm{m}} - V_{\mathrm{Ca}}) \tag{1.5}$$

where V_{Ca} is the Nernst potential, $\bar{g}_{\mathrm{Ca}}$ is the maximum conductance, m and h are the activation and inactivation variables of Ca^{2+} channel, respectively.

The calcium-activated potassium current ($I_{\mathrm{K_{Ca}}}$) was given by [73, 74]

$$I_{\mathrm{K_{Ca}}}(V_{\mathrm{m}},Ca) = \bar{g}_{\mathrm{K_{Ca}}} \frac{Ca}{K_d + Ca}(V_{\mathrm{m}} - V_{\mathrm{K}}) \tag{1.6}$$

where $\bar{g}_{\mathrm{K_{Ca}}}$ is the maximum conductance, K_d is the half maximal effective concentration of intracellular Ca^{2+} concentration (Ca).

The flow of other ions in the model was described by a leakage current given by

$$I_{\text{leak}}(V_{\text{m}}) = \bar{g}_{\text{leak}}(V_{\text{m}} - V_{\text{leak}}) \tag{1.7}$$

where the constant $\bar{g}_{\text{leak}}$ represents the maximal conductance.

The activation and inactivation variables m, h and n, satisfy the differential equations, which were originally introduced by Hodgkin and Huxley [30], given by

$$\frac{\text{d}X}{\text{d}t} = \frac{X_\infty(V_{\text{m}}) - X}{\tau_{\text{X}}(V_{\text{m}})} \quad \text{where} \quad X = \{m, h, n\} \tag{1.8}$$

In order to complete the Chay-Keizer model, there is one more ODE that describes the dynamics of the intracellular Ca^{2+} concentration. The regulation of the intracellular calcium concentration is represented by a balance equation and shows the difference between influx and efflux of calcium, given by

$$\frac{\text{d}Ca}{\text{d}t} = f\left(-k_1 I_{\text{Ca}}(V_{\text{m}}, m, h) - k_{\text{Ca}} Ca\right) \tag{1.9}$$

where f is the ratio of free to bound intracellular calcium ions, k_1 is a constant given by $\frac{-3}{4\pi r^3 F}$ where F is Faraday's constant, r is the radius of the cell and the factor 3 is obtained by the ratio between the surface and volume of the cell.

The influx of Ca^{2+} ions is represented by the voltage-gated Ca^{2+} current and the efflux of Ca^{2+} ions is given by $k_{\text{Ca}}Ca$, where k_{Ca} is the rate constant of Ca^{2+} removal from the cytoplasm. Although there are a variety of Ca^{2+} removal mechanism from the cell including the ATPase pumps, the Na^+ / Ca^{2+} exchange and the mitochondrial uptake of Ca^{2+}, the Ca^{2+} efflux in (1.9) was modelled linearly due to the lack of knowledge about calcium regulation at that time. Additionally, the behaviour of the Chay-Keizer model was studied for different values of k_{Ca}. They showed that as the value of the parameter k_{Ca} increases, the silent phase of the bursting becomes shorter while the active phase becomes longer [13].

The Chay-Keizer model is a five dimensional model given by the ODEs in (1.1), (1.8) and (1.9), which was orginally introduced in [13]. Additionally, the original Chay-

Keizer model was simplified by replacing the variables m and n, the activation and inactivation variables of Ca^{2+} channel, by their steady-state functions $m_\infty(V_\mathrm{m})$ and $n_\infty(V_\mathrm{m})$. Therefore, similar bursting can be captured by a model having fewer dynamic variables [78–80]. In Chapter 3, the original four-dimensional (4D) IHC model will also be simplified to a three-dimensional model, having the same dynamic variables, which are the membrane voltage V, the activation variable of K^+ channel n and the intracellular calcium concentration Ca, as the reduced Chay-Keizer model.

Since the ODEs of the variables m and n in (1.8) were eliminated, the reduced 3-dimensional Chay-Keizer model is given by

$$\begin{aligned} C_\mathrm{m}\frac{\mathrm{d}V_\mathrm{m}}{\mathrm{d}t} &= -[I_\mathrm{Ca}(V_\mathrm{m}) + I_\mathrm{K}(V_\mathrm{m}, n) + I_{\mathrm{K_{Ca}}}(V_\mathrm{m}, Ca) + I_\mathrm{leak}(V_\mathrm{m})] \\ \frac{\mathrm{d}n}{\mathrm{d}t} &= \lambda_n\left(\frac{n_\infty(V_\mathrm{m}) - n}{\tau_\mathrm{n}(V_\mathrm{m})}\right) \\ \frac{\mathrm{d}Ca}{\mathrm{d}t} &= f\left(-\alpha I_\mathrm{Ca}(V_\mathrm{m}) - k_\mathrm{Ca}Ca\right) \end{aligned} \tag{1.10}$$

where $I_\mathrm{Ca}(V_\mathrm{m}) = \bar{g}_\mathrm{Ca} m_\infty(V_\mathrm{m})^3 h_\infty(V_\mathrm{m})(V_\mathrm{m} - V_\mathrm{Ca})$. The model parameters and current activation/inactivation functions can be found in [79].

The reduced (3D) Chay-Keizer model, although having fewer state variables, shares similar dynamics with the original (5D) Chay-Keizer model. We plotted a time series of the membrane potential and intracellular calcium concentration of the reduced Chay-Keizer model in Figure 1.7. This shows the reduced model also produces similar bursting solutions as simulated by the original model (see Figure 1 in [13]). The underlying dynamics of such bursting was studied using a tecnique called *geometric singular perturbation analysis*, or *slow-fast analysis*, which will be reviewed in the following section.

1.2.2 Review of the Slow-Fast Analysis

In this section, we will give a general overview of the slow-fast analysis which we apply to the IHC model in Chapter 4.

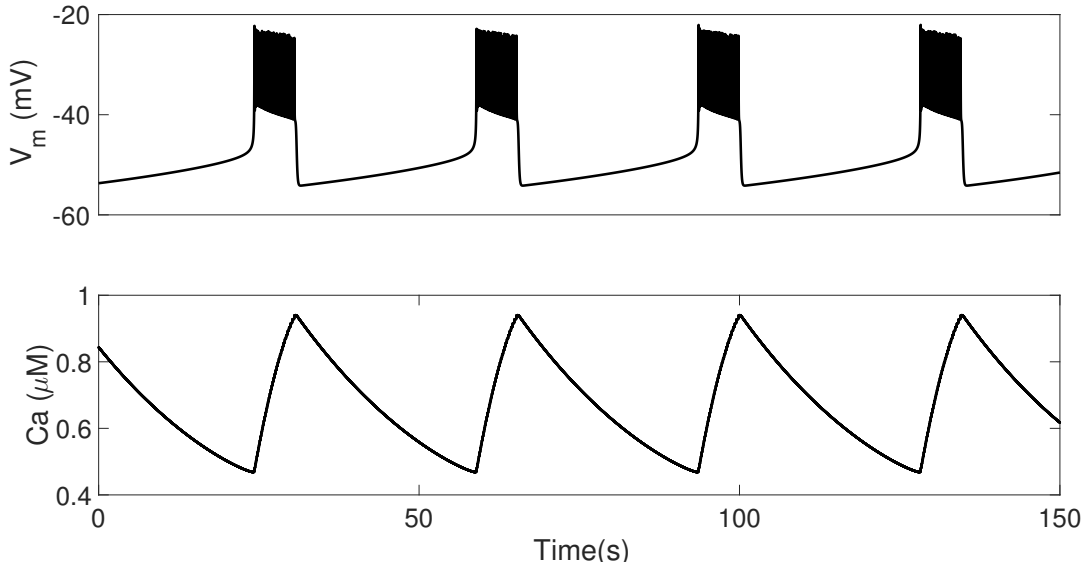

FIGURE 1.7. Reproduced numerical simulation of the reduced Chay-Keizer model with the given parameter by Rinzel in [79].

A *slow-fast system* is a system of ordinary differential equations (ODEs) that takes the form

$$\begin{aligned} \epsilon \frac{\mathrm{d}x}{\mathrm{d}\tau} &= f(x, y, \epsilon) \\ \frac{\mathrm{d}y}{\mathrm{d}\tau} &= g(x, y, \epsilon) \end{aligned} \tag{1.11}$$

where $(x, y) \in \mathbb{R}^m \times \mathbb{R}^n$ are the state variables, $f : \mathbb{R}^m \times \mathbb{R}^n \times \mathbb{R} \to \mathbb{R}^m$ and $f : \mathbb{R}^m \times \mathbb{R}^n \times \mathbb{R} \to \mathbb{R}^n$ and $0 < \epsilon \ll 1$. The small parameter ϵ represents the ratio of time scales. The variables x and y are called *fast* and *slow* variables, respectively. Setting $t = \tau/\epsilon$, the system in (1.11) becomes

$$\begin{aligned} \frac{\mathrm{d}x}{\mathrm{d}t} &= f(x, y, \epsilon) \\ \frac{\mathrm{d}y}{\mathrm{d}t} &= \epsilon g(x, y, \epsilon) \end{aligned} \tag{1.12}$$

We refer to τ as the *slow time* and t as the *fast time*.

In order to analyse a slow-fast system, we first consider the case $\epsilon \to 0$ in (1.11) and

(1.12) since $0 < \epsilon \ll 1$. Thus, setting $\epsilon = 0$ on the fast time in (1.12) gives

$$\begin{aligned} \frac{\mathrm{d}x}{\mathrm{d}t} &= f(x, y, \epsilon) \\ \frac{\mathrm{d}y}{\mathrm{d}t} &= 0 \end{aligned} \tag{1.13}$$

which is called the *fast subsystem* (or the *layer problem*) and the flow of the system in (1.13) is called the *fast flow* [16, 52].

On the other hand, setting $\epsilon = 0$ on the slow time in (1.11) gives

$$\begin{aligned} 0 &= f(x, y, \epsilon) \\ \frac{\mathrm{d}y}{\mathrm{d}\tau} &= g(x, y, \epsilon) \end{aligned} \tag{1.14}$$

which is called the *slow subsystem* (or *reduced problem*) and the flow of the system in (1.14) is called the *slow flow* [16, 52].

We note that the system in (1.14) is an ODE with an algebraic equation $f(x, y, 0) = 0$. Hence, we have a *differential-algebraic equation (DAE)*. The trajectories near the set given by $f(x, y, 0) = 0$ are described by the slow flow. The set defined by

$$S := \{(x, y) \in \mathbb{R}^m \times \mathbb{R}^n \quad | \quad f(x, y, 0) = 0\} \tag{1.15}$$

is called the *critical manifold*. It is clear that the points of the critical manifold S are the equilibrium points of the fast flow in (1.13) [52].

We will define the fast and slow subsystems of the IHC model in order to understand the behaviour of the model solutions according to the fast and slow flows of the corresponding subsystems in greater detail in Chapter 4.

1.2.3 The Slow-Fast Analysis of the Chay-Keizer Model

Rinzel [78, 79] described a theoretical treatment of the bursting phenomenon of the Chay-Keizer model. The fundamental idea of his analysis was to split the model into slow and fast subsystems due to the differences in time scales of the state variables.

Since the intracellular calcium concentration (Ca) evolves on a much slower time scale than the voltage membrane (V_{m}) and the activation variable of K^+ channel (n), Rinzel treated the variable Ca as a constant in the fast subsystem and performed a bifurcation analysis of the fast subsystem using Ca as the bifurcation parameter [78].

Applying the bifurcation analysis, Rinzel was able to describe how the fast subsystem dynamics depend on the changes of the slowest variable Ca. Additionally, the dynamics of the control parameter Ca were included in the understanding of the overall dynamics by superimposing the bursting solution on the fast subsystem bifurcation diagram. In Figure 1.8, we illustrate his qualitative analysis of bursting for the reduced Chay-Keizer model given by the system in (1.10).

In Figure 1.8(a), for illustrative purposes, we reproduce the bifurcation diagram originally computed by Rinzel [79]. The low and high membrane voltage (V_{m}) steady states are stable and are shown by blue solid curves. The middle branch (the dashed red curve) represents unstable steady states. At the supercritical Hopf bifurcation (HB), a family of stable periodic orbits emanates (the solid green curve). This branch terminates at a homoclinic bifurcation (HC) where the orbit connects the saddle equilibrium on the middle branch, which is between two saddle-node bifurcations, to itself, having an infinite period.

In the range of Ca values between SN_2 and HC, the fast subsystem exhibits *bistability* that are the lower stable steady states and stable periodic orbits. It was shown in Figure 1.8 that the membrane potential switches between low voltage to high voltage states i.e. between the silent to active phase during the bursting process. This activity can be better understood by superimposing the bursting solution onto the fast subsystem diagram, which is shown in Figure 1.8(b). When the bursting is in the silent phase, the trajectory follows the lower stable steady state (solid blue) curve. Additionally, since this happens under the *Ca* nullcline curve (i.e. $dCa/dt < 0$), Ca decreases until the saddle node bifurcation (SN_2). When the trajectory reaches SN_2, it switches to the

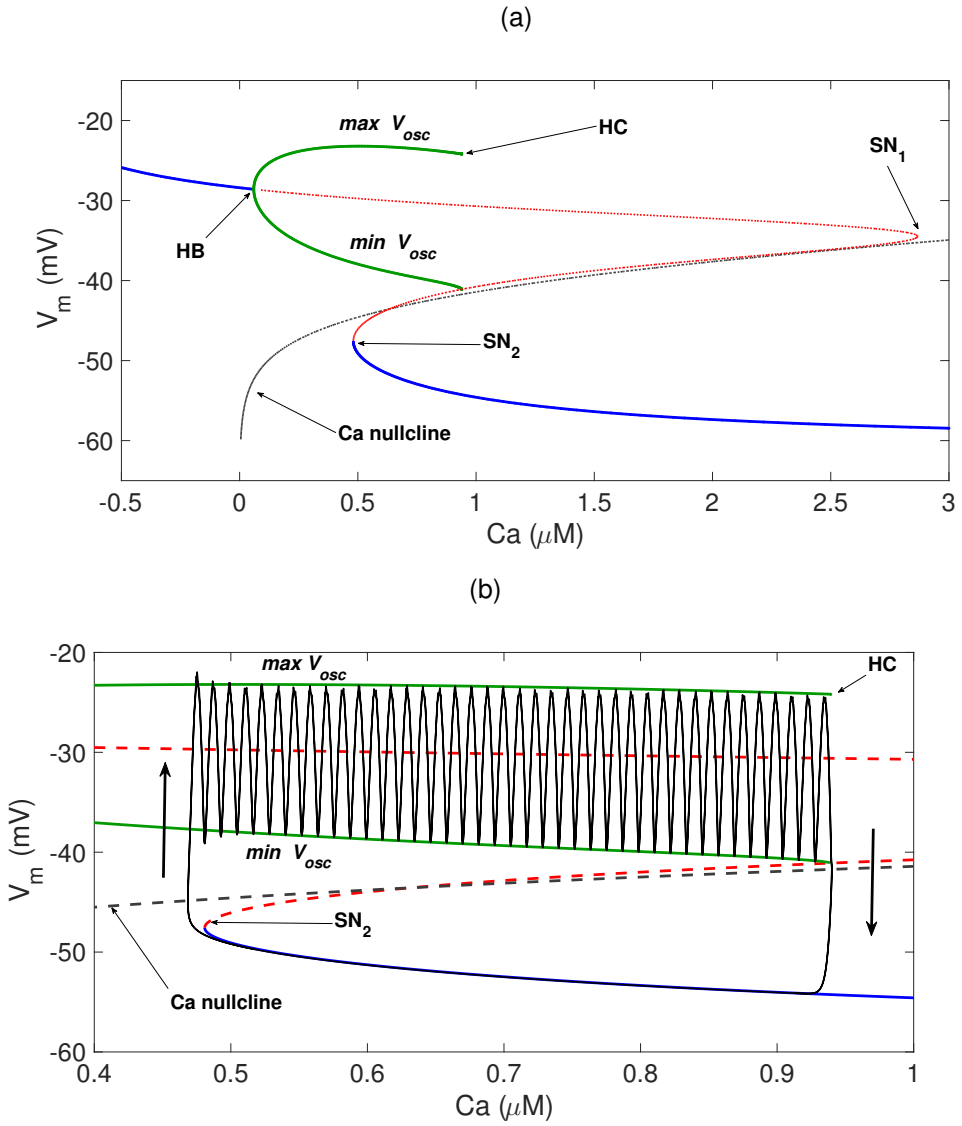

FIGURE 1.8. (a) Fast subsystem bifurcation diagram of the reduced Chay-Keizer model with the given parameters in [79]. (b) Projection of the solution shown in Figure 1.7 is superimposed. Solid blue lines represent stable equilibria and the dashed red line represents unstable equilibria. HB: Hopf bifurcation, HC: Homoclinic bifurcation, SN: Saddle-node bifurcation of equilibria. *max* V_{osc} and *min* V_{osc} is the maximum and minimum values of the voltage membrane of spiking oscillations, respectively. The *Ca* nullcline curve is computed by solving the equation $dCa/dt = 0$.

oscillatory region (the green curves). Since the trajectory crosses the *Ca* nullcline (i.e. $dCa/dt > 0$), Ca increases until the homoclinic bifurcation (HC), where the trajectory

switches back to the lower stable steady state, which completes the cycle.

The bursting of the Chay-Keizer model shown in Figure 1.7 is known as *square wave bursting* because the voltage amplitude profile during the active phase of bursting sometimes looks like a square (or *plateau bursting*) [94] and is classified mathematically as *fold-homoclinic* since the silent phase of the bursting ends at a fold bifurcation and the active phase ends at a homoclinic bifurcation [32]. However, the IHC model produces a different type of bursting, so called *pseudo-plateau bursting* [87, 99] (see Figure 1.5). In the following, we will review this type bursting, which can also be observed by modifying the Chay-Keizer model.

1.2.4 Pseudo-Plateau Bursting

Pseudo-plateau bursting differs notably from square wave bursting [87, 94]. Figure 1.9 shows an example of these two types. The active phase of the square wave bursting is characterised by larger spikes, which sometimes form the burst in a square-like shape. On the other hand, the active phase of the pseudo-plateau bursting is characterised by smaller oscillations. Another characteristic of pseudo-plateau burstings is that they have a smaller number of oscillations and a shorter period than square wave burstings [94].

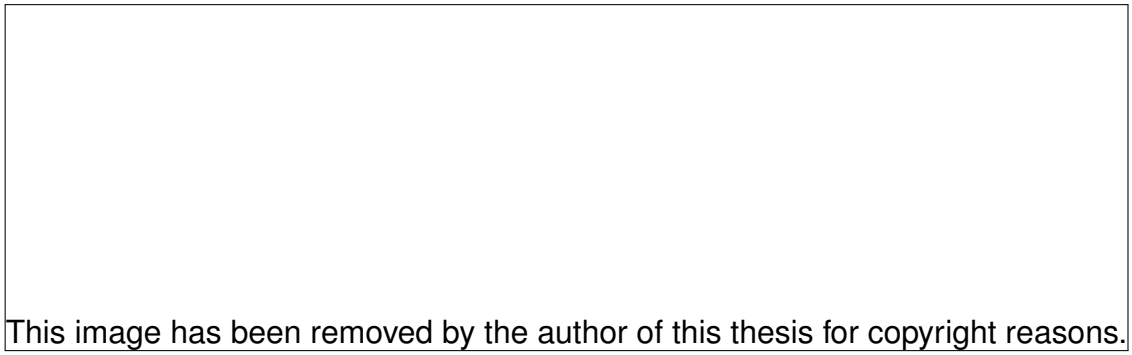

FIGURE 1.9. Experimental recording of pseudo-plateau (left) and plateau (right) burstings. Image from [93].

The original Chay-Keizer model that produced square wave bursting was modified to generate pseudo-plateau bursting [71, 87, 91]. Moreover, by changing some of the model parameters of the Chay-Keizer model [94], the transition between plateau and pseudo-plateau bursting was studied [87, 94]. These two class of burstings are distinguished by their fast subsystem bifurcation structures. From the fast subsystem structure of square wave bursting (see Figure 1.8(b)) to pseudo-plateau burstings, these changes can be observed [94]:

- The supercritical Hopf bifurcation becomes subcritical.
- The stable limit cycles disappear and the unstable limit cycle branch terminates at a homoclinic bifurcation.
- Bistability occurs between the upper and lower equilibrium branches.

Figure 1.10 shows the bursting oscillations of the modified Chay-Keizer model [94]. Increasing v_{n}, voltage value at the midpoint of the steady-state function of the activation variable of K^+ channel ($n_\infty(V)$), changes the criticality of the Hopf bifurcation. As shown in Figure 1.8(a), it is a supercritial Hopf bifurcation of the fast subsystem classified mathematically as fold-homoclinic which we discussed in the previous section [32]. However, when v_{n} increases, the Hopf becomes subcritical, which is a characteristic of pseudo-plateau burstings classified mathematically as *fold-subHopf* where the silent phase of the bursting ends at a fold bifurcation and the active phase ends at a subcritical Hopf bifurcation [32]. The parameter f, which represents the fraction of intracellular calcium that is unbound by buffers, controls the speed of the slow variable. As it is increased, the slow variable c becomes faster and pseudo-plateau bursting occurs.

The structure of the fast subsystem diagram shown in Figure 1.10 of the modified Chay-Keizer model [94] is different from the fast subsystem of the original Chay-Keizer model [13] (see Figure 1.8). In Figure 1.10, unstable limit cycles orginating from the subcritical

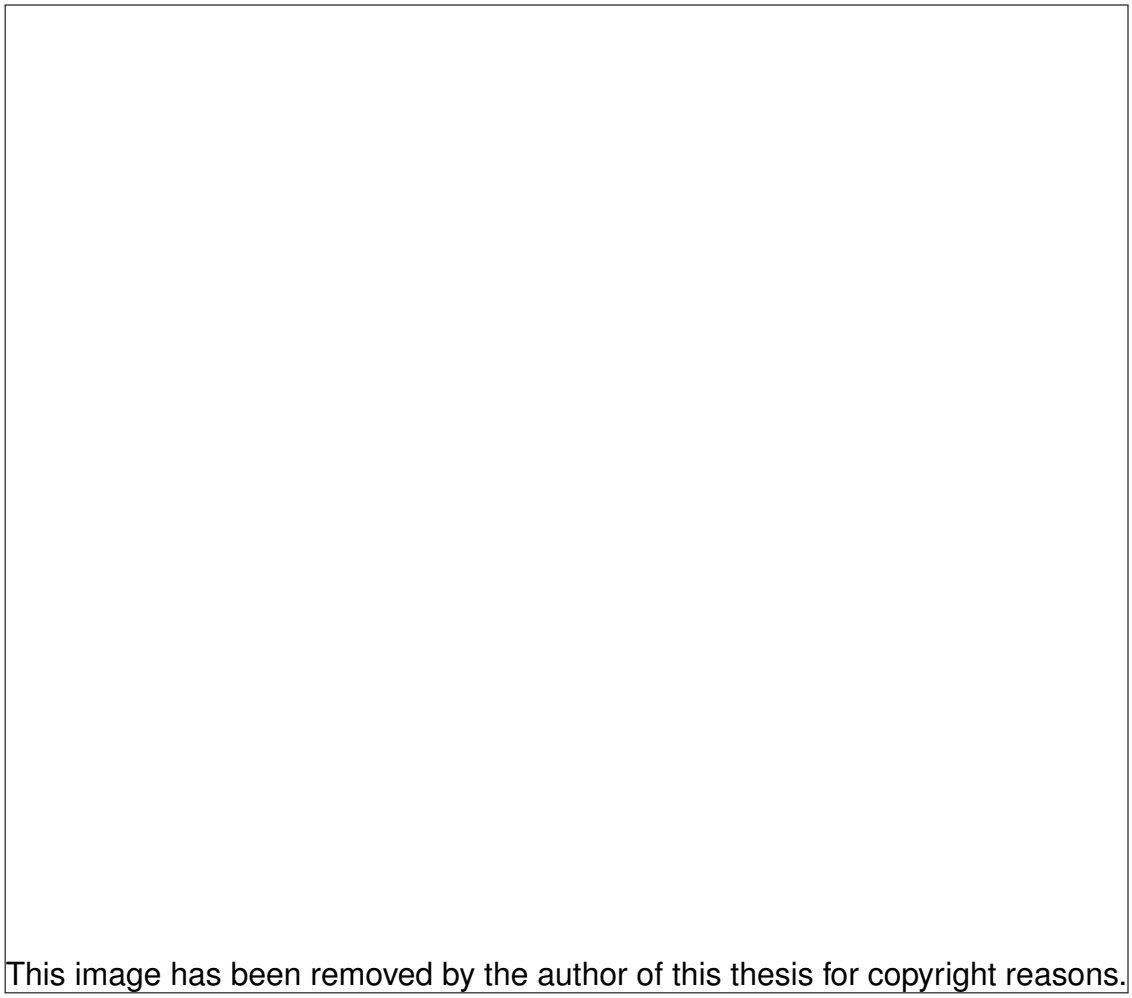

FIGURE 1.10. Plateau burstings (A, C, E) and pseudo-plateau burstings (B, D, F) generated by modification of Chay-Keizer model in [94] with different values of f and v_n. Image from [94]. Increasing v_n results in the oscillations from plateau bursting to pseudo-plateau bursting. The bottom figure shows the slow-fast analysis of the model when v_n=-12 mV. The two trajectory shown in B and F above, when f=0.00025 (orange) and f=0.01 (black) respectively, are superimposed. Image from [92].

Hopf bifurcation (labelled as *subHB*) undergo a homoclinic bifurcation (labelled as *HM*). The trajectories in Figure 1.10 B (orange) and F (black) are superimposed on the fast subsystem bifurcation diagram. As the parameter f increases, the transition occurs from plateau to pseudo-plateau bursting.

The modified Chay-Keizer model discussed above has two fast (V_{m}, n) and one slow (Ca) variable. Therefore, the slow variable Ca is used as a bifurcation parameter to perform a bifurcation analysis. However, changing some of the model parameters could change the number of fast and slow variables in biophysical models. For instance in [93], the membrane capacitance C_{m} was changed to make the model has one fast (V_{m}) and two slow (n, Ca) variables. Using the *2-slow/1-fast* analysis, it was shown that pseudo-plateau bursting is a *canard-induced mixed mode oscillations* [93]. We will explain the details of the 2-slow/1-fast analysis and apply this analysis to the IHC model in Chapter 4.

Reviewing the original and modified Chay-Keizer models, we are now able to study the IHC model in detail in the following section.

1.3 A Mathematical Model for Immature Inner Hair Cells

In this section, we introduce a mathematical model, called the *IHC model*, of immature inner hair cells' (IHCs) action potentials based on experimental data, which was originally proposed in [90]. We discuss the action potentials of the immature IHCs and review the mathematical model equations in detail in this section.

1.3.1 Membrane Currents of Immature IHCs

We reviewed the Ca^{2+}-based action potentials of the immature IHCs in Section 1.1.4. Figure 1.11 summarises the ionic currents involved in action potentials in immature IHCs. Unlike neurones, action potentials of immature IHCs are generated by calcium (Ca^{2+}) rather than sodium (Na^{+}) influx and terminate when external Ca^{2+} is removed. Immature IHCs also express sodium currents I_{Na}. Although sodium currents do not contribute to the upstroke of the action potential, they increase the rate of depolarisation to threshold [63]. At rest, Ca^{2+}-activated K^{+} channels (SK) are closed due to low Ca^{2+}

concentration. During action potential firing, the membrane potential depolarises and opening voltage-gated Ca^{2+} channels result in Ca^{2+} influx. Additionally, Ca^{2+} signals are amplified by CICR from intracellular stores. Due to the level of intracellular Ca^{2+} which is increased, Ca^{2+}-activated K^+ channels are opened and generate an outflow of K^+ ions [50, 62] in addition to outflow of K^+ ions through the voltage-gated K^+ channels. This results in the repolarisation of the cell and closure of voltage-gated Ca^{2+} channels.

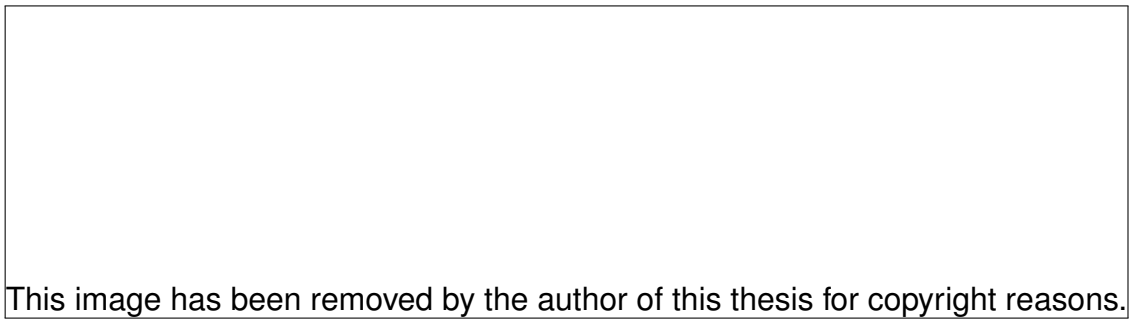

FIGURE 1.11. Membrane currents involved in spiking in developing IHCs. I_{K1}: the inward K^+ current, $I_{K,\,neo}$: the delayed rectifier current, I_{Na}: sodium current, I_{Ca}: voltage-gated Ca^{2+} current, I_{SK}: Ca^{2+}-activated K^+ current. Image from [62].

A mathematical model, called the *IHC model*, was orginally proposed in [90] by taking into account the experimental results [25, 38, 46, 49, 61–63, 108]. We review the IHC model, which is a Chay-Keizer type, in detail in the following section.

1.3.2 The IHC Model

The IHC model was originally introduced in [90] and explained in detail in the supplement of [31]. We review the model equations in detail here.

The IHC model is based on experimental data that takes into account the interaction between voltage and calcium dependent ion channels. The IHC model is of the Chay-Keizer [13] type and is formulated in accordance with voltage-clamp experimental data obtained from immature IHCs.

The IHC model consists of four coupled ordinary differential equations (ODEs) including the membrane potential (V_m) measured in mV, the dimensionless activation (n) and inactivation (h) variables for the voltage-gated K^+ channel and the intracellular calcium concentration (Ca) measured in μM. We now describe the ion channels and ODEs of the IHC model in greater detail. The parameters used in the IHC model will be given in Table 1.1 at the end of this chapter.

Voltage-gated Ca^{2+} Channels:

The Ca^{2+} current is an L-type current carried by the CaV1.3 subunit [38, 75]. The voltage-gated Ca^{2+} ion current equation is given by

$$I_\mathrm{Ca}(V_\mathrm{m}, Ca) = g_\mathrm{Ca} m_\infty^2(V_\mathrm{m}) q_\infty(Ca)(V_\mathrm{m} - V_\mathrm{Ca}) \tag{1.16}$$

The Boltzmann function is used to describe the steady-state activation variable $m_\infty(V_\mathrm{m})$ of the voltage-gated Ca^{2+} channels as well as the steady-state activation $n_\infty(V_\mathrm{m})$ and inactivation $h_\infty(V_\mathrm{m})$ variables of the voltage-gated K^+ channels.

Based on the experimental results [19, 61, 83, 86] that were fitted by single first-order Boltzmann equations, the voltage-gated Ca^{2+} channels were assumed to become active instantaneously

$$m_\infty(V_\mathrm{m}) = (1 + e^{(V_\mathrm{mL} - V_\mathrm{m})/s_\mathrm{m}})^{-1} \tag{1.17}$$

where V_mL is the potential of half-maximal activation and s_m is the voltage sensitivity of the activation.

The analytical expression of the inactivation function q_∞ based on [25] is given by

$$q_\infty(Ca) = (1 + Ca/K_\mathrm{q})^{-1} \tag{1.18}$$

The activation (m_∞) and inactivation (q_∞) functions are illustrated in Figure 1.12.

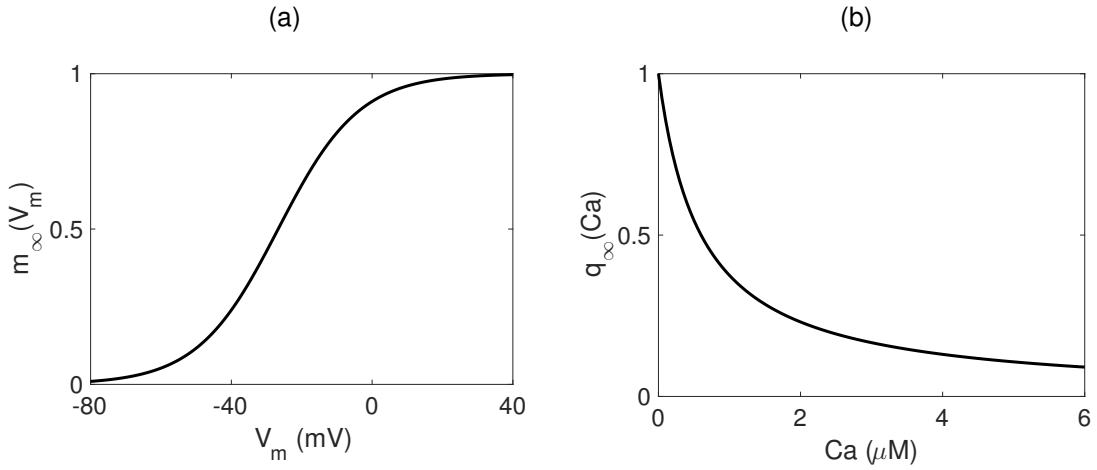

FIGURE 1.12. The activation (a) and inactivation (b) functions of the voltage-gated Ca^{2+} channels.

Ca^{2+}-activated K^+ Channels:

Ca^{2+}-activated K^+ channels in the immature inner hair cells are considered to take part in the development of hearing [62]. The Ca^{2+}-activated K^+ ion current equation is given by

$$I_{K_{Ca}}(V,Ca) = g_{K_{Ca}} s_\infty(Ca)(V - V_K) \tag{1.19}$$

where s_∞ is the steady-state activation function of the K_{Ca} channels given by [35]

$$s_\infty(Ca) = \frac{Ca^4}{Ca^4 + k_s^4} \tag{1.20}$$

where k_s is the half maximal effective concentration of intracellular Ca^{2+} concentration. The steady-state activation function of the K_{Ca} channels (s_∞) is illustrated in Figure 1.13.

Voltage-gated K^+ Channels:

The voltage-gated K^+ ion current equation is given by

$$I_K(V_m,n,h) = g_K n h (V_m - V_K) \tag{1.21}$$

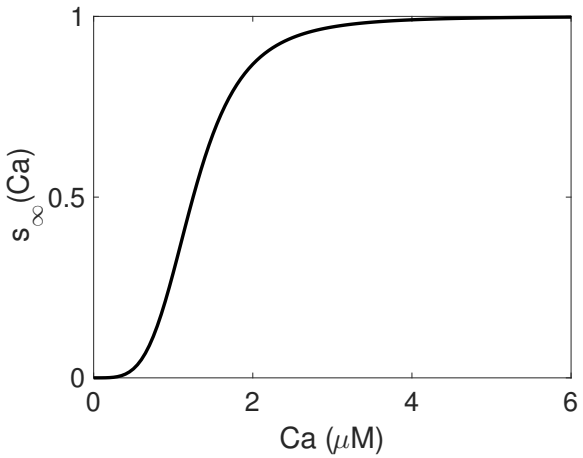

FIGURE 1.13. The steady-state activation function of the K_{Ca} channels.

where n and h represent the activation and inactivation variables associated with the voltage-gated K^+ channels, respectively.

The steady-state functions of these variables are given by

$$n_\infty(V_m) = (1 + e^{(V_n - V_m)/s_n})^{-1} \tag{1.22}$$

$$h_\infty(V_m) = 0.214 + 0.355(1 + e^{(V_m - V_{h1})/s_{h1}})^{-1} + 0.448(1 + e^{(V_m - V_{h2})/s_{h2}})^{-1} \tag{1.23}$$

The steady-state activation (n_∞) and inactivation (h_∞) function of the voltage-gated K^+ channels are illustrated in Figure 1.14.

The time scale function of the activation variable n is

$$\tau_n(V_m) = 0.0022 + 0.0029e^{-V_m/s_{\tau_n}} \tag{1.24}$$

and is illustrated in Figure 1.15. However, the voltage-gated K^+ channels were assumed to inactivate on a slow constant time scale $\tau_h = 0.55\ s^{-1}$.

The activation (n) and inactivation (h) of the voltage-gated K^+ channels are described

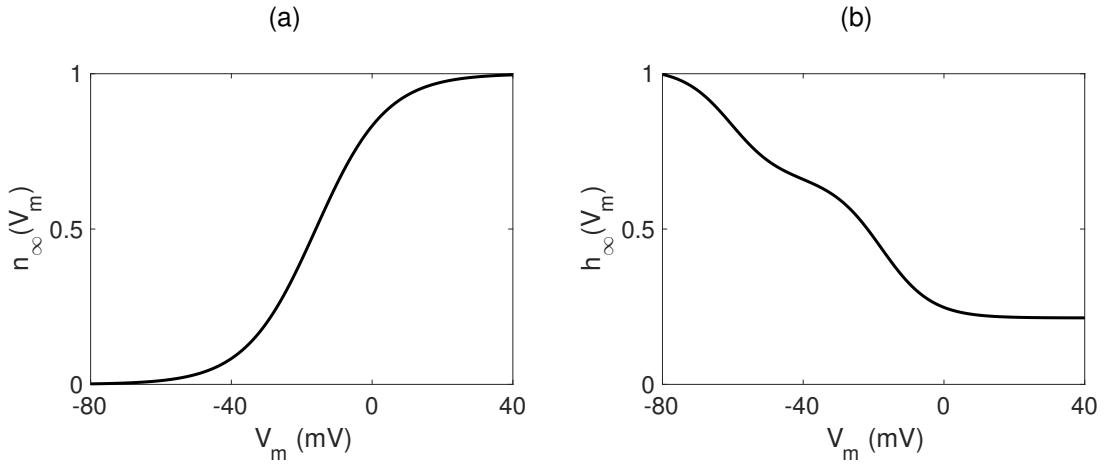

FIGURE 1.14. The activation (a) and inactivation (b) functions of the voltage-gated K^+ channels.

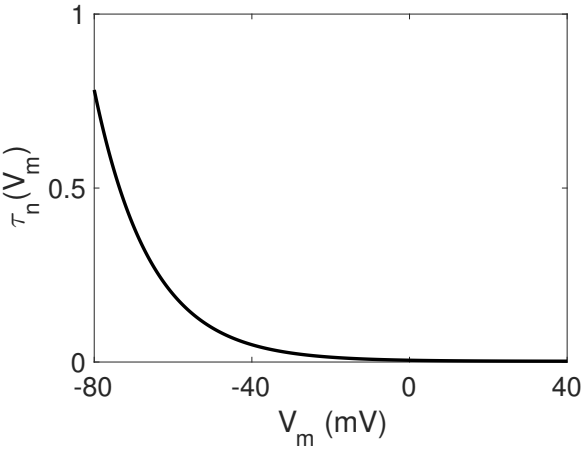

FIGURE 1.15. The time scale function of the activation of the voltage-gated K^+ channels.

by

$$\begin{aligned} \frac{\mathrm{d}n}{\mathrm{d}t} &= \frac{n_\infty(V_\mathrm{m}) - n}{\tau_\mathrm{n}(V_\mathrm{m})} \\ \frac{\mathrm{d}h}{\mathrm{d}t} &= \frac{h_\infty(V_\mathrm{m}) - h}{\tau_\mathrm{h}}. \end{aligned} \tag{1.25}$$

Like the Chay-Keizer model equations [13], the membrane current of the IHC model is the sum of all the contributions of the ionic currents discussed above (1.20), (1.21)

and (1.16) and plus a leak current given by

$$I_{\text{leak}}(V_{\text{m}}) = g_{\text{leak}}(V_{\text{m}} - V_{\text{leak}}). \tag{1.26}$$

Then, the rate of change of the membrane potential is expressed by

$$C_{\text{m}}\frac{\text{d}V_{\text{m}}}{\text{d}t} = -I_{\text{Ca}}(V_{\text{m}}, Ca) - I_{\text{K}}(V_{\text{m}}, n, h) - I_{\text{K}_{\text{Ca}}}(V_{\text{m}}, Ca) - I_{\text{leak}}(V_{\text{m}}) \tag{1.27}$$

where $C_{\text{m}} = \frac{10^{-5}}{A_{\text{cell}}}$ is the membrane capacitance and $A_{\text{cell}} = \pi \times d_{\text{cell}}^2$ is the area of the cell. In order to complete the IHC model , we need one more equation that defines the rate of change of the intracellular Ca^{2+} concentration, which is given below.

Intracellular Ca^{2+} Dynamics:

The rate of change of the intracellular Ca^{2+} concentration (Ca) is given by the balance equation

$$\frac{\text{d}Ca}{\text{d}t} = J_{\text{in}}(V_{\text{m}}, Ca) - J_{\text{out}}(Ca) \tag{1.28}$$

where the Ca^{2+} influx (J_{in}) and efflux (J_{out}) are

$$J_{\text{in}}(V_{\text{m}}, Ca) = -f_{\text{c}}\alpha I_{\text{Ca}}(V_{\text{m}}, Ca) + p_{\text{ER}}(Ca_{\text{ER}} - Ca) \tag{1.29}$$

$$J_{\text{out}}(Ca) = \frac{k_{\text{PMCA}}Ca^2}{Ca^2 + K_{\text{p}}^2} + k_{\text{SERCA}}Ca \tag{1.30}$$

The intracellular Ca^{2+} is increased by Ca^{2+} ion flow via voltage-gated Ca^{2+} channels and via intracellular Ca^{2+} stores through ryanodine receptors (RyRs) [46], called Ca^{2+}-induced Ca^{2+} release (CICR). On the other hand, Ca^{2+} efflux occurs through plasma-membrane Ca^{2+} (PMCA) and endoplasmic reticulum (SERCA) Ca^{2+} pumps.

The parameter f_{c} is the ratio of free to total cytosolic Ca^{2+}, which is multiplied with the fluxes through the cell membrane. We note that this parameter controls the time scale

of the intracellular Ca^{2+}, and its role in the overall dynamics of the IHC model will be investigated in Chapter 4 via a slow-fast analysis.

The parameter α is the factor that converts currents into Ca^{2+} ion fluxes, which is inversely proportional to the cell area i.e. $\alpha = \frac{10^5}{2\times 9.65\times A_{\text{cell}}}$ where $A_{\text{cell}} = \pi \times d_{\text{cell}}^2$ is the area of the cell.

k_{PMCA} is the maximum rate of plasma membrane, k_{SERCA} is the ER calcium ATPase pump rate and p_{ER} is the rate of calcium-induced calcium release (CICR). Ca^{2+} concentration in the ER is assumed to be constant and is represented by c_{ER} in the model.

The IHC model parameters and their dimensions are given in Table 1.1.

1.4 Thesis Outline

In this chapter, we discuss the Ca^{2+}-based action potentials of immature IHCs. In order to gain further insight into the electrical activity and intracellular Ca^{2+} signalling in immature IHCs, a mathematical model, called the IHC model, based on experimental results, was originally developed in [90] and is introduced in Chapter 1. In order to review the previous work in mathematical modelling, we introduce the Chay-Keizer model [13], upon which the IHC model is based, and discuss some developed techniques to be used in the investigation of the dynamics of the oscillations in immature IHCs.

There are three notable parameters that significantly contribute to calcium regulation in the IHC model, namely $g_{\text{K}_{\text{Ca}}}$ (the maximum Ca^{2+}-activated K^+ channel conductance), p_{ER} (the rate of Ca^{2+}-induced Ca^{2+} release (CICR)) and g_{Ca} (the maximum Ca^{2+} channel conductance). Since the action potentials of IHCs depend on Ca^{2+}, we are interested in understanding the effects of varying the three parameters on the IHC model solutions.

	Parameter	Value	Dimension
Voltage-gated Ca^{2+} current (I_{Ca})	g_{Ca}	2.4	nS
	V_{Ca}	-60	mV
	V_{mL}	-26.7	mV
	s_m	11.5	mV
	K_q	0.6	μM
Ca^{2+}-activated K^+ current ($I_{K_{Ca}}$)	$g_{K_{Ca}}$	4	nS
	V_K	60	mV
	k_s	1.25	μM
Voltage-gated K^+ current (I_K)	g_K	2.85	nS
	V_K	60	mV
	V_n	-16	mV
	s_n	10	mV
	V_{h_1}	-60.5	mV
	s_{h_1}	6.8	mV
	V_{h_2}	-17.8	mV
	s_{h_2}	7.1	mV
	s_{τ_n}	14.3	mV
	τ_n	0.55	s
Leak current (I_{leak})	g_{leak}	0.12	nS
	V_{leak}	-20	mV
Intracellular Ca^{2+} Equation	f_c	0.004	
	α	7.3	$\mu MpA^{-1}s^{-1}$
	k_{PMCA}	3.6	s^{-1}
	K_p	0.08	μM
	k_{SERCA}	1.2	s^{-1}
	p_{ER}	0.0004	s^{-1}
	c_{ER}	500	μM
	C_m	0.0071	nF
	d_{cell}	15	μm

Table 1.1: The IHC model parameters. The red coloured parameters are the bifurcation parameters for the bifurcation analysis performed in Chapters 2 and 3.

Chapter 2 looks at a numerical bifurcation analysis of the IHC model. Previous studies [31, 90] investigated the effects of the parameters $g_{\mathrm{K_{Ca}}}$ and p_{ER} on the model solutions, however, the effects of varying the parameter g_{Ca} have not yet been addressed. Therefore, we attempt to present a characterisation of the relative contributions of the parameters g_{Ca}, $g_{\mathrm{K_{Ca}}}$ and p_{ER} in shaping immature IHC signalling by performing a numerical bifurcation analysis.

Chapter 3 discusses the simplification of the original (4D) IHC model. The nondimensionalisation of the IHC model provides the characteristic time scale constants of the dynamic variables. Then, we are able to reduce the dimension of the IHC model. We verify that the reduced (3D) IHC model can also reproduce the oscillations that were observed in the original IHC model. Similar to the analysis in Chapter 2, we present a characterisation of the relative contributions of the three parameters on the reduced IHC model solutions. Additionally, since the nondimensional reduced IHC model provides the characteristic time scale constants, we use this information to estimate the speed of the state variables based on the model parameters. Next, the nondimensional reduced (3D) IHC model is considered in order to apply the slow-fast analysis in Chapter 4.

Chapter 4 presents a slow-fast analysis of the reduced IHC model introduced in Chapter 3 in order to understand the dynamics underlying the oscillations of the model. The reduced IHC model can be characterised by two fast (v and n) and one slow (c) or one fast (v) and two slow (n and c) variables depending on the choices of the parameters. We explain the mechanism of pseudo-plateau bursting type oscillations of the reduced IHC model using the *1-slow/2-fast analysis*. By changing the model parameters, the slow variable becomes faster and the reduced IHC model exhibits *mixed mode oscillations (MMOs)* that are studied by the *2-slow/1-fast analysis*.

Also, one of the parameters of interest, namely g_{Ca}, has a significant effect on the characteristic time scale constants of the intracellular calcium concentration. However,

this parameter could also directly affect the time scale of the membrane voltage when it dominates the other conductances in the model since the time scale of v is given by $\hat{\tau}_v := \frac{C_\mathrm{m}}{Q_\mathrm{t} g_\mathrm{max}}$ where g_max is the maximum of the conductances. We attempt to interpret the dynamics of the complex solutions according to the differences in the time scales between fast and slow variables of the reduced IHC model. However, as a limitation of our analysis in this chapter, neither the 1-slow/2-fast nor the 2-slow/1-fast analyses can adequately explain the mechanism of complex solutions.

Chapter 5 summarises and suggests possible future research directions indicated through the thesis. In Chapters 2 and 3, we identify the parameter regions where the original (4D) and the reduced (3D) IHC models exhibit irregular mixed firing patterns that were also seen in the experiments (see Figure 1.5). Altough we discuss possible dynamic mechanisms underlying the aperiodic trajectories found in the model, a deeper investigation of the routes to chaos in the IHC model is left for future studies. In Chapter 4, the limitations on understanding the dynamics of the complex periodic orbits of the IHC model using 1-slow/2-fast or 2-slow/1-fast analysis, which could be due to the three distinct time scales of the model, also remain as a direction for future research.

To sum up, we shall investigate the oscillatory behaviour of the IHC model throughout this thesis. We will show that:

- As the parameter g_Ca increases, the complex oscillations lose their large spikes and become pseudo-plateau bursting solutions, which can be observed over a large span of the parameter space, resulting in a significant increase on the amplitude and duration of Ca^{2+} signals. Also, we have studied the changes on the pattern of the model solutions according to the changes of the three parameters that are directly involved in calcium dynamics regulation. This represents a significant advance compared to previous analysis of the model [31, 90].
- A simplified 3-dimensional IHC model can reproduce similar dynamics as the

original 4-dimensional model. Therefore, we no longer need to deal with phase space projections of the trajectories and attractors organising the oscillatory behaviour in the model.

- The reduced model could exhibit two time scales depending on the choice of parameters. Therefore, the mechanisms underlying the bursting dynamics and mixed mode oscillations in the model are studied applying 1-slow/2-fast and 2-slow/1-fast analysis, respectively. We find that g_{Ca} is inversely proportional to the time sclaes of the variables v and c. Therefore, large g_{Ca} causes an increase on the speed of both v and c. Hence, the periodic orbits observed at high values of g_{Ca} can also be studied by 2-slow/1-fast analysis.

- Finally, our analysis indicates that the complex (mixed) solutions in the model could not be satisfactory explained by the well-established slow-fast analysis techniques. This opens up future directions for investigation of the model dynamics.

CHAPTER 2

A NUMERICAL CONTINUATION AND BIFURCATION ANALYSIS OF THE IHC MODEL

In the previous chapter we reviewed the experimental data showing that the immature inner hair cells' (IHCs) action potentials arise due to interactions between influx from the extracellular environment via voltage-gated calcium channels [25, 38, 63, 108], calcium-sensitive potassium channels (K_{Ca}) [61, 62] as well as calcium induced calcium release (CICR) mediated via the ryanodine receptors (RyRs) in the endoplasmic reticulum (ER) [31, 46]. Furthermore, IHCs action potentials and associated calcium signals manifest themselves in the form of regular single spikes, bursts with several small spikes and chaotic solutions of mixed type, mixture of spikes and burst, in the membrane potential of the cell [31, 90].

A mathematical model, called the *IHC model*, based on the experimental data to mathematically model the complicated biological process in the developing inner hair cells, was introduced in [90] and explained in detail in Chapter 1.

The IHC model is defined by a set of four ordinary differential equations (ODEs) as

$$\begin{aligned}
C_{\mathrm{m}}\frac{\mathrm{d}V_{\mathrm{m}}}{\mathrm{d}t} &= -I_{\mathrm{Ca}}(V_{\mathrm{m}},Ca) - I_{\mathrm{K}}(V_{\mathrm{m}},n,h) - I_{\mathrm{K_{Ca}}}(V_{\mathrm{m}},Ca) - I_{\mathrm{leak}}(V_{\mathrm{m}}) \\
\frac{\mathrm{d}n}{\mathrm{d}t} &= \frac{n_\infty(V_{\mathrm{m}}) - n}{\tau_{\mathrm{n}}(V_{\mathrm{m}})} \\
\frac{\mathrm{d}h}{\mathrm{d}t} &= \frac{h_\infty(V_{\mathrm{m}}) - h}{\tau_{\mathrm{h}}} \\
\frac{\mathrm{d}Ca}{\mathrm{d}t} &= f_{\mathrm{c}}\left(-\alpha I_{\mathrm{Ca}}(V_{\mathrm{m}}) - \frac{k_{\mathrm{PMCA}}Ca^2}{Ca^2 + K_{\mathrm{p}}^2}\right) - k_{\mathrm{SERCA}}Ca + p_{\mathrm{ER}}(Ca_{\mathrm{ER}} - Ca)
\end{aligned} \tag{2.1}$$

where V_{m} denotes the membrane potential, (n) the activation and (h) the inactivation variable for the voltage-gated K^+ channel and Ca is the intracellular Ca^{2+} concentration.

The action potential firing in immature inner hair cells is calcium-based [49, 63]. Therefore we are interested in the parameters of the IHC model that control the dynamics of calcium in the model. We will investigate the effects of these parameters on the IHC model solutions in this chapter.

2.1 Periodic Patterns of the IHC Model: Simple and Complex

There are three notable parameters that significantly contribute to the calcium regulation in the IHC model, namely $g_{\mathrm{K_{Ca}}}$ (the maximum $\mathrm{K_{Ca}}$ channel conductance), p_{ER} (the rate of calcium-induced calcium release (CICR)) and g_{Ca} (the maximum calcium channel conductance). Since the action potentials of IHCs depend on calcium, we will try to understand the effects of varying these three parameters in this chapter.

Firstly, the effects of varying the parameter $g_{\mathrm{K_{Ca}}}$ has already been investigated [90]. A one-parameter bifurcation diagram using $g_{\mathrm{K_{Ca}}}$ as a bifurcation parameter was computed to show that decreasing $g_{\mathrm{K_{Ca}}}$ results in complex periodic orbits with more spikes, found on isolated solution branches, called *isolas* [31, 90].

Secondly, a numerical bifurcation analysis was performed by continuing the bifurcations underlying different stable periodic solutions in (p_{ER}-$g_{K_{Ca}}$)-space [31] in order to understand the relative contribution of the rate of CICR (p_{ER}) and the maximum K_{Ca} channel conductance ($g_{K_{Ca}}$) to specific characteristics of the action potential waveforms, such as shape and duration, observed experimentally in the immature inner hair cells. As these two parameters change, the two-parameter bifurcation diagram in ($g_{K_{Ca}}$-p_{ER})-space (Figure 3-a in [31]) indicated the regions of some stable periodic orbits as well as irregular mixed firing patterns.

In this chapter we investigate the behaviour of the model solutions as the above mentioned parameters vary using numerical bifurcation analysis. We employ XPPAUT [22] for numerical integration of the IHC model and AUTO [18] for numerical continuation. We further compute two-parameter bifurcation diagrams in (g_{Ca}-p_{ER})-space and (g_{Ca}-$g_{K_{Ca}}$)-space to gain an insight into the changes of the model solutions in three parameters. In this way we attempt to present a characterisation of the relative contributions of g_{Ca}, $g_{K_{Ca}}$ and p_{ER} to the transitions between different dynamic states in the IHC model.

2.1.1 Single Spikes and Quasi-Periodic Solutions

The dependence of the model solutions on two parameters, namely $g_{K_{Ca}}$ and p_{ER}, involved in the regulation of calcium dynamics has been previously investigated [31, 90]. However, there is another important parameter, the maximum calcium channel conductance (g_{Ca}), that contributes significantly to the overall calcium flux in the IHC model and whose involvement in shaping the action potentials and calcium signals generated by the model has not been addressed. In order to investigate the interplay between electrical activity and calcium dynamics in the IHC model, we perform a bifurcation analysis using g_{Ca} as a bifurcation parameter.

In Figure 2.1 we show a one-parameter bifurcation diagram using g_{Ca} as a bifurcation parameter. For small values of g_{Ca}, the IHC model produces stable equilibrium solu-

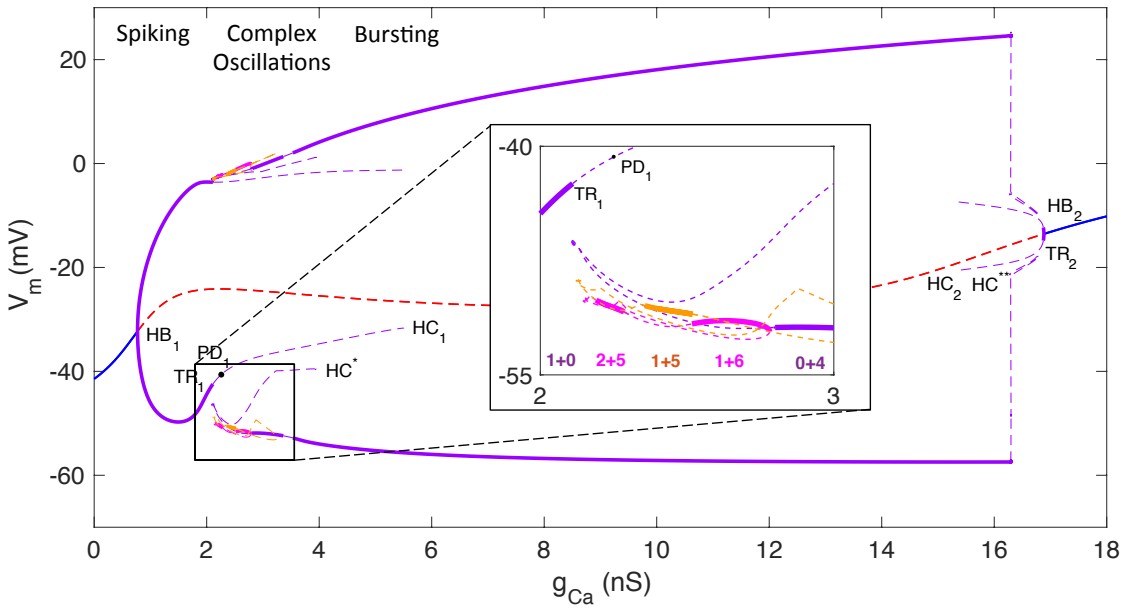

FIGURE 2.1. One-parameter bifurcation diagram of the IHC model in the parameter g_{Ca}. The region of complex periodic orbits is magnified in the middle of the diagram. We fixed the two parameters, which are $g_{\mathrm{K_{Ca}}}$=1.98, p_{ER}=0.0004, all other parameters of the IHC model are given in Table 1 in Chapter 1. Solid lines represent stable solution branches and dashed lines represent unstable solution branches. Periodic orbits are denoted by the number of their large (normal) and plateau oscillations. For example; *2+5* represents a periodic orbit with 2 large (normal) spikes and a burst made of 5 plateau oscillations. HB: Hopf bifurcation, TR: Torus bifurcation, PD: Period-doubling bifurcation, HC: Homoclinic bifurcation.

tions (solid blue curve). As g_{Ca} increases, the family of stable equilibria undergoes a supercritical Hopf bifurcation (HB_1) at g_{Ca}=0.77 and becomes unstable (dashed red curve). This unstable family of equilibria regains stability at a second supercritical Hopf bifurcation (HB_2) for g_{Ca}=16.88. A family of stable spiking solutions arises from the first supercritical Hopf bifurcation (HB_1) and loses its stability at a torus bifurcation (TR_1) for g_{Ca}=2.11.

The branch of unstable single spike periodic orbits undergoes a period-doubling bifurcation (PD_1), which does not change the stability of the branch. Continuing these

period-doubling bifurcations creates unstable period-doubled limit cycle branches that terminate via homoclinic bifurcations (for example, we plotted the homoclinic orbit that corresponds to HC_1 in Figure 2.2(b)). These computations indicate that the branches of limit cycle solutions originating from HB_1 and HB_2 are disconnected. However, there is a possibility that these branches connect in other model parameters and/or that not all invariant objects have been captured in our computations so far. Thus, we have to explore complex and bursting periodic orbits by direct numerical integration of the IHC model equations in a relatively large range of values for the parameter g_{Ca} (2.11<g_{Ca}<16.87) in order to trace their families in the parameter g_{Ca}, which will be done in the next section. However, as we showed in Figure 2.1, the IHC model produces stable single spikes between the Hopf bifurcation (HB_1) and the torus bifurcation (TR_1) for smaller values of the parameter g_{Ca}. The IHC model also produces quasi-periodic oscillations nearby the bifurcation point TR_1.

In Figure 2.2(a) we show the phase-space projection onto (Ca, n, V_m)-space of a stable-single spike periodic orbit when g_{Ca}=2.1, that is very close to the torus bifurcation, which occurs at g_{Ca}=2.11. Also, we plot the homoclinic orbit at g_{Ca}=5.51, where the branch originating from HB_1 terminates (see Figure 2.2(b)) via a homoclinic bifurcation (HC_1). The red dot on the periodic orbit represents the saddle equilibrium, which indicates where the trajectory joins the equilibrium to itself as time goes to infinity, called *homoclinic orbit* [89].

The torus bifurcation (TR_1) occurs at g_{Ca}=2.11, which destabilises the family of single-spike periodic solutions. Near TR_1 the IHC model produces two dimensional invariant torus around the unstable periodic orbit [53]. We plot the projection of the torus (informally, a bagel or doughnut shaped) when g_{Ca}=2.113 onto (Ca, n, V_m)-space in Figure 2.2(c). In order to confirm the quasi-periodic motion, we calculate a Poincaré section of the torus [6], which we considered to be the section V_m=-25 since the membrane potential (V_m) in Figure 2.2(c) is in the range -60 mV to 0 mV. Therefore, the choice V_m=-25 would be sufficient to indicate the quasiperiodic motion by Poincaré

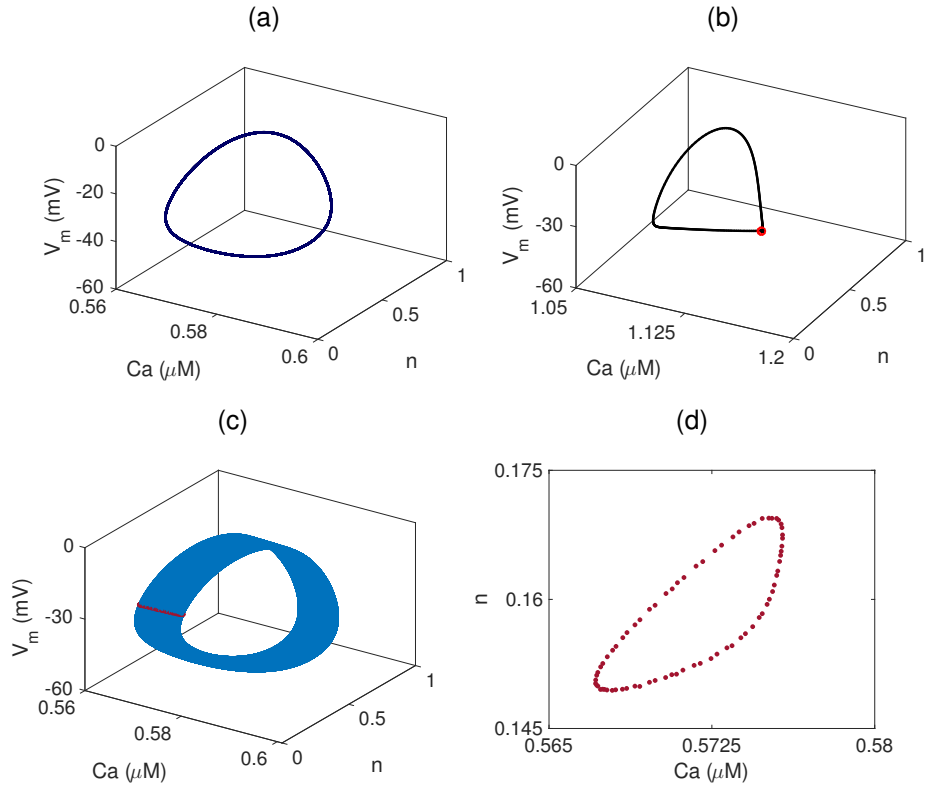

FIGURE 2.2. Some of the IHC model solutions projected onto (Ca, n, V_m)-space that correspond to the bifurcation parameter (a) g_{Ca}=2.1, (b)g_{Ca}=5.51 and (c) g_{Ca}=2.113 (see Figure 2.1 for the bifurcation diagram). (d) A Poincaré section at V_m=-25 of the torus shown in Figure 2.2(c) on the (Ca, n)-space.

section. Unlike the periodic orbits whose Poincaré sections consist of n points (for period-n limit cycles) in the phase space, Poincaré sections of an invariant torus forms a closed curve in the phase space, which indicates that the motion is quasi-periodic [68]. In Figure 2.2(d), we plot the Poincaré section at V_m=-25 of the torus shown in Figure 2.2(c). The trajectory never crosses the Poincaré section at the same point twice and hence forms a closed curve [95].

We have shown examples of how the IHC model trajectories form as single spikes and invariant tori at low values of g_{Ca} when all the other model parameters are fixed. Additionally, as the parameter g_{Ca} increases, the IHC model produces complex periodic orbits, which are a combination of large and small oscillations, shown in Figure 2.1.

We will investigate such solutions in more detail in the following section.

2.1.2 Complex Bursting Oscillations

In the previous section we showed a one-parameter bifurcation diagram using g_{Ca} as a bifurcation parameter in order to gain an insight into the contribution of g_{Ca} to the IHC model solutions. We continued the branches emanating from the Hopf bifurcation (HB_1), and showed that these branches terminate at homoclinic bifurcations. By direct numerical integration of the IHC model, we computed a torus at g_{Ca}=2.113 near the torus bifurcation point (TB_1). In this section, we investigate more complicated periodic orbits that form as a combination of large and small spikes for the paramater g_{Ca}>2.113.

We mentioned that the complex periodic orbits consisting of one large (normal) spike and several small spikes within the plateau-bursting part of the corresponding orbit were observed lying on isolated solution branches as the parameter $g_{\mathrm{K_{Ca}}}$ varies [90]. Similar behaviour can also be shown for the parameter g_{Ca}. In Figure 2.3(a) we depict a part of the bifurcation diagram that is disconnected from the other branches, called an *isola* [90]. In order to plot an isola, first we calculate a stable periodic orbit by direct numerical integration of the IHC model with fixed g_{Ca}. For instance, we show a time series representation such as a complex periodic orbit consisting of two large (normal) spikes and a burst made of five plateau oscillations in Figure 2.3(b). Once we have obtained one of the stable solutions of a continuous family, then we are able to continue the periodic orbit in order to find the continuous family of such periodic orbits as g_{Ca} varies.

In Figure 2.3(a) we show a continuous family of periodic attractors of the IHC model that shares the same total number of spikes which, as was shown in [31], is seven in this case. We represent a complex orbit by the number of its oscillations such as *M+N* solution, which means that the orbit consists of M large (normal) spikes and a burst made of N plateau oscillations. For example the isola in Figure 2.3(a) contains

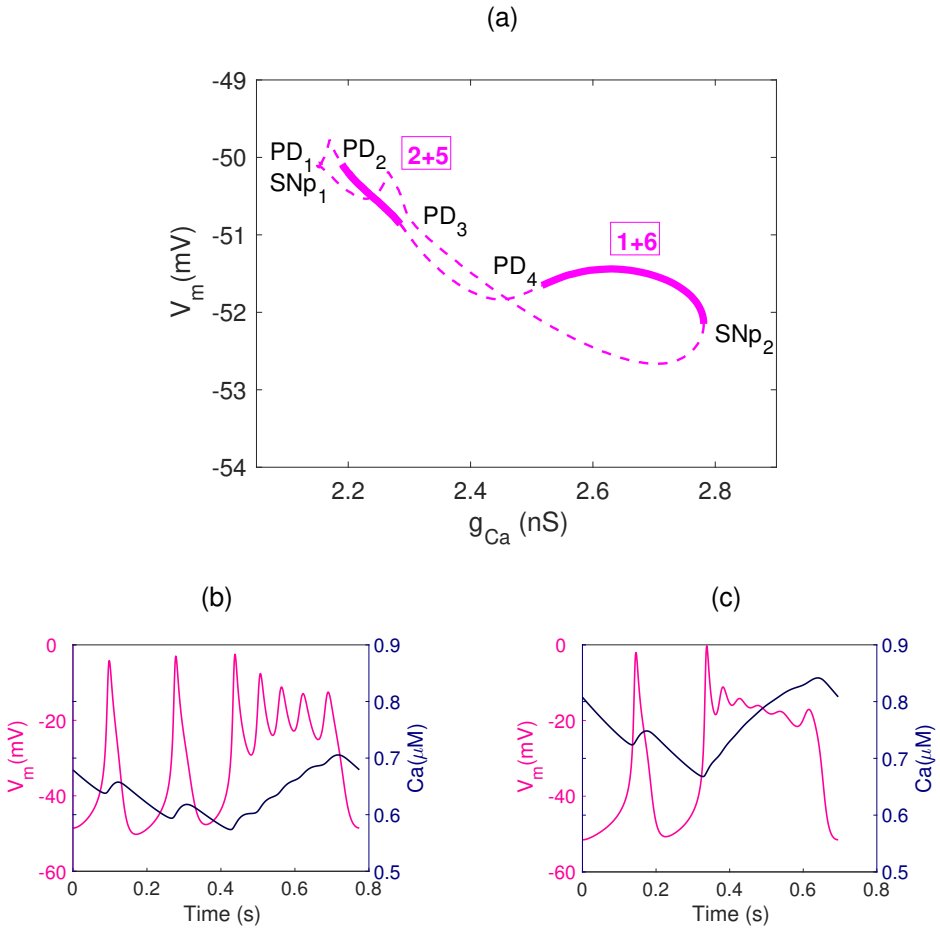

FIGURE 2.3. (a) An isolated branch of periodic solutions in the model, *isola*, in the parameter g_{Ca}. Solid lines represent stable solution branches and dashed lines represent unstable solution branches. PD: Period doubling bifurcation, SNp: Saddle node bifurcation for periodic orbits. (b) Complex bursting orbit with 2 large spikes and a burst made of 5 plateau oscillations (*2+5* solution) at g_{Ca}=2.2. (c) Complex bursting orbit with 1 large spike and a burst made of 6 plateau oscillations (*1+6* solution) at g_{Ca}=2.6. Both solutions belong to the isola, along which the total number of oscillations is fixed (7 in this case).

solutions with 7 oscillations in total, which are *2+5* solution (2 large spikes and a burst made of 5 plateau oscillations) and *1+6* solution (1 large spike and a burst made of 6 plateau oscillations). Additionally, we will denote this isola by I_7 [31].

In order to compute a solution branch or an isola such as shown in Figure 2.3(a), we first calculate a stable periodic orbit as shown in Figure 2.3(b) or Figure 2.3(c) by

direct numerical integration of the model equations with the given set of parameters. Once we have a stable periodic orbit, then AUTO [18] allows us to continue that orbit as the bifurcation parameter varies. Additionally, AUTO calculates the multipliers at each step, which gives the information about the stability of the periodic solutions along the isola. The stability of the solution branch changes at some bifurcation points such as period-doubling (PD) and saddle-node of periodic (SNp) bifurcations (see Figure 2.3(a)). AUTO can locate the bifurcation of equilibrium and periodic orbits by computing the multipliers [9]. For example, one of the multipliers crosses the unit circle at -1 when we have PD bifurcation, and similarly SNp bifurcation occurs when one of the multipliers crosses the unit circle at +1. Hence, we are able to plot a solution curve as shown in Figure 2.3(a), that locates the stable and unstable periodic solutions and bifurcations along the isola.

The solid lines of the isola in Figure 2.3(a) denote the stable solution branches and the dashed lines denote unstable solution branches that have 7 oscillations in total. The stable part of the isola where *2+5* solutions lie is determined by period-doubling bifurcations (PD_2 and PD_3). As g_{Ca} increases, the unstable branch becomes stable at another period-doubling bifurcation (PD_4), where stable *1+6* solutions can be found. The stable region of *1+6* solutions ends at a saddle-node bifurcation (SNp_2), which is also one of the boundaries of the isola in the g_{Ca} parameter. Additionally, we will continue these bifurcations in order to locate the regions of the stable periodic orbits in the two-parameter spaces such as (g_{Ca}-$g_{K_{Ca}}$)-space.

We plot two representative examples of complex periodic orbits computed by direct numerical simulations that correspond to two different stable regions of the isola. The *2+5* solution in Figure 2.3(a) is calculated at g_{Ca}=2.2 and *1+6* solution in Figure 2.3(c) is calculated when g_{Ca}=2.6. As g_{Ca} increases, one of the large spikes of the *2+5* solution becomes smaller between PD_3 and PD_4 and the model exhibits *1+6* solutions. However, the total number of spikes of the periodic orbits along the isola does not change. This behaviour is robust and seen at other isolas that have different number

of spikes.

We observe in the time series of the periodic orbits that the intracellular calcium concentration of *1+6* solution is larger than *2+5* solution since *1+6* solution corresponds to larger g_{Ca}. This also shows that the IHC model is able to reproduce the behaviour of inner hair cells captured in experiments, which is prolonged action potentials generate much larger and long lasting calcium signals [31, 90].

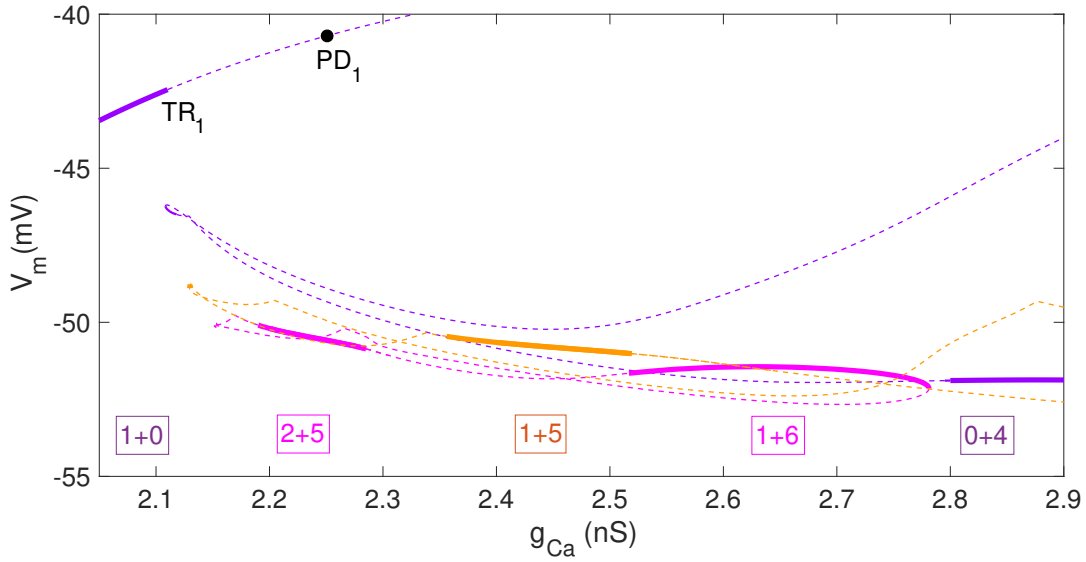

FIGURE 2.4. Bifurcation diagram of the IHC model that is zoomed to the region where the isolas are located in Figure 2.1.

In Figure 2.4, we zoom the region where the complex solutions are located in Figure 2.1. Similar to *2+5* and *1+6* solutions, we compute stable *1+5* solution by direct numerical integration of the IHC model equations. Then, we continue this solution as g_{Ca} varies, to find the family of such solutions in the parameter g_{Ca}. Unlike the isola I_7 (magenta coloured) that consists of solutions (*2+5* and *1+6* solutions) with 7 oscillations in total, there is only one stable region on the isola I_6 (orange coloured) that consists of solutions with 6 oscillations in total (*1+5* solutions), which are located between *2+5* and *1+6* solutions in the parameter g_{Ca}. As g_{Ca} increases when $g_{\mathrm{K_{Ca}}}$=1.98, p_{ER}=0.0004 and all the other parameters given in Chapter 1 are fixed in the IHC model, as we have

shown in Figure 2.4, the number of large (normal) spikes of complex periodic orbits decreases while the number of small oscillations increases in the intermediate range values of the parameter g_{Ca}, where the complex periodic behaviour is found.

Up to now, we have investigated the regions in the parameter g_{Ca} where normal spiking, quasi-periodic and complex oscillations can be detected. As we showed at the beginning of this chapter (in Figure 2.1), there is a stable branch that continues for a larger range of values for the parameter (2.79<g_{Ca}<16.29) and terminates at homoclinic bifurcations HC* and HC**. In the following section, we will investigate the periodic solutions along this branch.

2.1.3 Pseudo-Plateau Bursting

In the previous section, we considered periodic solutions up to the parameter g_{Ca}=2.78 (the saddle-node bifurcation (SNp$_2$) on the isola for *1+6* solutions). Direct numerical simulations show that the IHC model produces pseudo-plateau bursting solutions [71, 87, 94] when g_{Ca}>2.78. The stable periodic solutions that correspond to the values g_{Ca}>2.78 lie on neither one of the solution branches we have already calculated nor the branch orginating from the second Hopf bifurcation (HB$_2$). For example, we plot a stable pseudo-plateau bursting when g_{Ca}=2.8 in Figure 2.5(b).

We continue this bursting solution in the parameter g_{Ca}, which is shown in Figure 2.5 as the longest branch of stable periodic solutions in the diagram and depicts three representative stable periodic orbits along the branch in Figure 2.5(b), (c) and (d) which correspond to the parameters g_{Ca}=2.8, g_{Ca}=5 and g_{Ca}=15, respectively. At g_{Ca}=2.8 the stable periodic orbit has 4 plateau oscillations (labelled *0+4* solution). As g_{Ca} increases, the period of these orbits increase and the oscillations disappear resulting in periodic solutions which appear as large prolonged action potentials. As expected, this corresponds to an increase of the intracellular concentration in the model. We will investigate this behaviour applying slow-fast analysis in Chapter 4.

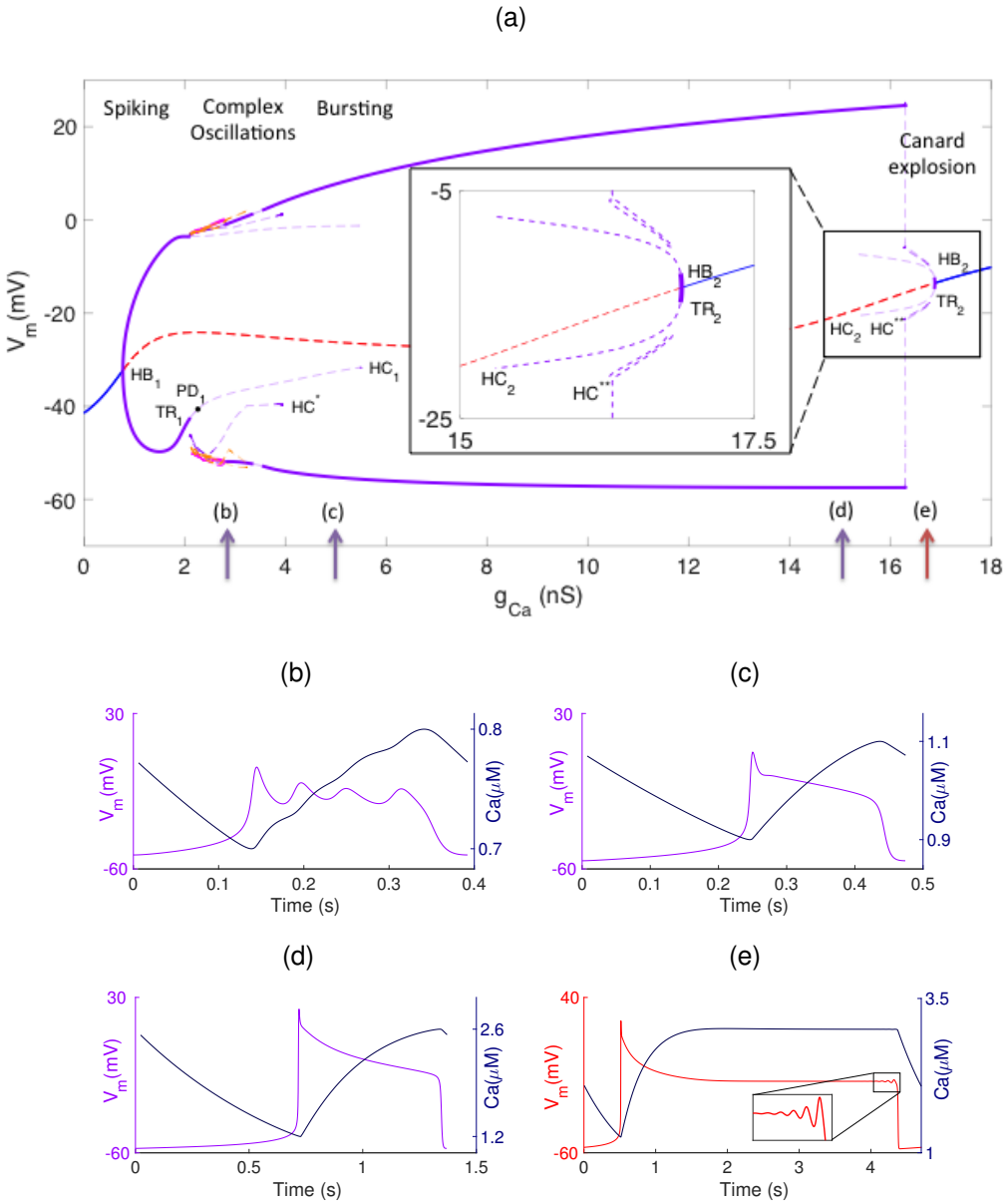

FIGURE 2.5. (a) The replaced one-parameter bifurcation diagram shown in Figure 2.1. Here the region of the second Hopf bifurcation (HB_2) is magnified in the middle of the diagram. Time series plots of stable periodic orbits correspond to the parameter g_{Ca}=2.8 (b), g_{Ca}=5 (c), g_{Ca}=15 (d) and g_{Ca}=16.75 (e). The periodic orbits shown in (b),(c) and (d) lie on the branch in the bifurcation diagram, while the periodic orbit shown in (e) does not belong to the branch and is computed via numerical simulations of the model equations.

We have already mentioned that the solution branch of the pseudo-plateau oscillations shown in Figure 2.5 is not connected to the branches orginating from Hopf bifurcations. This branch terminates at homoclinic bifurcations (HC*) and (HC**). For smaller values of g_{Ca}, this solution branch terminates at a homoclinc bifurcation (HC*) about g_{Ca}=3.946. Additinally, as g_{Ca} increases, another homoclinc bifurcation occurs (HC**) about g_{Ca}=16.29. We computed the orbits with a high period (T=1000s) near the homoclinic bifurcation points in Figure 2.6 and the saddle equilibria shown as red stars in the figure panels.

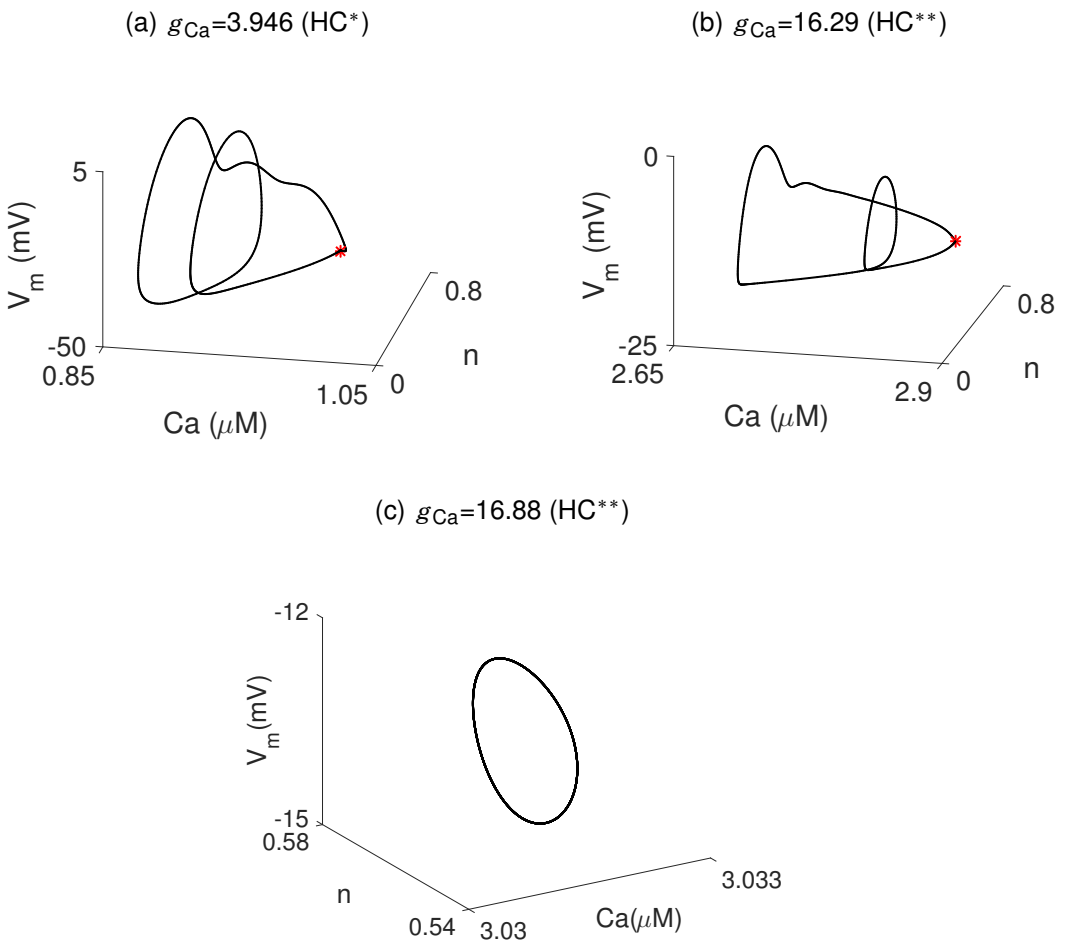

FIGURE 2.6. Homoclinic orbits at (a) g_{Ca}=3.946 (HC*) and (b) g_{Ca}=16.29 (HC**) projected on the (Ca, n, V_m)-space. Red star indicates the saddle equilibrium. (c) Small amplitude single spikes when g_{Ca}=16.88 between TR_2 and HB_2 bifurcations in Figure 2.5(a).

As g_{Ca} increases, we see in Figure 2.5 that the amplitude of limit cycles increase up to $g_{\mathrm{Ca}} \approx$16.29, which is near the second Hopf bifurcation (HB_2). Additionally, there is a rapid change in the amplitude of limit cycles, which resembles a *canard explosion* [16]. In the parameter range 16.29<g_{Ca}<16.87 (TR_2), we are able to calculate some of the stable solutions by direct numerical integration, although the branches for such periodic orbits are not continued and not plotted on the bifurcation diagram in Figure 2.5(a). Figure 2.5(e) shows a time series plot of a stable periodic orbit when g_{Ca}=16.75. We notice that the periodic orbit exhibits small oscillations near the end of the action potential. The number of the small oscillations is increased as the value of the parameter g_{Ca} approaches to the torus bifurcation point (TR_2), where the IHC model enters the parameter region of small amplitude single spikes, which continues until the second Hopf bifurcation point (HB_2). In Figure 2.6(c), we show a phase-space plot of a small amplitude periodic orbit when g_{Ca}=16.88, between TR_2 and HB_2 bifurcations shown in Figure 2.5(a).

We have investigated the periodic behaviour of the IHC model as g_{Ca} varies when all other parameters are fixed. However, we are interested in the interaction between three notable parameters that are involved in calcium regulation, namely g_{Ca}, $g_{\mathrm{K_{Ca}}}$ and p_{ER}, on the pattern of electricial activity of the IHC model. Therefore, we will perform further bifurcation analysis in order to map the stationary, normal spiking, complex and bursting as well as chaotic oscillatory regions in a relatively large portion of the parameter space, considering these parameters as bifurcation parameters.

2.2 Effects of Varying the Parameters on the Model Solutions

In the previous section we showed the normal spikes, quasi-periodic, complex and bursting oscillatory behaviours of the IHC model as the parameter g_{Ca} varies when all other parameters are fixed. Since we are interested in the interactions between the

parameters g_{Ca}, $g_{\mathrm{K_{Ca}}}$ and p_{ER}, we present two-parameter bifurcation diagrams tracing the bifurcations of branches emanating from Hopf as well as bifurcations of isolas that delimit the stable solutions of the IHC model.

2.2.1 Mapping the Interaction between g_{Ca} and $g_{\mathrm{K_{Ca}}}$

We showed in Figure 2.4 that the number of large (normal) spiking decreases as g_{Ca} increases and the solutions of the IHC model become bursting, whose plateau oscillations become too small to be seen in the given resolution when g_{Ca} is large. The one-parameter bifurcation diagram in Figure 2.1 was computed when $g_{\mathrm{K_{Ca}}}$=1.98 and p_{ER}=0.0004.

We compute a wide variety of periodic attractors, which are normal spiking, bursting and complex oscillations with one and two large (normal) spikes (*0+N*, *1+*N_1 or *2+*N_2) when p_{ER}=0.0004, and trace the bifurcations that result in a change of the stability of the periodic solutions, which are period-doubling (PD) and saddle-node bifurcation of periodic solutions (SNp). As we pointed out in the previous section, complex periodic orbits sharing the same total number of spikes belong to a continuous family of periodic attractors and lie on isolated branches (isolas). We denote such isolas by their total number of spikes. For instance, I_7 stands for an isola whose total number of spikes is 7, so the periodic solutions on such an isola could be *0+7*, *1+6*, *2+5* and so on, which can be observed at some parameter settings.

We showed that the model exhibits large (normal) spiking behaviour when g_{Ca} is small by plotting a one-parameter bifurcation diagram in Figure 2.1, and also plotted a phase space diagram of such large (normal) spiking behaviour in Figure 2.2(a). The big region at the top left corner in Figure 2.7(a) shows the stable region of the large (normal) spiking periodic solutions of the model on g_{Ca}-$g_{\mathrm{K_{Ca}}}$ plane when p_{ER}=0.0004. We showed that the large (normal) spiking behaviour loses stability via a torus bifurcation when $g_{\mathrm{K_{Ca}}}$=1.98 (see Figure 2.1) using g_{Ca} as a bifurcation parameter. As $g_{\mathrm{K_{Ca}}}$ increases, the large (normal) spiking behaviour loses stability via

(a)

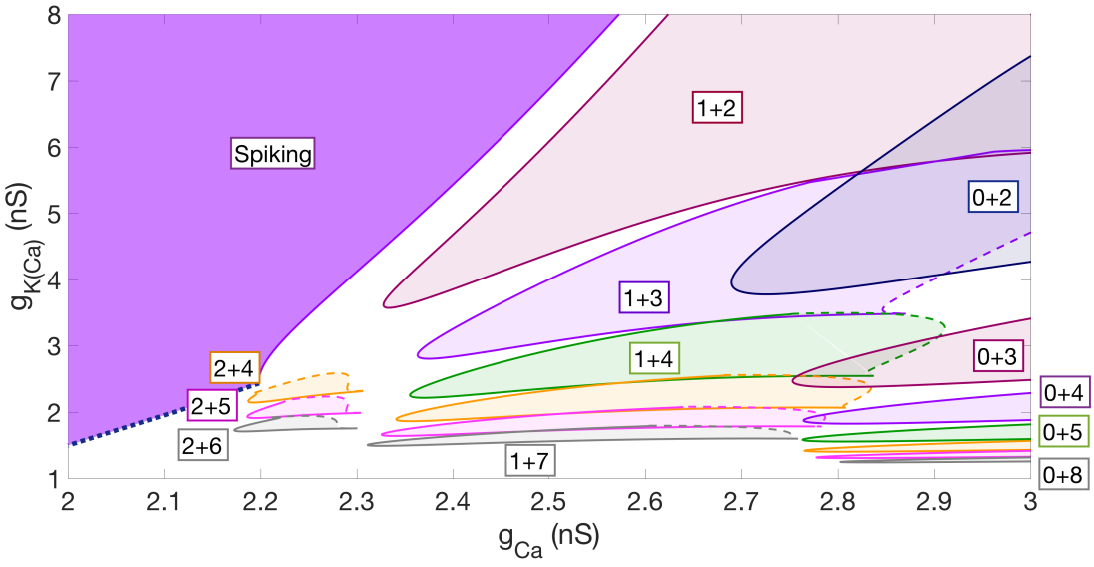

(b)

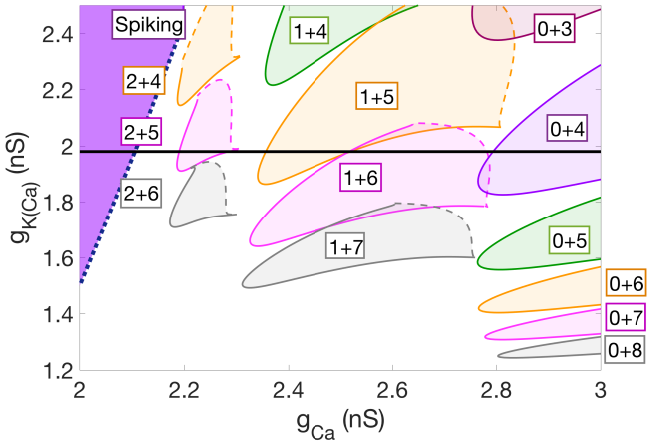

FIGURE 2.7. (a) A two-parameter bifurcation diagram of the IHC model when p_{ER}=0.0004. Stable regions of solutions are delimited by tracing the period-doubling bifurcations (solid curves) and saddle-node bifurcation of periodic solutions (dashed curves) and are coloured accordingly. Torus bifurcations of the branches originating from Hopf bifurcations are indicated by dashed dotted curves on the bottom left. White regions denote the chaotic behaviour of the IHC model. (b) Portion of the diagram. The black line represents the section at $g_{K_{Ca}}$=1.98. We showed its one-parameter bifurcation diagram in Figure 2.1 as g_{Ca} varies.

period-doubling bifurcations.

When $g_{K_{Ca}}$>2.5 in Figure 2.7, the large (normal) spiking behaviour loses stability via period-doubling bifurcations (PD). However, when $g_{K_{Ca}}$<2.5, the stability changes via torus bifurcations (TR). We could not continue the torus bifurcation curve in two parameters on g_{Ca}-$g_{K_{Ca}}$ plane when p_{ER}=0.0004. Instead, we computed several one-parameter bifurcation diagrams to detect the torus bifurcations (TR) in the parameter range 1<$g_{K_{Ca}}$<2.5, which change the stability of the spiking periodic orbits. Then, we constructed the region of the large (normal) spiking behaviour for 1<$g_{K_{Ca}}$<2.5 by linear interpolation between the computed torus bifurcation points by a blue dotted curve on the two-parameter bifurcation diagram in Figure 2.7.

The behaviour of the IHC model solutions can be interpreted by examining the two-parameter bifurcation diagram presented in Figure 2.7 where the stable regions of various periodic solutions are coloured according to the total number of oscillations of the periodic orbits in the g_{Ca}-$g_{K_{Ca}}$ plane. Additionally, the white regions also include chaotic (aperiodic) solutions of the model. We will discuss representative model solutions corresponding to white regions at the end of this chapter.

It was shown previously [31, 90] that lowering $g_{K_{Ca}}$ results in an increase in the number of the plateau oscillations. The two-parameter bifurcation diagram in Figure 2.7 confirms this behaviour on g_{Ca}-$g_{K_{Ca}}$ plane. The stable regions for complex and bursting periodic orbits with many oscillations accumulate as the parameter $g_{K_{Ca}}$ decreases. We considered the model solutions up to 8 oscillations in total (*2+6*, *1+7* and *0+8* solutions) to illustrate the behaviour of the model solutions as the parameters g_{Ca} and $g_{K_{Ca}}$ vary.

On the other hand, increasing the parameter g_{Ca} results in a decrease in the number of large (normal) spikes of complex periodic orbits. The parameter range of complex periodic orbits with 2 large (normal) spikes is smaller than the range of complex periodic orbits with 1 large spike, and this range corresponds to smaller values for

both parameters g_{Ca} and $g_{K_{Ca}}$. As g_{Ca} increases, the complex solutions with two large (normal) spikes lose one of the large spikes, where the region for such complex periodic orbits with one large spike can be found at a larger parameter region in g_{Ca}-$g_{K_{Ca}}$ plane comparing to the complex solutions with two large spikes. Increasing g_{Ca} further, the complex solutions with one large spike become bursting periodic orbits through a large range of parameter values. For larger values of the parameter g_{Ca}>3, the plateau oscillations in bursting solutions become harder to be visualised as previously shown in Figure 2.5(c) and (d).

In Figure 2.7, we showed only the stable regions of the periodic attractors which are enclose by the PD and SNp curves. The PD and SNp curves that enclose the stable region of a periodic solution become very close to each other in the parameter space, but they actually do not merge. As these curves becomes closer and closer, one of the multipliers of SNp curves cross the unit circle at -1. Similarly, one of the multipliers of PD curves cross the unit circle at +1 at the same point. Although such complex dynamical systems could have some other bifurcation curves that may not be traced here, the multipliers suggest that those special points could be codimension two bifurcations (the *fold-flip bifurcations* [54]).

Up to now, we have investigated the contributions of g_{Ca} and $g_{K_{Ca}}$ to the model solutions when p_{ER} is fixed. The role of varying the parameter p_{ER} was investigated performing a two-parameter bifurcation analysis in p_{ER}-$g_{K_{Ca}}$ plane when the third parameter (g_{Ca}) was fixed [31]. In the following section, we will try to understand the relative effects of these three parameters on the model solutions through a large span of the parameter space.

2.2.2 Interpreting the Relative Contributions of g_{Ca}, $g_{K_{Ca}}$ and p_{ER}

We have shown a two-parameter bifurcation diagram to indicate the stable regions of various periodic solutions in the g_{Ca}-$g_{K_{Ca}}$ plane in Figure 2.7 (also shown in Figure 2.8(a)) by tracing the bifurcations of isolas as well as limit cycle solution branches

corresponding to normal spiking solutions. Also, the white regions in the g_{Ca}-$g_{\mathrm{K_{Ca}}}$ plane correspond to the parameter regions of aperiodic behaviour [31], which will be discussed in Section 2.2.3. This two-parameter bifurcation diagram shows the interaction between the parameters g_{Ca} and $g_{\mathrm{K_{Ca}}}$ while the other third parameter is fixed (p_{ER}=0.0004) .

In order to complete the investigation of understanding the relative contributions of the three notable parameters, we freeze the parameter $g_{\mathrm{K_{Ca}}}$ and compute another two-parameter bifurcation diagram as g_{Ca} and p_{ER} vary, and note that the interaction between p_{ER} and $g_{\mathrm{K_{Ca}}}$ was already investigated when g_{Ca}=2.4 [31], which is reproduced in Figure 2.8(c). Therefore, we will be able to capture the behaviour of the IHC model solutions over a large span of the parameter space using the bifurcation diagrams in Figure 2.8.

We plot a two-parameter bifurcation diagram in the g_{Ca}-p_{ER} plane when $g_{\mathrm{K_{Ca}}}$=4 in Figure 2.8(b). As we pointed out, the role of g_{Ca} on the model solutions in the g_{Ca}-$g_{\mathrm{K_{Ca}}}$ plane in Figure 2.8(a) can also be seen in Figure 2.8(b), namely that the complex periodic orbits become bursting solutions as g_{Ca} increases. Additionally, as p_{ER} increases, the number of plateau oscillations of periodic orbits decreases.

Figure 2.8(a) shows that the IHC model produces complex periodic orbits with two large (normal) spikes (*2+N* solutions) in the region where $g_{\mathrm{K_{Ca}}} \in [1.5, 2.5]$ and $g_{\mathrm{Ca}} \in [2.1, 2.3]$ when p_{ER}=0.0004. As p_{ER} increases, the parameter value of $g_{\mathrm{K_{Ca}}}$ decreases while the parameter values of g_{Ca} increase so that the IHC model produces *2+N* solutions. For example; if we increase the rate of CICR to p_{ER}=0.003, then *2+N* solutions can be found in the range of $g_{\mathrm{K_{Ca}}} \in [0.55, 0.65]$ and $g_{\mathrm{Ca}} \in [5.5, 6.5]$.

The IHC model exhibits complex periodic orbits with two large (normal) spikes (*2+N* solutions) in smaller parameter regions comparing to *1+N* and bursting solutions as shown in Figure 2.8(a). Therefore, it is expected that some parameter sections do not contain any *2+N* solutions. For example, the two-parameter bifurcation diagram

(a) p_{ER}=0.0004

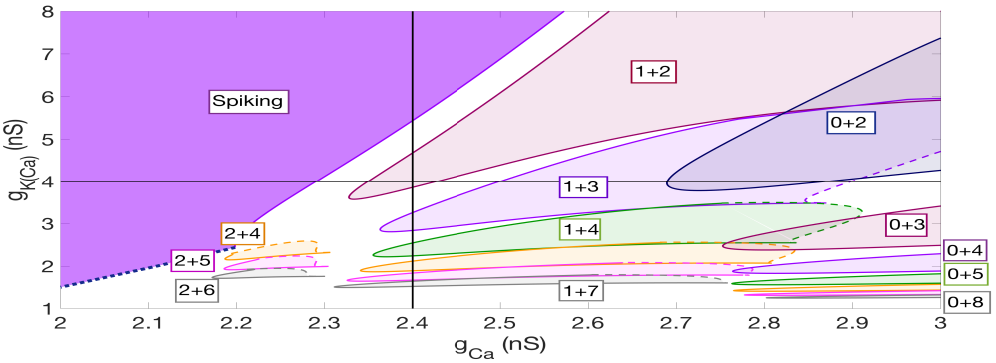

(b) $g_{K_{Ca}}$=4

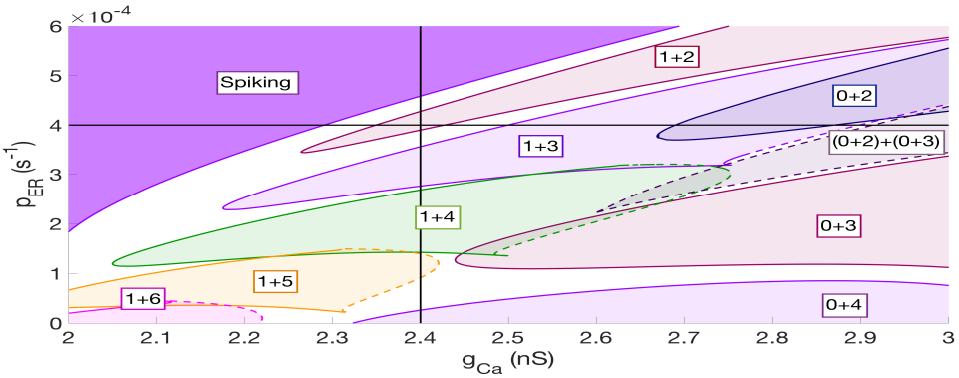

(c) g_{Ca}=2.4

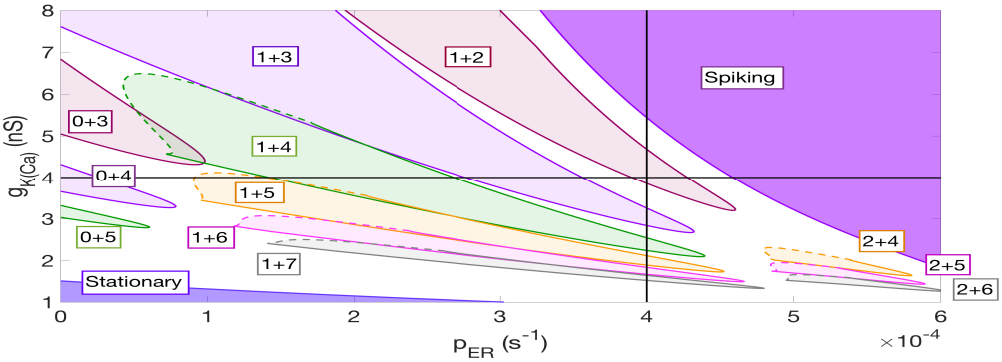

FIGURE 2.8. Two-parameter bifurcation diagrams of the IHC model when p_{ER}=0.0004 (a), $g_{K_{Ca}}$=4 (b) and g_{Ca}=2.4 (c). Stable regions of solutions are delimited by tracing the period-doubling bifurcations (solid curves) and saddle-node bifurcation of periodic solutions (dashed curves) and are coloured accordingly. Torus bifurcations of the branches originating from Hopf bifurcations are indicated by dashed dotted curves. Black lines indicate the cross-sections.

in Figure 2.8(b) does not contain any *2+N* solutions since the parameter $g_{\mathrm{K_{Ca}}}$=4 is not sufficiently small. Therefore, we conclude that the IHC model produces complex solutions with 2 (or more) large spikes for smaller values of $g_{\mathrm{K_{Ca}}}$ ($g_{\mathrm{K_{Ca}}}$<3). We also check the relative contributions of the three parameters on *2+N* solutions and find the intervals $g_{\mathrm{K_{Ca}}} \in [0.55, 3]$, $p_{\mathrm{ER}} \in [0, 0.0031]$ and $g_{\mathrm{Ca}} \in [2, 6]$ that indicate the maximum and minimum values for the parameters having *2+N* solutions in the IHC model.

Figure 2.8(c) is the two-parameter bifurcation diagram in the p_{ER}-$g_{\mathrm{K_{Ca}}}$ plane, which was orginally presented in [31] and reproduced here. As the parameter p_{ER} increases, the number of large spikes in complex periodic orbits increases for the intermediate values of p_{ER}. This two-parameter figure also supports that the complex periodic orbits with two large (normal) spikes can be found in the region where $g_{\mathrm{K_{Ca}}} \in [1.5, 2.5]$ and $p_{\mathrm{ER}} \in [0.0005, 0.0006]$ when g_{Ca}=2.4.

When we increased the parameter g_{Ca}, the IHC model exhibited *2+N* solutions for smaller values of the parameter $g_{\mathrm{K_{Ca}}}$ and larger values of the parameter p_{ER}. This is also similar to the complex solutions with one large spike. For example, we consider two values of the parameter g_{Ca}, which are g_{Ca}=2.4 and g_{Ca}=6, the IHC model produces *1+N* solutions in the parameter range of $[0, 0.0005] \times [1.5, 40]$ in the p_{ER}-$g_{\mathrm{K_{Ca}}}$ plane when g_{Ca}=2.4 shown in Figure 2.8(c). If we increase the parameter g_{Ca} to 6, then the model produces *1+N* solutions in the parameter range of $[0.0028, 0.0030] \times [0.6, 0.7]$ in the p_{ER}-$g_{\mathrm{K_{Ca}}}$ plane. This indicates that if we increase the parameter g_{Ca} in the model, the parameter p_{ER} must be increased while the parameter $g_{\mathrm{K_{Ca}}}$ is decreased accordingly in order to get similar behaviour (*1+N* solutions in this case).

2.2.3 Aperiodic Model Solutions

In Figure 2.8, we showed the stable regions for the periodic orbits in different colours according to the numer of spikes of the periodic solutions. There are also regions in white where we could not obtain stable periodic solutions. It is important to mention that the region of solutions were determined by tracing the SNp and PD bifurcations.

There are further PD bifurcations (second, third etc.) that would cover only a very tiny area near the PD (solid) curves on the two-parameter bifurcation diagrams in Figure 2.8, which is not shown in the diagrams.

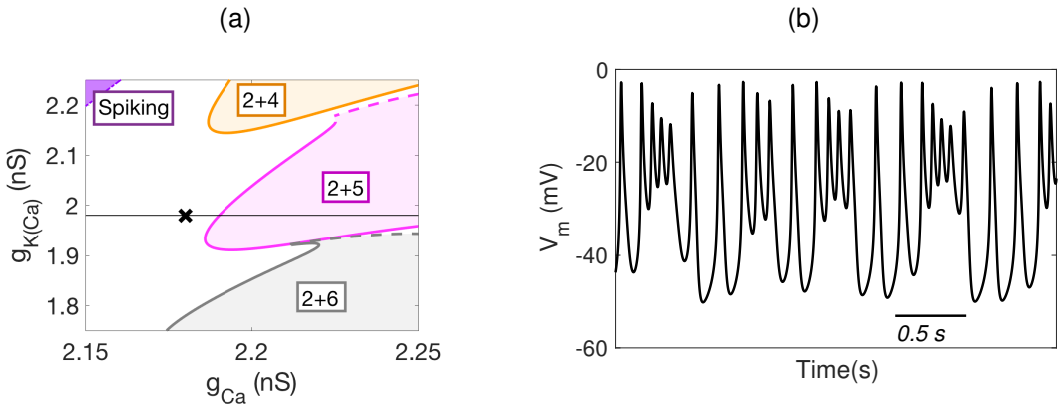

FIGURE 2.9. (a) Magnification of the two-parameter diagram in Figure 2.7. The black cross corresponds to the parameters of the aperiodic pattern. (b) A time series plot of the aperiodic pattern.

We consider an aperiodic pattern whose location is indicated by a black cross (g_{Ca}=2.18 and $g_{\mathrm{K(Ca)}}$=1.98) in the two parameter bifurcation diagram on (g_{Ca}-$g_{\mathrm{K(Ca)}}$)-plane when p_{ER}=0.0004 in Figure 2.9. We compute the time series and phase-space plots of the pattern and three Poincaré sections at V_{m}=-15 mV, V_{m}=-30 mV and V_{m}=-45 mV, respectively. We can gain an insight into the irregular pattern of the trajectory using the Poincaré sections in Figure 2.10(a). Such Poincaré sections suggest that this pattern arises from strong dissipation, which results in the contraction of areas in the phase space [2, 82].

So far we have only showed the Poincaré sections of the aperiodic time series. However, chaos arises from the exponential growth of infinitesimal perturbations, which is indicated by the Lyapunov exponents [20, 28]. Therefore, calculating Lyapunov exponents gives more information about the nature of such trajectories i.e. Kaplan-Yorke dimension, dissipation rate etc. [42, 57, 107] and could help gaining an insight into the aperiodic behaviour of the IHC model. Therefore, we calculate the spectrum of

the dynamic Lyapunov exponents using variational equations [106] in Figure 2.10(b) for the given aperiodic time series. The positive exponent λ_1 indicates the chaotic behaviour of the model with the given parameters.

Poincaré sections of a periodic orbit has only a finite number fixed points. A quasi-periodic orbit, on the other hand, forms a closed-curve (see Figure 2.2(d)) with an infinite number of points. Therefore, the Poincaré sections and the spectrum of Lyapunov exponents in Figure 2.10 give us an indication about the nature of such irregular patterns, which are found in the white regions seen in the two-parameter bifurcation diagrams. Due to the period-doubling bifurcation as the control parameter g_{Ca} decreases, this implies a possibility of a period-doubling cascade which underlies the observed chaotic pattern. There are also aperiodic solutions near the quasi-periodic oscillations, which could indicate the scenario of a quasi-periodic route to chaos [29]. This suggests a future direction for research in order to gain a better understanding of the chaotic attractors of the IHC model.

2.3 Conclusion

Immature inner hair cells' action potentials are calcium-dependent. In this chapter we investigated the relative contribution of three important parameters, namely $g_{\mathrm{K_{Ca}}}$, p_{ER} and g_{Ca}, that are directly involved in calcium dynamics regulation in the IHC model, by performing a numerical bifurcation analysis in order to understand the effects of varying these parameters on the model solutions.

The role of varying the two parameters ($g_{\mathrm{K_{Ca}}}$ and p_{ER}) in shaping the pattern of electrical activity in immature inner hair cells were studied when g_{Ca} is fixed [31, 90]. An atlas of stable solutions was presented in a two-parameter bifurcation diagram in [31], where they traced only period-doubling bifurcations (PDs) of various isola, highlighting the corresponding stable regions in the p_{ER}-$g_{\mathrm{K_{Ca}}}$ plane. However, the one-parameter bifurcation diagram in Figure 2.3(a) shows that the stable parts of the

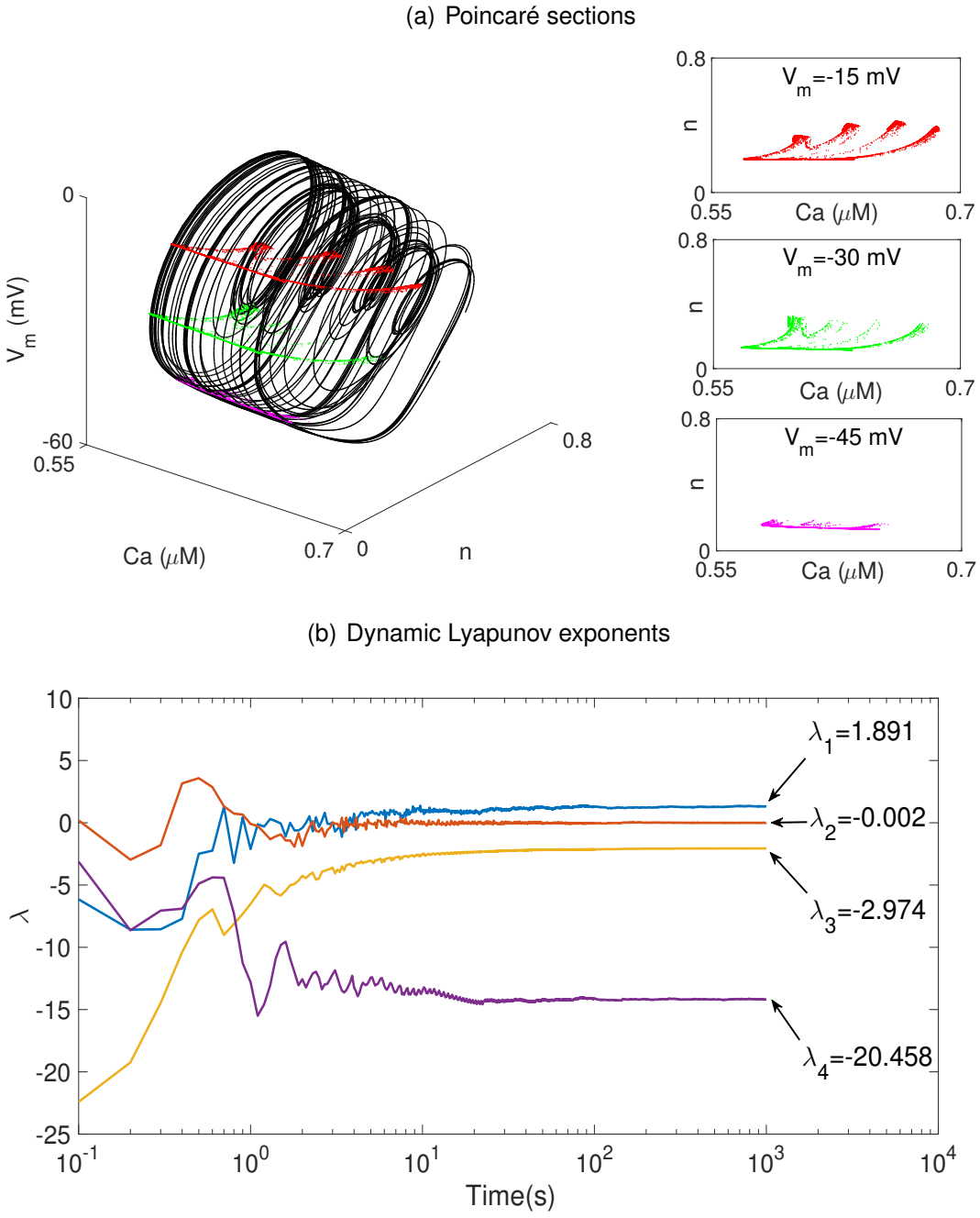

FIGURE 2.10. (a) Three Poincaré sections of the chaotic time series shown in Figure 2.9 are computed at V_m=-15 mV, V_m=-30 mV and V_m=-45 mV. (b) The spectrum of the dynamic Lyapunov exponents.

isola can sometimes be bounded by both PD and SNp bifurcations. Therefore, we continued the SNp bifurcations in two parameters in our bifurcation analysis in this

chapter. Additionally, although these bifurcation curves become very close to each other, enclosing the stable regions of periodic solutions, they do not merge. As these curves become closer and closer, one of the multipliers crosses the unit circle at a specific point [54].

However, the effects of changing the parameter g_{Ca} (the maximum calcium channel conductance) had not yet been studied. Therefore, prior to the investigation of the relative contribution of the three parameters, we started to explore the effects of varying g_{Ca} by fixing the two parameters $g_{\mathrm{K_{Ca}}}$ and p_{ER}. We showed that the number of large (normal) spikes of complex periodic orbits decreases and eventually complex solutions become bursting solutions as g_{Ca} increases. Furthermore, the plateau oscillations of bursting solutions become harder to visualise with larger values of g_{Ca}. In addition to this, the intracellular calcium concentration increases significantly as g_{Ca} increases, which leads to a higher calcium intake through the cell membrane.

We confirmed that the periodic orbits, whose total number of oscillations is fixed, lie on the same isola [31], which indicates that those solutions are connected in the parameter space. Therefore, we tried to understand the behaviour of periodic orbits according to changes of the three parameters using several two-parameter bifurcation diagrams shown in Figure 2.8.

Increasing the parameter g_{Ca}, *2+N* solutions of the model are detected for smaller values of the parameter $g_{\mathrm{K_{Ca}}}$ and larger values of the parameter p_{ER}. We noted that this behaviour is also similar to the complex solutions with one large spike and bursting solutions. Therefore, in order to estimate the parameters for similar types of solution (complex solutions with two large spikes, complex solutions with one large spike or bursting), if the parameter g_{Ca} increases, then the parameter p_{ER} must be increased while the parameter $g_{\mathrm{K_{Ca}}}$ is decreased accordingly. For instance, we showed the parameter region of *1+N* solutions in the p_{ER}-$g_{\mathrm{K_{Ca}}}$ plane when g_{Ca}=2.4 was $[0, 0.0005] \times [1.5, 40]$, partially shown in Figure 2.8(c). The parameter range will

be $[0.0028, 0.0030] \times [0.6, 0.7]$ when g_{Ca}=6. Thus, our numerical bifurcation analysis here helps to estimate the parameter regions of the IHC model solutions according to changes in the three parameters.

However, there are some limitations of our analysis and further questions, which remain open. Firstly, since we have considered two-parameter sections of the three dimensional parameter space, we do not have a complete view of solutions in 3D space to display how periodic solutions, whose total number of spikes is equal, connect and disconnect when they have different numbers of large and small spikes. Secondly, since we did not continue the homoclinic bifurcations on the two-parameter bifurcation diagrams, we do not know if these bifurcations explain the relation between the branches originating from Hopf bifurcations and isolas. Thirdly, as we have shown in Figure 2.1, the IHC model produces quasi-periodic motion near the torus bifucation. As g_{Ca} increases, the model solutions become complex periodic orbits. However, we could not identify the relation between the quasi-periodic and complex solutions in the IHC model.

Despite unanswered questions, we are now able to estimate what happens when we vary the three parameters in the model. Next, we would like to simplify the four-dimensional IHC model by reducing its dimension and compare it with the original model. These parameter estimations will also help us to identify the ranges for the parameters that result in different types of periodic solutions (regular, bursting and complex) of the IHC model.

CHAPTER 3

DIMENSION REDUCTION OF THE IHC MODEL

The Inner Hair Cell (IHC) Model was introduced in Chapter 1 while its oscillatory behaviour over a large range of three dimensional parameter space of parameters, namely g_{Ca}, $g_{\mathrm{K_{Ca}}}$ and p_{ER}, was studied in detail in Chapter 2 by considering the two-parameter sections of the three dimensional parameter space. The states variables of the model are the membrane potential V_m, an activation (n) and an inactivation (h) variables for the voltage-gated K^+ channel, and the intracellular Ca^{2+} concentration Ca=$[Ca^{2+}]_i$. In this chapter, we show that it is possible to reduce the dimensions of the original IHC Model that allows to deal with a simpler (three dimensional) model without losing the valuable dynamic features of the original model. This enables us to use this simpler reduced (3D) IHC model for further analysis instead of the original (4D) IHC model. In Chapter 4, we will consider the reduced IHC model and carry out slow-fast analysis of the IHC model.

3.1 Determining the Slowest Variable of the Model

Dimension reduction of mathematical models of biological systems has a long history [11]. In particular, recent models contain many state variables [58] due to the highly complex biological processes the models describe. In order to understand the basic dynamical behaviour of such models, model reduction is vital to reduce the complexity and approximate the behaviour of the original models by constructing simplified models. Thus, methods of dimension reduction and model simplification are still crucial topics in the mathematical modelling of biological systems.

A recent review paper on methods of model reduction [85] provides an up-to-date overview for reducing the dimensions of biological models. We will consider the *timescale exploitation methods* to help reduce the dimension of the IHC model by fixing the time derivative of the slowest variable to zero, which will make the slowest variable a constant in the model.

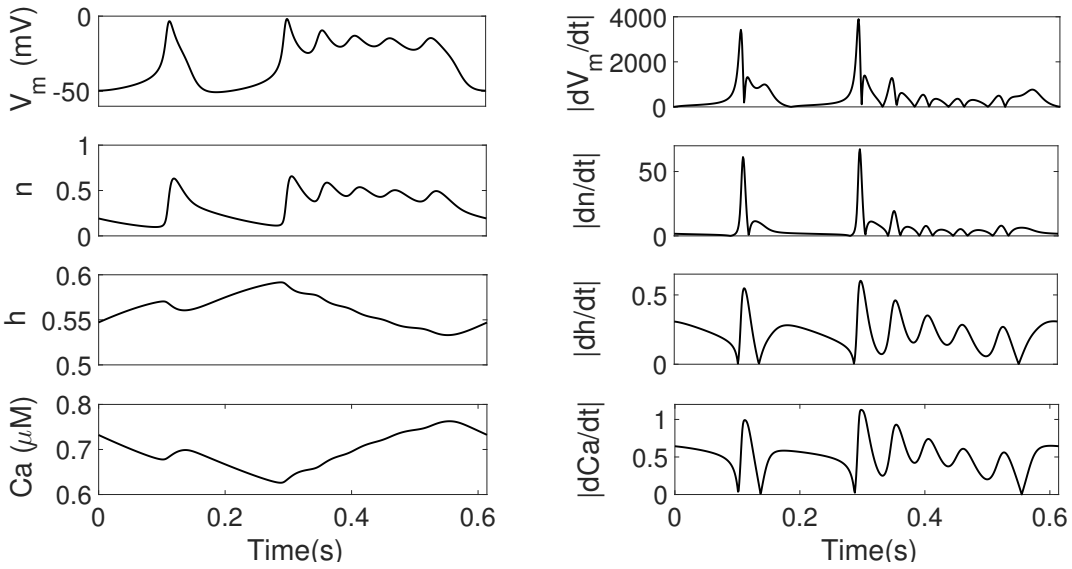

FIGURE 3.1. Time series of the state variables and absolute time derivatives of a periodic orbit corresponding to the parameters g_{Ca}=2.4, $g_{\mathrm{K_{Ca}}}$=1.98 and p_{ER}=0.0004. All the other parameters are fixed and given in Table 1.1 in Chapter 1.

Timescale exploitation methods are based on differences between time scales of model variables. We have plotted the time courses and absolute values of the time derivatives of the four variables, which are computed by the numerical simulation package XPPAUT [22], in Figure 3.1, to indicate the differences in time scales of the IHC model variables. It is seen from the amplitude ranges of the time series and their derivatives that the variables h and Ca change on relatively slower time scales than the variables V_{m} and n.

We will also calculate the time scale constants by nondimensionalising the IHC model equations in greater detail in the following subsection to check and verify the fast and slow variables of the IHC model. Additionally, we will use the nondimensional IHC model to gain an insight into the speed of variables according to changes of the model parameters and analyse their periodic behaviour by splitting the model into the fast and slow subsystems in Chapter 4.

3.1.1 Nondimensionalisation of the IHC Model

The IHC model intoduced in Chapter 1 is biophysical and hence the variables representing the membrane potential (V_{m}) and the intracellular calcium (Ca) as well as all model parameters, have dimensions. We would like to remove the dimensions of the state variables of the model to estimate the speed of the variables. Therefore, we can approximate the model by considering the rate of change of the slowest variable in time is negligible, which simplifies the four-dimensional model to a three-dimensional model. Therefore, we can deal with a simplified model having fewer state variables than the original (4D) IHC model and no longer need to consider the phase space projections of the trajectories and periodic solutions of the model.

Nondimensionalisation is a process which eliminates the physical units of the variables in the model [67]. There are several objectives in making biophysical models nondimensional. Our purpose in creating a nondimensionalisation version of the IHC model is to access the characteristic time scale differences between the variables.

Secondly, estimating the typical time scales of the variables in the IHC model enables us to identify the important parameters that control the time scales and how the model variables are related to each other. In Chapter 4, we will consider the nondimensional reduced IHC model to apply a fast-slow analysis [78, 94].

3.1.2 Dimensionless Model Equations

The IHC model is defined by a set of four ordinary differential equations (ODEs) in Chapter 1 as

$$\begin{aligned} C_{\mathrm{m}}\frac{\mathrm{d}V_{\mathrm{m}}}{\mathrm{d}t} &= -I_{\mathrm{Ca}}(V_{\mathrm{m}},Ca) - I_{\mathrm{K}}(V_{\mathrm{m}},n) - I_{\mathrm{K_{Ca}}}(V_{\mathrm{m}},Ca) - I_{\mathrm{leak}}(V_{\mathrm{m}}) \\ \frac{\mathrm{d}n}{\mathrm{d}t} &= \frac{n_\infty(V_{\mathrm{m}})-n}{\tau_{\mathrm{n}}(V_{\mathrm{m}})} \\ \frac{\mathrm{d}h}{\mathrm{d}t} &= \frac{h_\infty(V_{\mathrm{m}})-h}{\tau_{\mathrm{h}}} \\ \frac{\mathrm{d}Ca}{\mathrm{d}t} &= f_{\mathrm{c}}\left(-\alpha I_{\mathrm{Ca}}(V_{\mathrm{m}}) - \frac{k_{\mathrm{PMCA}}Ca^2}{Ca^2+K_{\mathrm{p}}^2}\right) - k_{\mathrm{SERCA}}Ca + p_{\mathrm{ER}}(Ca_{\mathrm{ER}}-Ca) \end{aligned} \tag{3.1}$$

where V_{m} denotes the membrane potential, (n) the activation and (h) the inactivation variable for the voltage-gated K^+ channel and Ca=$[Ca^{2+}]_i$ the intracellular Ca^{2+} concentration. (The full model equations including the ion current equations and the parameters can be found in Chapter 1.)

Dimensionless Membrane Voltage Equation (v):

In order to eliminate the dimensions of the membrane voltage equation in (3.1), we have to rescale the state variables V_{m} and Ca as well as time t by some scaling constants that have the same dimensions as variables V_{m}, Ca and t. Additionally, if we use the typical amplitude ranges for the state variables as these rescaling constants, the nondimensional state variables will vary between 0 and 1.

We have checked that the typical values of the membrane potential and the intracellular calcium of the IHC model are $V_{\mathrm{m}} \in [-60, 0]$ mV and $Ca \in [0, 1]$ μM. Therefore, we

consider the suitable choices for the membrane voltage and intracellular calcium as Q_{v}=100 mV and Q_{c}=1 μM, respectively.

Rescaling $V_{\mathrm{m}} = vQ_{\mathrm{v}}$, $Ca = cQ_{\mathrm{c}}$ and $t = \tau Q_{\mathrm{t}}$ with $Q_{\mathrm{t}} = 1s$ eliminates the dimensions of V_{m}, Ca and t to get the new dimensionless variables v and c as well as time τ. Therefore, we obtain the dimensionless form of the membrane voltage (v) as

$$\frac{C_{\mathrm{m}}}{Q_{\mathrm{t}} g_{\mathrm{max}}} \frac{\mathrm{d}v}{\mathrm{d}\tau} = -\hat{I}_{\mathrm{Ca}}(v,c) - \hat{I}_{\mathrm{K}}(v,n) - \hat{I}_{\mathrm{K_{Ca}}}(v,c) - \hat{I}_{\mathrm{leak}}(v) \tag{3.2}$$

where g_{max}=max$\{g_{\mathrm{Ca}}, g_{\mathrm{K}}, g_{\mathrm{K_{Ca}}}, g_{\mathrm{leak}}\}$ and the dimensionless currents $\hat{I}_X = \frac{I_X}{g_{\mathrm{max}} Q_{\mathrm{v}}}$ with $X \in$\{Ca, K, $\mathrm{K_{Ca}}$, leak\}.

Scaling the conductances by g_{max} results in all terms on the right hand side (RHS) of the equation to be bounded (in absolute values) by one. Therefore, the typical time scale for the membrane voltage v is given by $\frac{C_{\mathrm{m}}}{Q_{\mathrm{t}} g_{\mathrm{max}}}$.

Dimensionless Calcium Equation (c):

Let us recall the intracellular calcium equation of the reduced IHC model given in (3.1).

$$\frac{\mathrm{d}Ca}{\mathrm{d}t} = f_{\mathrm{c}} \left(-\alpha I_{\mathrm{Ca}}(V_{\mathrm{m}}, Ca) - \phi(Ca)Ca - (\hat{k}_{\mathrm{SERCA}} + \hat{p}_{\mathrm{ER}})Ca + \hat{p}_{\mathrm{ER}} Ca_{\mathrm{ER}} \right)$$

where $\hat{k}_{\mathrm{SERCA}} = \frac{k_{\mathrm{SERCA}}}{f_{\mathrm{c}}}$, $\hat{p}_{\mathrm{ER}} = \frac{p_{\mathrm{ER}}}{f_{\mathrm{c}}}$ and $\phi(Ca) = \frac{k_{\mathrm{PMCA}} Ca}{Ca^2 + K_{\mathrm{p}}^2}$.

Scaling $V_{\mathrm{m}} = vQ_{\mathrm{v}}$, $Ca = cQ_{\mathrm{c}}$ and $t = \tau Q_{\mathrm{t}}$, we obtain the dimensionless form of the calcium equation as:

$$\frac{\mathrm{d}c}{Q_{\mathrm{t}} \mathrm{d}\tau} = f_{\mathrm{c}} \left(-\xi \bar{I}_{\mathrm{c}}(v,c) - \Phi \bar{\phi}(c)c - (\hat{k}_{\mathrm{SERCA}} + \hat{p}_{\mathrm{ER}})c + \hat{p}_{\mathrm{ER}} c_{\mathrm{ER}} \right) \tag{3.3}$$

where $\xi = \frac{\alpha g_{\mathrm{Ca}} Q_{\mathrm{v}}}{Q_{\mathrm{c}}}$, $\bar{I}_{\mathrm{c}}(v,c) = \frac{I_{\mathrm{Ca}}(vQ_{\mathrm{v}}, cQ_{\mathrm{c}})}{g_{\mathrm{Ca}} Q_{\mathrm{v}}}$, $\bar{\phi}(c) = \frac{\tilde{\phi}(c)}{\Phi}$ with $\Phi = \max_{0 \le c \le 1} \tilde{\phi}(c)$ and $c_{\mathrm{ER}} = \frac{Ca_{\mathrm{ER}}}{Q_{\mathrm{c}}}$.

Using the parameters specified in Chapter 1, we can plot the function $\tilde{\phi}(c)$ over the range of c

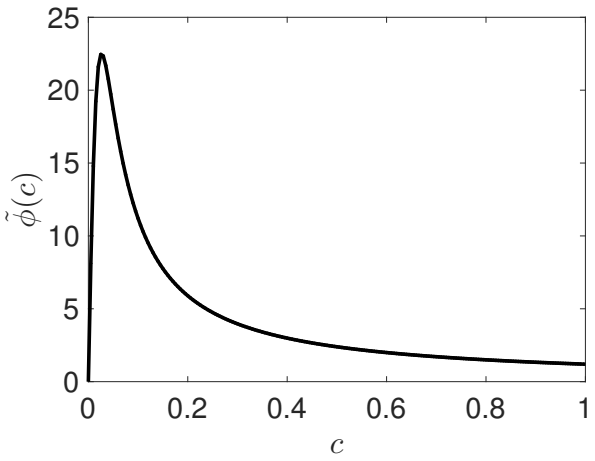

FIGURE 3.2. Graph of the function $\tilde{\phi}(c)$.

We see that the function $\tilde{\phi}(c)$ in (3.3) has a maximum of about 22. Hence, the function $\bar{\phi}(c)$ on the RHS of the equation (3.3), which is $\bar{\phi}(c) = \frac{\tilde{\phi}(c)}{\Phi}$ with $\Phi = \max_{0\le c\le 1}\tilde{\phi}(c)$, will be bounded by one.

In order to make all terms on the RHS of the equation (3.3) bounded (in absolute values) by one, we calculate the values of constants on the RHS. Thus, we get

$$
\begin{aligned}
&(\hat{k}_{\mathrm{SERCA}} + \hat{p}_{\mathrm{ER}}) \quad \text{is of an order} \quad O(10^3),\\
&(\hat{p}_{\mathrm{ER}} c_{\mathrm{ER}}) \quad \text{is of an order} \quad O(10^3) \quad \text{and}\\
&\xi = \frac{\alpha g_{\mathrm{Ca}} Q_{\mathrm{v}}}{Q_{\mathrm{c}}} \quad \text{is of an order} \quad O(10^4)
\end{aligned}
$$

with the model parameters given in 1.1 in Chapter 1 and considering the ranges of the bifurcation parameters p_{ER} and g_{Ca} in Chapter 2.

We identify ξ as the largest constant in the RHS of the calcium equation (3.3). Accordingly, if we divide the RHS of (3.3) by ξ, all terms on the RHS will be bounded (in absolute values) by one. Therefore, we get

$$
\frac{Q_{\mathrm{c}}}{Q_{\mathrm{t}} f_{\mathrm{c}} \alpha g_{\mathrm{Ca}} Q_{\mathrm{v}}} \frac{\mathrm{d}c}{\mathrm{d}\tau} = -\bar{I}_{\mathrm{c}}(v,c) - \zeta_1 \bar{\phi}(c) c - \zeta_2 c + \zeta_3 \tag{3.4}
$$

where $\zeta_1 = \frac{\Phi Q_c}{\alpha g_{Ca} Q_v}$, $\zeta_2 = \frac{(\hat{k}_{SERCA} + \hat{p}_{ER}) Q_c}{\alpha g_{Ca} Q_v}$ and $\zeta_3 = \frac{\hat{p}_{ER} c_{ER} Q_c}{\alpha g_{Ca} Q_v}$.

Dimensionless Activation Variable Equation (n):

The equation of the activation variable (n) associated with the voltage-dependent potassium (K^+) channel is given by

$$\frac{dn}{Q_t d\tau} = \frac{1}{\tau_n(v)}(n_\infty(v) - n) \tag{3.5}$$

As we have seen, the variable n is already dimensionless. Since we would like to bound the RHS of the of the IHC model in (3.1) as a result of the process of nondimensionalisation, we need only to check if the right hand side of (3.5) is bounded by one.

We have $0 \leq n \leq 1$ and $0 \leq n_\infty(v) \leq 1$, hence $|n - n_\infty(v)| \leq 1$. Figure 3.3 shows the behaviour of the inverse of the voltage dependent time scale function of the gating variable, which is given by

$$\frac{1}{\tau_n(v)} = (0.0022 + 0.0029 e^{-v Q_v / 14.3})^{-1} \tag{3.6}$$

Let $\hat{T}_n := \max_{-0.6 \leq v \leq 0} \frac{1}{\tau_n(v)}$. Therefore, we can rescale the function $\frac{1}{\tau_n(v)}$ by its maximum to get a new dimensionless time scale function, which is bounded (in absolute values) by one; i.e.

$$\frac{1}{\hat{\tau}_n(v)} := \frac{1/\tau_n(v)}{\hat{T}_n}$$

Hence, the equation of the activation variable n in (3.5) becomes

$$\frac{1}{\hat{T}_n Q_t} \frac{dn}{d\tau} = \frac{1}{\hat{\tau}_n(v)}(n_\infty(v) - n) \tag{3.7}$$

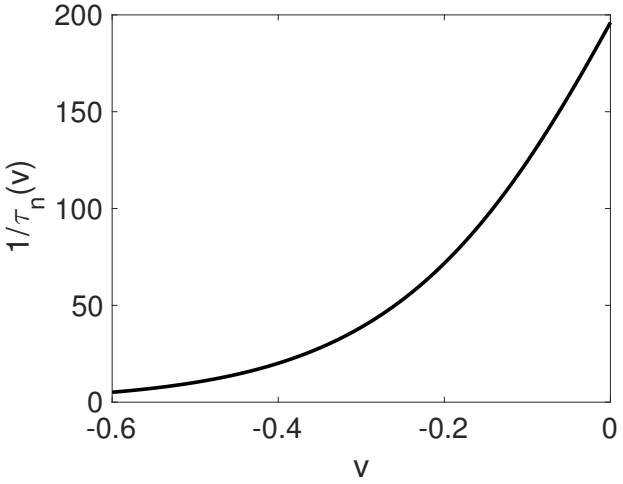

FIGURE 3.3. Graph of the function $\frac{1}{\tau_{\mathrm{n}}(v)}$ in (3.6).

This scaling makes the RHS of the equation dimensionless and bounded (in absolute values) by one. Therefore, the typical time scale for the activation variable is given by $\frac{1}{\hat{T}_n Q_{\mathrm{t}}}$, which is equal to 0.0051.

Dimensionless Inactivation Variable Equation (h):

The rate of change in the inactivation variable h is represented by

$$\frac{\mathrm{d}h}{\mathrm{d}t} = \frac{h_\infty(V_{\mathrm{m}}) - h}{\tau_{\mathrm{h}}} \tag{3.8}$$

$$\frac{\tau_{\mathrm{h}}}{Q_{\mathrm{t}}}\frac{\mathrm{d}h}{\mathrm{d}\tau} = h_\infty(v) - h \tag{3.9}$$

Similar to the activation variable (n), the inactivation variable (h) is already dimensionless, and moreover its time constant is already given in the model by τ_{h}, which is equal to 0.55. Therefore, the typical time scale for the inactivation variable is given by $\frac{\tau_{\mathrm{h}}}{Q_{\mathrm{t}}}$, which is equal to 0.55.

Thus, the dimensionless form of the IHC model in (3.1) can be written as

$$\begin{aligned}
\frac{C_\mathsf{m}}{Q_\mathsf{t} g_\mathsf{max}}\frac{\mathrm{d}v}{\mathrm{d}\tau} &= -\hat{I}_\mathsf{Ca}(v,c) - \hat{I}_\mathsf{K}(v,n) - \hat{I}_{\mathsf{K_{Ca}}}(v,c) - \hat{I}_\mathsf{leak}(v) \\
\frac{1}{\hat{T}_n Q_\mathsf{t}}\frac{\mathrm{d}n}{\mathrm{d}\tau} &= \frac{1}{\hat{\tau}_\mathsf{n}(v)}(n_\infty(v) - n) \\
\frac{\tau_\mathsf{h}}{Q_\mathsf{t}}\frac{\mathrm{d}h}{\mathrm{d}\tau} &= h_\infty(V_\mathsf{m}) - h \\
\frac{Q_\mathsf{c}}{Q_\mathsf{t} f_\mathsf{c} \alpha g_\mathsf{Ca} Q_\mathsf{v}}\frac{\mathrm{d}c}{\mathrm{d}\tau} &= -\bar{I}_\mathsf{c}(v,c) - \zeta_1 \bar{\phi}(c) c - \zeta_2 c + \zeta_3
\end{aligned} \tag{3.10}$$

where

$$g_\mathsf{max} = \max\{g_\mathsf{Ca}, g_\mathsf{K}, g_{\mathsf{K_{Ca}}}, g_\mathsf{leak}\}, \quad \hat{I}_\mathsf{X} = \frac{I_X}{g_\mathsf{max} Q_\mathsf{v}}, \quad X \in \{\mathsf{Ca}, \mathsf{K}, \mathsf{K_{Ca}}, \mathsf{leak}\}$$

$$\frac{1}{\hat{\tau}_n(v)} = \frac{1/\tau_\mathsf{n}(v)}{\hat{T}_n} \quad \text{where} \quad \hat{T}_n = \max_{-0.6 \le v \le 0} \frac{1}{\tau_\mathsf{n}(v)} \quad \text{and}$$

$$\bar{I}_\mathsf{c}(v,c) = \frac{I_\mathsf{Ca}(v,c)}{g_\mathsf{Ca} Q_\mathsf{v}}, \quad \zeta_1 = \frac{\Phi Q_\mathsf{c}}{\alpha g_\mathsf{Ca} Q_\mathsf{v}}, \quad \zeta_2 = \frac{(\hat{k}_\mathsf{SERCA} + \hat{p}_\mathsf{ER}) Q_\mathsf{c}}{\alpha g_\mathsf{Ca} Q_\mathsf{v}}, \quad \zeta_3 = \frac{\hat{p}_\mathsf{ER} c_\mathsf{ER} Q_\mathsf{c}}{\alpha g_\mathsf{Ca} Q_\mathsf{v}}$$

Now all terms on the right hand side of (3.10) are bounded (in absolute values) by one. Therefore, the coefficients of the time derivatives of the nondimensional IHC model in (3.10) indicate the relative rates of evolution of the state variables, which are

$$\hat{\tau}_v := \frac{C_\mathsf{m}}{Q_\mathsf{t} g_\mathsf{max}}, \quad \hat{\tau}_n := \frac{1}{T_n Q_\mathsf{t}}, \quad \hat{\tau}_h := \frac{\tau_\mathsf{h}}{Q_\mathsf{t}}, \quad \hat{\tau}_c := \frac{Q_\mathsf{c}}{Q_\mathsf{t} f_\mathsf{c} \alpha g_\mathsf{Ca} Q_\mathsf{v}} \tag{3.11}$$

Considering the scaling parameter values Q_v=100 mV, Q_c=1 μM, Q_t=1 s and the model parameter values given in Chapter 1, the time constants of the IHC model are calculated with the given parameters for the periodic solution shown in Figure 3.1 as $\hat{\tau}_v$=0.0018, $\hat{\tau}_n$=0.0051, $\hat{\tau}_h$=0.55 and $\hat{\tau}_c$=0.14. Therefore, these time scale constants also support that the variable h of the IHC model is the slowest variable.

Additionally, fixing the slowest variable, the reduced IHC model becomes three dimensional. We will investigate the effects of changing model parameters on the time scales of the variables using fast-slow analysis in Chapter 4.

3.1.3 The Reduced (3D) IHC Model

Up to now, we have shown that the state variables V_{m} and n are much faster than the variables Ca and h. Additionally, since the action potentials of the inner hair cells are calcium-dependent, the IHC model no longer exhibits its characteristic solutions such as pseudo-plateau and complex periodic orbits if we assume $\frac{\mathrm{d}Ca}{\mathrm{d}t} = 0$. Therefore, we will consider the case that the state variable h satisfies the condition $\frac{\mathrm{d}h}{\mathrm{d}t} = 0$ in order to reduce the dimension of the four-dimensional IHC model.

The rate of change in the variable h is represented by

$$\frac{\mathrm{d}h}{\mathrm{d}t} = \frac{1}{\tau_{\mathrm{h}}}(h_\infty(V_{\mathrm{m}}) - h) \tag{3.12}$$

where $h_\infty(V_{\mathrm{m}})$ is the steady-state function of h and $\frac{1}{\tau_{\mathrm{h}}}$ is small. As we reviewed the slow-fast analysis in Section 1.2.2, similar to the limit of ϵ, setting $\frac{1}{\tau_{\mathrm{h}}} = 0$ will make $\frac{\mathrm{d}h}{\mathrm{d}t} = 0$. Therefore, we have to consider either $h = h_\infty(V_{\mathrm{m}})$ or the variable h is fixed to a constant.

Firstly, we assumed that h is always in instantaneous equilibrium, thus we replace h by $h_\infty(V_{\mathrm{m}})$, which is called *quasi-steady state (QSS) reduction* [43]. This sets the rate of change in h equal to zero. However, we verified by direct numerical simulations and bifurcation analysis (not shown) that this causes critical changes in the dynamics of the original (4D) IHC model, which means that the reduced (3D) model no longer exhibits bursting and complex oscillations. Since we do not want to lose the important dynamic features of the original model, we cannot assume $h = h_\infty(V_{\mathrm{m}})$. Therefore, secondly, we will consider that h is a constant.

Fixing the variable h to a constant, we get $\frac{\mathrm{d}h}{\mathrm{d}t} = 0$. Therefore, the four dimensional IHC model becomes three dimensional, which we will call the *reduced IHC model*. In order to make a reasonable estimation for a fixed value of the variable h, we considered a large range of the parameters g_{Ca}, $g_{\mathrm{K_{Ca}}}$ and p_{ER}, where the original IHC model exhibits single spikes, quasi-periodic, bursting and complex periodic solutions.

We considered the range of the parameters where the model exhibits oscillations, which are $g_{\mathrm{Ca}} \in [0,50]$, $g_{\mathrm{K_{Ca}}} \in [0,150]$ and $p_{\mathrm{ER}} \in [0,0.0015]$.

In Appendix A, we plotted several one-parameter bifurcation diagrams in these ranges in order to estimate an average value or a midrange value, which is calculated by $(h_{\mathrm{Max}} + h_{\mathrm{Min}})/2$, for h taking into account the possible limit cycles such as single spikes, bursting and complex periodic solutions since the averaged value for h is different for the different type of solutions. As an example, we plot a one-parameter bifurcation diagram using g_{Ca} as a bifurcation parameter in Figure 3.4.

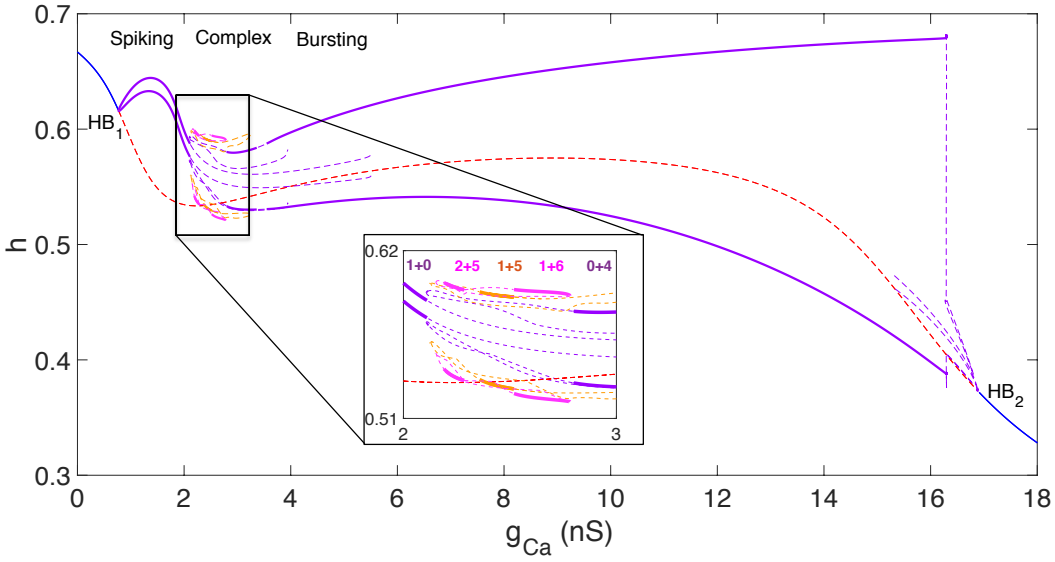

FIGURE 3.4. A one-parameter bifurcation diagram of the IHC model when $g_{\mathrm{K_{Ca}}}$=1.98 and p_{ER}=0.0004. The dynamic state variable h is plotted on the y-axis.

Such one-parameter bifurcation diagrams considering the parameters g_{Ca}, $g_{\mathrm{K_{Ca}}}$ and p_{ER} as bifurcation parameters and the variable h on the y-axis, allow us to determine the range for the constant value of h. Then, we will consider the average of the h values over this range to make an estimation of the constant h value in the reduced model. Based on one-parameter bifurcation analysis results as explained above, we calculated the average value for the variable h as h=0.5732. We will use this value in

the reduced IHC model from now on.

Fixing the variable h=0.5732, we are able to introduce the reduced three dimensional IHC model. The reduced IHC model has three state variables; namely, the membrane potential V_m, an activation variable (n) for the voltage-gated K^+ channel, and the intracellular Ca^{2+} concentration Ca=$[Ca^{2+}]_i$. The model equations are

$$\begin{aligned} C_{\mathrm{m}}\frac{\mathrm{d}V_{\mathrm{m}}}{\mathrm{d}t} &= -I_{\mathrm{Ca}}(V_{\mathrm{m}},Ca) - I_{\mathrm{K}}(V_{\mathrm{m}},n) - I_{\mathrm{K_{Ca}}}(V_{\mathrm{m}},Ca) - I_{\mathrm{leak}}(V_{\mathrm{m}}) \\ \frac{\mathrm{d}n}{\mathrm{d}t} &= \frac{n_\infty(V_{\mathrm{m}}) - n}{\tau_{\mathrm{n}}(V_{\mathrm{m}})} \\ \frac{\mathrm{d}Ca}{\mathrm{d}t} &= f_{\mathrm{c}}\left(-\alpha I_{\mathrm{Ca}}(V_{\mathrm{m}}) - \frac{k_{\mathrm{PMCA}}Ca^2}{Ca^2+K_{\mathrm{p}}^2}\right) - k_{\mathrm{SERCA}}Ca + p_{\mathrm{ER}}(Ca_{\mathrm{ER}} - Ca) \end{aligned} \tag{3.13}$$

Balance equations for the ion currents, other sub-functions and the parameters of the reduced IHC model in (3.13) can be found in Chapter 1.

3.2 Validation of the Reduced (3D) against the Original (4D) IHC Model

In this section, we will investigate the behaviour of the reduced (3D) IHC model solutions according to the changes of the parameters g_{Ca}, $g_{\mathrm{K(Ca)}}$ and p_{ER}. Similar to the analysis done for the original (4D) IHC model in Chapter 2, we will continue the period-doubling (PDs) and saddle-node of periodic (SNp) bifurcations in two parameters to identify the stable regions of the periodic solutions of the reduced IHC model. To be consistent in our analyses, we will use the same set of parameters as the original IHC model in Chapter 2 to perform the numerical bifurcation analysis in this section.

3.2.1 Behaviour of the Reduced Model Trajectories

We showed the effect of varying the parameter g_{Ca} on the original IHC model solutions with a one-parameter bifurcation diagram in Chapter 2. The original IHC model

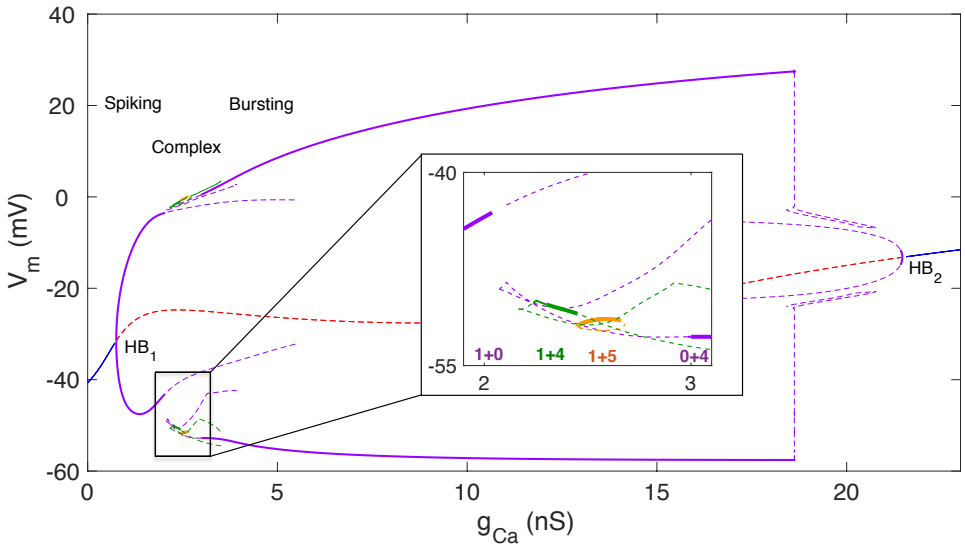

FIGURE 3.5. A one-parameter bifurcation diagram of the reduced (3D) IHC model in the parameter g_{Ca}. The other two parameters are fixed to $g_{\mathrm{K_{Ca}}}$=1.98 and p_{ER}=0.0004 (h=0.5732 is fixed).

exhibits single spike solutions for smaller values of g_{Ca}. As g_{Ca} increases, we showed that the original model generates complex periodic orbits for intermediate values of g_{Ca}. Increasing the parameter g_{Ca} results in the original IHC model solutions becoming bursting and persists for a relatively large portion of the parameter space (see Figure 2.1 in Chapter 2).

We plot a one-parameter bifurcation diagram of the reduced IHC model using g_{Ca} as the bifurcation parameter in Figure 3.5 considering the parameters $g_{\mathrm{K_{Ca}}}$=1.98 and p_{ER}=0.0004, which were used for the original IHC model in Figure 2.1 in Chapter 2. The bifurcation diagram in Figure 3.5 indicates that the reduced IHC model solutions also follow the pattern observed in the original IHC model, that is single spikes followed by complex and then bursting solutions as g_{Ca} increases.

Additionally, there are some parameter values for which the original and reduced IHC models exhibit periodic solutions with the same total number of spikes. This, of course, is not true in general due to the approximation of the slowest variable h by a fixed

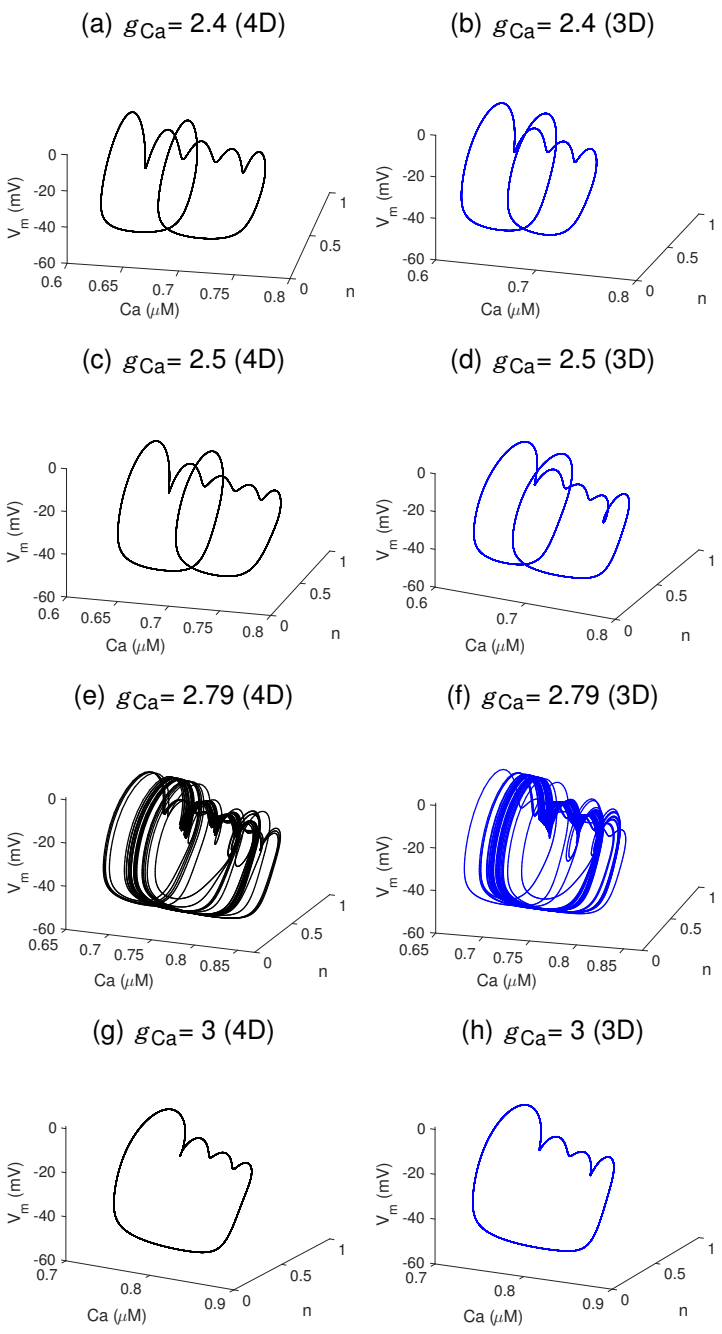

FIGURE 3.6. Phase plots projections of the original (4D) IHC model (black ink) and phase plots of the reduced (3D) IHC model (blue ink) at g_{Ca}= 2.4 (a)&(b), g_{Ca}= 2.5 (c)&(d), g_{Ca}= 2.79 (e)&(f) and g_{Ca}= 3 (g)&(h) (h=0.5732 is fixed).

quantity. As an example, we plot solutions of the original (4D) and reduced (3D) IHC

models for different values of g_{Ca} in Figure 3.6.

Althought the original model generates a complex periodic orbit with one large spike and 5 small spikes (*1+5* solution), the reduced model generates a complex solution with 4 spikes only (*1+4* solution) at g_{Ca}=2.4 shown in Figure 3.6 (a)&(b) respectively. However, for the parameter g_{Ca}=2.5, both models generate the complex *1+5* solutions as shown in Figure 3.6 (c)&(d). This could also be true for the aperiodic trajectories. We plot the 4D and 3D model trajectories when g_{Ca}=2.79 in Figure 3.6 (e)&(f), which is computed for 10 seconds by XPPAUT [22]. We will investigate such aperiodic behaviour at the end of this chapter in more detail. Additionaly, as g_{Ca} increases, both original (4D) and reduced (3D) IHC models start generating bursting solutions with four spikes (*0+4* solution). We plotted such bursting solutions in Figure 3.6 (g)&(h) when g_{Ca}=3.

We showed the reduced IHC model exhibits similar behaviour as the original IHC model, which could both generate the same number of spikes, such as *1+5* or *0+4* solutions, as well as aperiodic oscillations for the same set of parameters. Next, we would like to verify the role of three parameters, namely g_{Ca}, $g_{\mathrm{K(Ca)}}$ and p_{ER}, on the model solutions generating two-parameter bifurcation diagrams using the same parameters used to perform the bifurcation analysis for the original IHC model in Chapter 2.

3.2.2 Mapping the Interaction between g_{Ca}, $g_{\mathrm{K(Ca)}}$ and p_{ER} in the Reduced Model

As in the original IHC model in Chapter 2, we fixed one of the three variables and computed a wide variety of periodic attractors such as normal spiking, bursting and complex periodic orbits with several oscillations. Then, we continue the bifurcations responsible for change in the stability of the periodic solutions in the other two parameters with the continuation package AUTO [18].

We considered the set of parameters used to draw the two-parameter bifurcation

(a) p_{ER}=0.0004

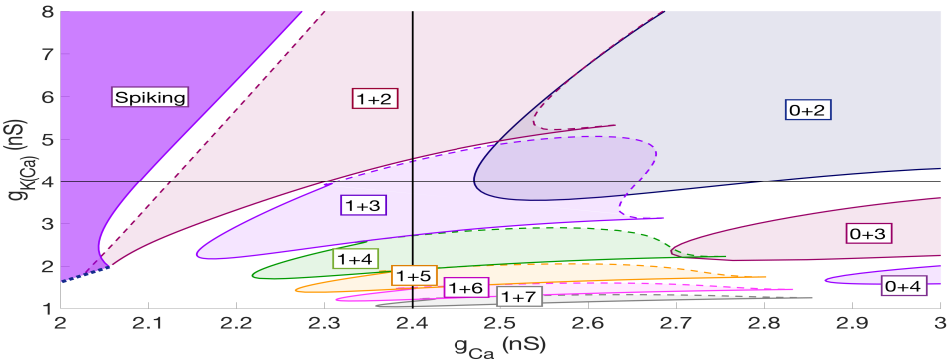

(b) $g_{K_{Ca}}$=4

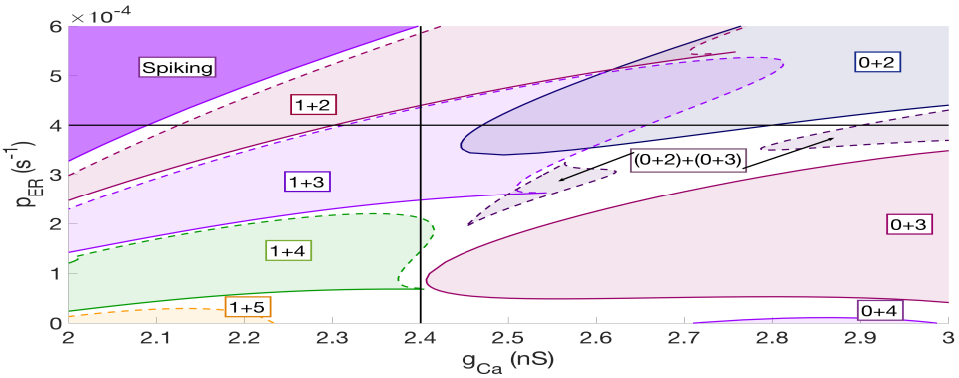

(c) g_{Ca}=2.4

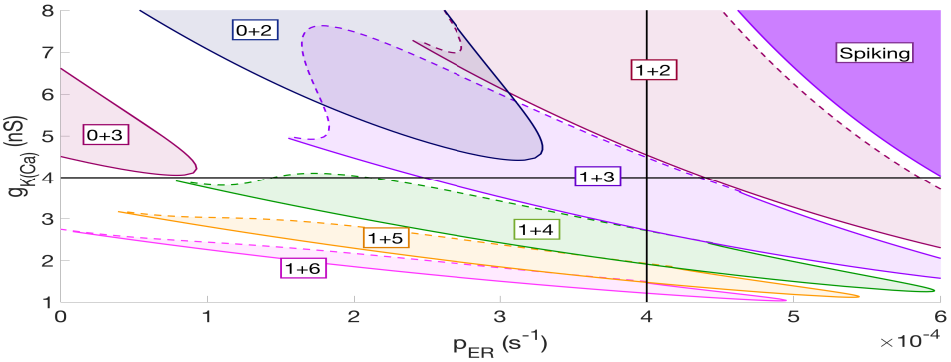

FIGURE 3.7. Two-parameter bifurcation diagrams of the reduced IHC model when p_{ER}=0.0004 (a), $g_{K_{Ca}}$=4 (b) and g_{Ca}=2.4 (c). Stable regions of solutions are delimited by tracing the period-doubling bifurcations (solid curves) and saddle-node bifurcation of periodic solutions (dashed curves) and are coloured accordingly. Torus bifurcations of the branches originating from Hopf bifurcations are indicated by dashed dotted curves. Black lines indicate the cross-sections.

diagrams of the reduced IHC model, which are g_{Ca}=2.4, $g_{K_{Ca}}$=4 and p_{ER}=0.0004. This set was chosen for the original IHC model in Chapter 2. The two parameter bifurcation diagram in Figure 3.7(a) when p_{ER}=0.0004 was computed by tracing the period-doubling bifurcations (solid curves) and saddle-node bifurcation of periodic solutions (dashed curves) in the g_{Ca}-$g_{K_{Ca}}$ plane. This diagram shows that the reduced IHC model generates oscillations similar to the original IHC model. For instance, we showed that the original IHC model generated oscillations upto 8 spikes (*0+8*, *1+7* and *2+6* solutions) when p_{ER}=0.0004 (see Figure 2.8(a) in Chapter 2). In agreement with this, we show in Figure 3.7(a) that the reduced IHC model also generates periodic solutions upto 8 spikes in total (*1+7* solution) when p_{ER}=0.0004.

On the other hand, although the original IHC model exhibits complex solutions with 2 large spikes (*2+4*, *2+5* etc.) in the g_{Ca}-$g_{K_{Ca}}$ plane shown in Figure 2.8(a) in Chapter 2, the reduced IHC model does not generate complex solutions with 2 large spikes when p_{ER}=0.0004. However, the reduced IHC model can produce complex periodic solutions with two or more large spikes with some other sets of parameters, which are not shown here.

The reduced IHC model can also generate the combination of bursting solutions. For example in Figure 3.7(b), we display the regions "*(0+2)+(0+3)*" by arrows that indicate the parameter regions of the stable periodic orbits, a burst with 2 small spikes is followed by another burst with 3 small spikes referring to *(0+2)+(0+3)* solution. In some parameter regions, the reduced IHC model generates periodic solutions which are a combination of complex solutions such as *(1+N)+(1+M)* etc. For example, we show time series and phase space projection of the *(1+3)+(1+4)* solution in Figure 3.8. Such periodic patterns can also be seen in the original IHC model.

As a result of the two-parameter bifurcation diagrams in Figure 3.7, we conclude that the reduced IHC model can generate oscillatory behaviours consistent with the behaviour observed in the original IHC model. We also interpret the relative

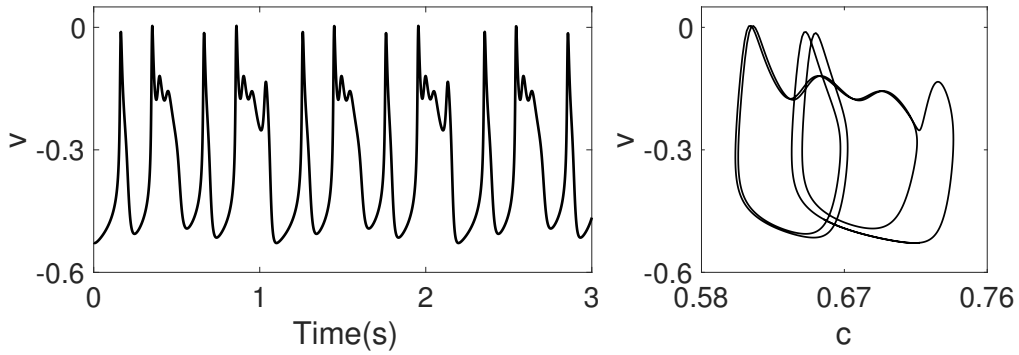

FIGURE 3.8. Time series and phase space projection of a combination of complex solution for the parameters g_{Ca}=2.6, $g_{\mathrm{K_{Ca}}}$=3 and p_{ER}=0.0004.

contributions of the three parameters on the model solutions in the reduced IHC model. Therefore, we can use the reduced (3D) IHC model for the slow-fast analysis in the following chapter instead of considering the original (4D) IHC model to split the variables into slow and fast sub-groups.

3.2.3 Aperiodic Model Solutions

Similar to the two-parameter bifurcation diagrams of the original (4D) IHC model, in Figure 3.7, we showed the stable regions for the periodic orbits in different colours according to the numbers of spikes of the periodic solutions of the reduced (3D) IHC model. These regions are determined by continuing the SNp and PD bifurcations in two parameters.

We consider the same parameter set as in Chapter 2 (g_{Ca}=2.18, $g_{\mathrm{K_{Ca}}}$=1.98 and p_{ER}=0.0004) to show the aperiodic motion of the reduced IHC model. We indicate this set by a blue cross in the two parameter bifurcation diagram on (g_{Ca}-$g_{\mathrm{K(Ca)}}$)-plane when p_{ER}=0.0004 in Figure 3.9. We show the time series and phase-space plots of the pattern and three Poincaré sections at V_{m}=-15 mV, V_{m}=-30 mV and V_{m}=-45 mV, respectively. As in the 4D model, these sections gives us a strong indication about the chaotic dynamic of the model trajectory. Moreover, the Poincaré sections in Figure 3.9

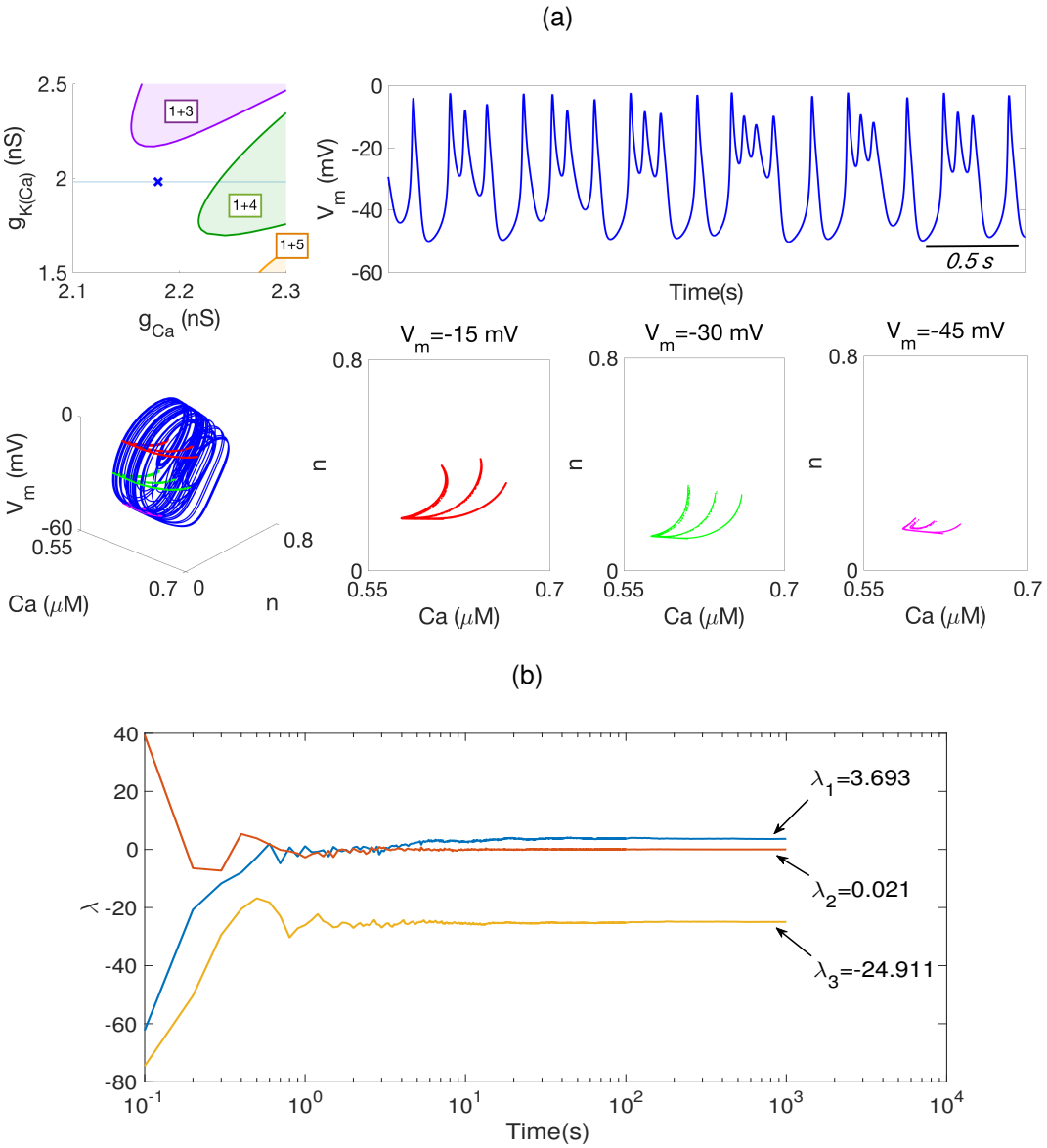

FIGURE 3.9. (a) An example of an aperiodic pattern in the reduced IHC model. The blue cross in the white region corresponds to parameters g_{Ca}=2.18 and $g_{K_{Ca}}$=1.98 in the two-parameter when p_{ER}=0.0004. Three Poincaré sections are considered at V_m=-15 mV, V_m=-30 mV and V_m=-45 mV. (b) The spectrum of the dynamic Lyapunov exponents.

indicate the strong dissipation and the resulting contraction of areas in phase space [2, 82] (see the Poincaré map in Figure 4.5(d) in [64] that indicates the presence of a rapid contraction of volumes).

We have shown the aperiodic pattern of the reduced IHC model at the same parameter set as the original IHC model. The Poincaré sections and Lyapunov exponents reveal that the reduced model also exhibits chaotic behaviour. We consider a set of parameters corresponding to the white region at the two-parameter bifurcation diagram in Figure 3.9 that is near the PD curves of *1+3* and *1+4* solutions. However, there are still unanswered questions about the chaotic motion of the IHC model such as 'Does this behaviour originate in a PD cascade or via some other route to chaos?', which will be left to further research.

3.3 Conclusion

In this chapter, we reduced the dimension of the original (4D) IHC model by approximating the slowest variable h with a constant. A similar analysis constructed for the original IHC model in Chapter 2 was undertaken for the reduced (3D) IHC model to show that the reduced model generates qualitatively similar behaviour as the original model.

We demonstrated that we do not lose the essential dynamic features of the original IHC model by fixing the slowest variable h in the original (4D) IHC model. Therefore, we could deal with a simpler three-dimensional model without losing the dynamic properties of the original (4D) IHC model. With this reduced model, we no longer have to use the phase projections of the original IHC model.

The same set of parameters were considered in the bifurcation analyses of the original (4D) and reduced (3D) IHC models. We compared the solutions of the original and reduced models as the parameter g_{Ca} varied. Due to the approximation of the slowest variable h, the original and reduced IHC models do not neccessary generate periodic solutions of same type (or the same number of oscillations) for the same parameter sets. However, there are some sets where both models generate the same type of periodic orbits as well as aperiodic solutions. Similar to the analysis done in Chapter 2 for the

original (4D) IHC model, we present a characterisation of the relative contributions of the three parameters of the reduced IHC model solutions. The two-parameter bifurcation diagrams reveal the qualitative agreement of the reduced model with the original model.

Additionally, the nondimensional reduced model introduced in this chapter will be considered in order to apply a slow-fast analysis to understand the mechanisms underlying the dynamics of the model solutions in Chapter 4 and our numerical bifurcation analysis here helps us to estimate the parameter regions of the reduced IHC model solutions according to the changes of the three parameters.

As we discussed in Chapter 2, there are some limitations to our analysis and further questions, which remain open in the analysis of the reduced IHC model. These are

- Although the two-parameter sections of the three dimensional parameter space gives an indication of the organisation of the periodic solutions having a different number of spikes, we still have not shown a complete view of solutions in three-dimensional parameteric space to display how these solutions connect and disconnect when they have different numbers of large and small spikes.
- The relation between the branches originating from Hopf bifurcations and isolas remains unclear.
- We have shown the Poincaré sections of an aperiodic trajectory in Figure 3.9, which correspond to the region in white in the two-parameter bifurcation diagram, where we could not find stable solutions. However, we could not identify the relation between the periodic, quasi-periodic and complex solutions in the IHC model in order to understand if a period-doubling cascade, quasi-periodic motion or other mechanisms underlie the observed chaotic pattern, which suggests a future direction of investigation of the chaotic attractors of the IHC model.

CHAPTER 4

A SLOW-FAST ANALYSIS OF THE REDUCED IHC MODEL

We simplified the original (4D) IHC model in Chapter 3 [90] by reducing its dimensions. This simplified version, called the *reduced IHC model*, is three-dimensional. Therefore, we are able to visualise and study the oscillatory behaviour in the full phase space of the model, rather than considering phase space projections. The nondimensional model equations reveal the typical time scale constants of the model variables as well as the model parameters that affect these time scales. Therefore, due to the differences between time scales of the model, we can split the reduced IHC model into the slow and the fast subsystems to gain an insight into the dynamics of the model solutions via a slow-fast analysis [78], which was reviewed in Chapter 1.

In this chapter we will apply a slow-fast analysis to the reduced IHC model. We will try to understand the contributions of the model parameters to the characteristic time scales of the model. Knowing the typical time scale constants of the model by nondimensionalisation, we are able to calculate the speed of the variables depending upon the parameters and categorise the variables as slow and fast. Then, we apply the slow-fast analysis techniques depending on the number of slow or fast variables (*1-slow/2-fast* or *2-slow/1-fast*) of the reduced (3D) IHC model.

4.1 The Subsystems of the Model

The slow-fast analysis was originally introduced by Rinzel [78] to understand the bursting solutions of the Chay-Keizer model [13]. We gave a brief overview of the slow-fast analysis in Chapter 1. In this chapter, we will apply this theory to the reduced IHC model to attempt to explain the dynamics of the bursting, complex solutions and mixed mode oscillations (MMOs) of the IHC model discussed in Chapters 2 and 3.

4.1.1 Dimensionless Model Equations

The dimensionless form of the reduced (3D) IHC model discussed in Chapter 3 is given by

$$\begin{aligned}
\frac{C_{\mathrm{m}}}{Q_{\mathrm{t}} g_{\max}} \frac{\mathrm{d}v}{\mathrm{d}\tau} &= -\hat{I}_{\mathrm{Ca}}(v,c) - \hat{I}_{\mathrm{K}}(v,n) - \hat{I}_{\mathrm{K_{Ca}}}(v,c) - \hat{I}_{\mathrm{leak}}(v) \\
\frac{1}{\hat{T}_n Q_{\mathrm{t}}} \frac{\mathrm{d}n}{\mathrm{d}\tau} &= \frac{1}{\hat{\tau}_{\mathrm{n}}(v)} (n_\infty(v) - n) \\
\frac{Q_{\mathrm{c}}}{Q_{\mathrm{t}} f_{\mathrm{c}} \alpha g_{\mathrm{Ca}} Q_{\mathrm{v}}} \frac{\mathrm{d}c}{\mathrm{d}\tau} &= -\bar{I}_{\mathrm{c}}(v,c) - \zeta_1 \bar{\phi}(c) c - \zeta_2 c + \zeta_3
\end{aligned} \tag{4.1}$$

The typical time scales of the state variables of the IHC model are given by the constants on the left hand side of the nondimensional form of the model in (4.1), which are

$$\hat{\tau}_v := \frac{C_{\mathrm{m}}}{Q_{\mathrm{t}} g_{\max}} \quad , \quad \hat{\tau}_n := \frac{1}{\hat{T}_n Q_{\mathrm{t}}} \quad \text{and} \quad \hat{\tau}_c := \frac{Q_{\mathrm{c}}}{Q_{\mathrm{t}} f_{\mathrm{c}} \alpha g_{\mathrm{Ca}} Q_{\mathrm{v}}} \tag{4.2}$$

We note that the parameter g_{Ca} affects both time scales of v and c when $g_{\mathrm{Ca}} \geq g_{\mathrm{K}} = 2.85$ i.e. the maxiumum conductance of the IHC model. Additionally, as we discussed in Chapter 3, the IHC model exhibits oscillatory behaviour when $0 < g_{\mathrm{Ca}} < 60$. Thus, considering the parameter values given in Table 1.1 in Chapter 1 and the range $0 < g_{\mathrm{Ca}} < 60$, we get

- the typical time constant of v is of an order between $O(10^{-3})$ and $O(10^{-4})$,

- the typical time constant of n is of an order $O(10^{-2})$
- the typical time constant of c is of an order between $O(10^{-1})$ and $O(10^{-2})$.

This suggests that when g_{Ca} is large, the variables n and c are slower ($O(10^{-2})$) than v ($O(10^{-4})$). Thus, in this case, the model could have one fast and two slow variables.

On the other hand, we note that the parameter f_c directly affects the time scale of c only. Decreasing f_c makes the slow variable slower i.e. the time scale of c is of an order $O(10^{0})$. Therefore, v and n become much faster than c, where the model could have two fast and one slow variables. We will study the effects of this parameter on the solutions of the model in Sections 4.2.1 and 4.2.2.

The dimensionless model can be rescaled by replacing τ with $\tilde{\tau} = \frac{Q_{\mathrm{t}} g_{\mathrm{max}}}{C_{\mathrm{m}}}\tau$. Therefore, we obtain

$$\begin{aligned}
\frac{\mathrm{d}v}{\mathrm{d}\tilde{\tau}} &= -\hat{I}_{\mathrm{Ca}}(v,c) - \hat{I}_{\mathrm{K}}(v,n) - \hat{I}_{\mathrm{K_{Ca}}}(v,c) - \hat{I}_{\mathrm{leak}}(v) \\
\frac{\mathrm{d}n}{\mathrm{d}\tilde{\tau}} &= \frac{\hat{T}_n C_{\mathrm{m}}}{g_{\mathrm{max}}}\left(\frac{n_\infty(v) - n}{\hat{\tau}_{\mathrm{n}}(v)}\right) \\
\frac{\mathrm{d}c}{\mathrm{d}\tilde{\tau}} &= \epsilon\left(-\bar{I}_{\mathrm{c}}(v,c) - \zeta_1 \bar{\phi}(c)c - \zeta_2 c + \zeta_3\right)
\end{aligned} \tag{4.3}$$

where

$$\epsilon = \frac{C_{\mathrm{m}} f_{\mathrm{c}} \alpha g_{\mathrm{Ca}} Q_{\mathrm{v}}}{g_{\mathrm{max}} Q_{\mathrm{c}}}. \tag{4.4}$$

$\epsilon = 0.000162$ when the bifurcation parameter values are given by g_{Ca}=2.4, $g_{\mathrm{K_{Ca}}}$=18, p_{ER}=0.00097 and $f_c = 0.000235$ whose time series graph is shown in Figure 4.1(a). The constant ϵ represents the ratio between fast and slow time scales. As we mentioned above, when f_c is small or g_{Ca} is large, the model could have two fast and one slow variables, where ϵ is of an order between $O(10^{-2})$ and $O(10^{-4})$ i.e. $\epsilon \ll 1$. Therefore, we can apply the *geometric singular perturbation analysis (GSPA)* with one slow variable (or *1-slow/2-fast analysis*) [78].

On the other hand, if we re-cast the system (4.3) from the fast time scale $\tilde{\tau}$ to the slow time scale $\tilde{t} := \epsilon\tilde{\tau}$, we obtain

$$\begin{aligned}
\epsilon\frac{\mathrm{d}v}{\mathrm{d}\tilde{t}} &= -\hat{I}_{\mathrm{Ca}}(v,c) - \hat{I}_{\mathrm{K}}(v,n) - \hat{I}_{\mathrm{K_{Ca}}}(v,c) - \hat{I}_{\mathrm{leak}}(v) \\
\frac{\mathrm{d}n}{\mathrm{d}\tilde{t}} &= \frac{\hat{T}_n Q_{\mathrm{c}}}{f_{\mathrm{c}}\alpha g_{\mathrm{Ca}} Q_{\mathrm{v}}}\left(\frac{n_\infty(v)-n}{\hat{\tau}_{\mathrm{n}}(v)}\right) \\
\frac{\mathrm{d}c}{\mathrm{d}\tilde{t}} &= -\bar{I}_{\mathrm{c}}(v,c) - \zeta_1\bar{\phi}(c)c - \zeta_2 c + \zeta_3
\end{aligned} \tag{4.5}$$

to which we apply *2-slow/1-fast analysis* [7]. Next, we will discuss the slow-fast analysis by splitting the IHC model equations into slow and fast subsystems in greater detail.

4.1.2 Fast and Slow Subsystems

If a dynamical system exhibits only two time scales, it is commonly called a *slow-fast system* [52]. We have shown that the reduced (3D) IHC model has slow and fast variables depending upon the model parameters. If the slow variable is very slow (when ϵ is sufficiently small in (4.3)), then we can study the behaviour of the reduced IHC model using the subsystem obtained from the singular limit ($\epsilon \to 0$). This allows us to treat the slow variable as a bifurcation parameter in the model with the assumption $\frac{\mathrm{d}c}{\mathrm{d}\tilde{\tau}} = 0$ and to analyse the bifurcation structure of the fast subsystem in order to make predictions for $0 < \epsilon \ll 1$ [7, 52, 78, 79].

Considering the system (4.3) in the limit $\epsilon \to 0$ where v and n are the fast variables and c is the slow variable (1-slow/2-fast), we have

$$\begin{aligned}
\frac{\mathrm{d}v}{\mathrm{d}\tilde{\tau}} &= -\hat{I}_{\mathrm{Ca}}(v,c) - \hat{I}_{\mathrm{K}}(v,n) - \hat{I}_{\mathrm{K_{Ca}}}(v,c) - \hat{I}_{\mathrm{leak}}(v) \\
\frac{\mathrm{d}n}{\mathrm{d}\tilde{\tau}} &= \frac{\hat{T}_n C_{\mathrm{m}}}{g_{\mathrm{max}}}\left(\frac{n_\infty(v)-n}{\hat{\tau}_{\mathrm{n}}(v)}\right) \\
\frac{\mathrm{d}c}{\mathrm{d}\tilde{\tau}} &= 0
\end{aligned} \tag{4.6}$$

Hence, system (4.6) represents the *fast subsystem* (or *layer equations*) of the reduced IHC model [16, 52]. Since $\frac{\mathrm{d}c}{\mathrm{d}\tilde{\tau}} = 0$, we can consider c as a parameter in (4.6) and study the asymptotic behaviour of the the fast subsystem by computing the bifurcation

diagram of the fast subsystem where c is a bifurcation parameter. Then, using the information extracted from the fast subsystem bifurcation structure, we attempt to interpret the behaviour of the solutions of the reduced IHC model.

The slow subsystem that corresponds to the fast subsystem in (4.6) is given by

$$\begin{aligned} 0 &= -\hat{I}_{\mathrm{Ca}}(v,c) - \hat{I}_{\mathrm{K}}(v,n) - \hat{I}_{\mathrm{K_{Ca}}}(v,c) - \hat{I}_{\mathrm{leak}}(v) \\ 0 &= \frac{\hat{T}_n C_{\mathrm{m}}}{g_{\max}} \left(\frac{n_\infty(v) - n}{\hat{\tau}_{\mathrm{n}}(v)} \right) \\ \frac{\mathrm{d}c}{\mathrm{d}\tilde{t}} &= \left(-\bar{I}_{\mathrm{c}}(v,c) - \zeta_1 \bar{\phi}(c) c - \zeta_2 c + \zeta_3 \right) \end{aligned} \tag{4.7}$$

We observed from the typical time scale constants in (4.2) that the reduced IHC model could have one fast and two slow variables depending on the choice of parameters. Considering v is the fast variable and n and c are the slow variables (2-slow/1-fast), we write the system (4.5) in the singular limit as $\epsilon \to 0$

$$\begin{aligned} 0 &= -\hat{I}_{\mathrm{Ca}}(v,c) - \hat{I}_{\mathrm{K}}(v,n) - \hat{I}_{\mathrm{K_{Ca}}}(v,c) - \hat{I}_{\mathrm{leak}}(v) \\ \frac{\mathrm{d}n}{\mathrm{d}\tilde{t}} &= \frac{\hat{T}_n Q_{\mathrm{c}}}{f_{\mathrm{c}} \alpha g_{\mathrm{Ca}} Q_{\mathrm{v}}} \left(\frac{n_\infty(v) - n}{\hat{\tau}_{\mathrm{n}}(v)} \right) \\ \frac{\mathrm{d}c}{\mathrm{d}\tilde{t}} &= -\bar{I}_{\mathrm{c}}(v,c) - \zeta_1 \bar{\phi}(c) c - \zeta_2 c + \zeta_3 \end{aligned} \tag{4.8}$$

which is called the *slow subsystem* (or *reduced subsystem*) of the model [16, 52]. We prefer to use the term "slow subsystem" instead of "reduced subsystem" in order to avoid confusion with the reduced IHC model.

The fast subsystem that corresponds to the slow subsystem in (4.8) is given by

$$\begin{aligned} \frac{\mathrm{d}v}{\mathrm{d}\tilde{\tau}} &= -\hat{I}_{\mathrm{Ca}}(v,c) - \hat{I}_{\mathrm{K}}(v,n) - \hat{I}_{\mathrm{K_{Ca}}}(v,c) - \hat{I}_{\mathrm{leak}}(v) \\ \frac{\mathrm{d}n}{\mathrm{d}\tilde{\tau}} &= 0 \\ \frac{\mathrm{d}c}{\mathrm{d}\tilde{\tau}} &= 0 \end{aligned} \tag{4.9}$$

The system (4.8) contains an algebraic equation

$$F(v,n,c)=0 \quad \text{where} \quad F(v,n,c)=-\hat{I}_{\mathrm{Ca}}(v,c)-\hat{I}_{\mathrm{K}}(v,n)-\hat{I}_{\mathrm{K_{Ca}}}(v,c)-\hat{I}_{\mathrm{leak}}(v) \tag{4.10}$$

in addition to the ODEs for the variables n and c in (4.8). Therefore, the system in (4.8) is called *a differential-algebraic system*. The differential-algebraic system describes the *slow flow* that is restricted to the critical manifold [7, 16, 52]

$$S:=\{(v,n,c)\in\mathbb{R}^3 \quad | \quad F(v,n,c)=0\}. \tag{4.11}$$

We will use the fast and slow subsystems in order to understand the dynamics of the full model given by (4.5) from a geometrical point of view taking into account the invariant manifolds of the fast and slow subsystems, respectively.

4.1.3 The Critical Manifold and Slow Flow

The critical manifold, which is given by the set $S:=\{(v,n,c)\in\mathbb{R}^3 \quad | \quad F(v,n,c)=0\}$ where $F(v,n,c):=-\hat{I}_{\mathrm{Ca}}(v,c)-\hat{I}_{\mathrm{K}}(v,n)-\hat{I}_{\mathrm{K_{Ca}}}(v,c)-\hat{I}_{\mathrm{leak}}(v)$, represents a surface in $\mathbb{R}^3$, which is the equilibrium set of the fast subsystem for the 2-slow/1-fast case [7, 16, 52].

The fold curves on the critical manifold are defined by

$$F^{l,u}:=\{(v,n,c)\in\mathbb{R}^3 \quad | \quad F(v,n,c)=0 \quad \text{and} \quad \frac{\partial F}{\partial v}=0\}. \tag{4.12}$$

In the equation $F(v,n,c)=0$, the variable n appears only in the voltage-dependent K^+ current that is given by $\hat{I}_{\mathrm{K}}(v,n)=\frac{g_{\mathrm{K}}}{g_{\max}}nh(v-v_{\mathrm{K}})$. Therefore, $F(v,n,c)$ is linear in n, and so we can solve $F(v,n,c)=0$ for n in terms of v and c. Hence, we get

$$n:=n(v,c)=\frac{-g_{\mathrm{Ca}}m_{\infty}^2(v)q_{\infty}(c)(v-v_{\mathrm{Ca}})-g_{\mathrm{K_{Ca}}}s_{\infty}(c)(v-v_{\mathrm{K}})-g_{\mathrm{leak}}(v-v_{\mathrm{leak}})}{g_{\mathrm{K}}h(v-v_{\mathrm{K}})}$$

The slow subsystem, which is given by a differential-algebraic system (4.8), describes the flow when the trajectory is on the critical manifold [16].

Taking the derivative of $F(v,n,c)=0$ with respect to time $\tilde{t}$ and applying the chain rule to $\frac{dF}{d\tilde{t}}=0$, we obtain

$$\begin{aligned}
-\frac{\partial F}{\partial v}\frac{dv}{d\tilde{t}} &= \frac{\partial F}{\partial n}\frac{dn}{d\tilde{t}}+\frac{\partial F}{\partial c}\frac{dc}{d\tilde{t}} \\
-\frac{\partial F}{\partial v}\frac{dv}{d\tilde{t}} &= \left(\frac{\hat{T}_n Q_{\mathsf{c}}}{f_{\mathsf{c}}\alpha g_{\mathsf{Ca}} Q_{\mathsf{v}}}\left(\frac{n_\infty(v)-n}{\hat{\tau}_{\mathsf{n}}(v)}\right)\right)\frac{\partial F}{\partial n}+\left(-\bar{I}_{\mathsf{c}}(v,c)-\zeta_1\bar{\phi}(c)c-\zeta_2 c+\zeta_3\right)\frac{\partial F}{\partial c}
\end{aligned} \tag{4.13}$$

This system is singular when $\frac{\partial F}{\partial v}=0$ i.e. at the fold curves. The flow is well defined on the critical manifold S, but not on the fold curves. In order to remove the singularities, we introduce a re-scaled time $\hat{t}:=-\left(\frac{\partial F}{\partial v}\right)^{-1}d\tilde{t}$. Hence, we obtain the system

$$\begin{aligned}
\frac{dv}{d\hat{t}} &= G(v,c) \\
\frac{dc}{d\hat{t}} &= -\left(-\bar{I}_{\mathsf{c}}(v,c)-\zeta_1\bar{\phi}(c)c-\zeta_2 c+\zeta_3\right)\frac{\partial F}{\partial v}
\end{aligned} \tag{4.14}$$

where $G(v,c)=\left(\frac{\hat{T}_n Q_{\mathsf{c}}}{f_{\mathsf{c}}\alpha g_{\mathsf{Ca}} Q_{\mathsf{v}}}\left(\frac{n_\infty(v)-n}{\hat{\tau}_{\mathsf{n}}(v)}\right)\right)\frac{\partial F}{\partial n}+\left(-\bar{I}_{\mathsf{c}}(v,c)-\zeta_1\bar{\phi}(c)c-\zeta_2 c+\zeta_3\right)\frac{\partial F}{\partial c}$. This system defines the *desingularised slow flow* [16, 52].

A trajectory of the reduced IHC model near the singular limit passes through a folded singularity with finite speed unlike the other points on the fold curve, where trajectories have infinite speed [7].

The main idea of the geometric singular perturbation theory (GSPT) (or the slow-fast analysis) reviewed above is to gain insight into the reduced (3D) IHC model introduced in (4.1) by breaking it into subsystems using the information extracted from the subsystems, the layer equations and the slow subsystem, with $0<\epsilon\ll 1$. GSPT analyses a dynamical system from a geometrical point of view by taking advantage of the Fenichel Theory [23]. Fenichel Theory states that if $\epsilon>0$ is sufficiently small and S is normally hyperbolic, then invariant manifolds exist that are at $O(\epsilon)$ distance from S, and as $\epsilon\to 0$ the flows on these invariant manifolds converge to the slow flow on S.

Our goal is to understand the oscillatory behaviour of the reduced IHC model based on its fast and slow dynamics. We investigate the behaviour of fast and slow variables

for different parameter sets and apply a slow-fast analysis to interpret the solutions of the full model in terms of their behaviour near the invariant manifolds of fast and slow subsystems.

4.2 The Slow-Fast Decomposition of the Reduced IHC Model

We calculated the typical time scale constants of the reduced IHC model in the previous section. These time scale constants suggest that the variable c in the reduced IHC model could either be the only slow variable or share a similar time scale with the variable n depending on the choice of parameters. In order to gain insight into the dynamics of the reduced (3D) IHC model, we split the model equations into fast and slow subsystems. Using the bifurcation structure of the subsystems, we will investigate the 1-slow/2-fast and 2-slow/1-fast cases of the reduced IHC model that depend upon different sets of parameters. We also discuss the dynamics of the model when there is not a clear separation between the time scales. In this case we cannot reasonably apply the slow-fast analysis.

4.2.1 One Slow-Two Fast Analysis

We showed that the model could have two distinct time scales (a slow-fast system) in Section 4.1.2. As indicated in (4.2) the parameter f_c, the fraction of free to total cytosolic calcium, makes a direct contribution to the time scale of the slow variable c without affecting the time scales of the variables v and n.

In order to make the ratio between the fast and the slow time scales ϵ smaller, we make the slow variable c slower by increasing its time scale constant $\hat{\tau}_c = \frac{Q_c}{Q_t f_c \alpha g_{Ca} Q_v}$. The slow time scale $\hat{\tau}_c$ is inversely proportional to the parameter f_c, and f_c does not appear in the fast time scale equations in (4.2). As f_c decreases, $\hat{\tau}_c$ increases, which implies that the slow variable c becomes slower. This allows us to investigate the dynamics

of the various periodic solutions of the reduced IHC model by applying a slow-fast analysis.

Full model solutions

Before turning our attention to analysing the reduced IHC model in the limit of $\epsilon = 0$, it is instructive to look at the behaviour of the full model as f_c changes.

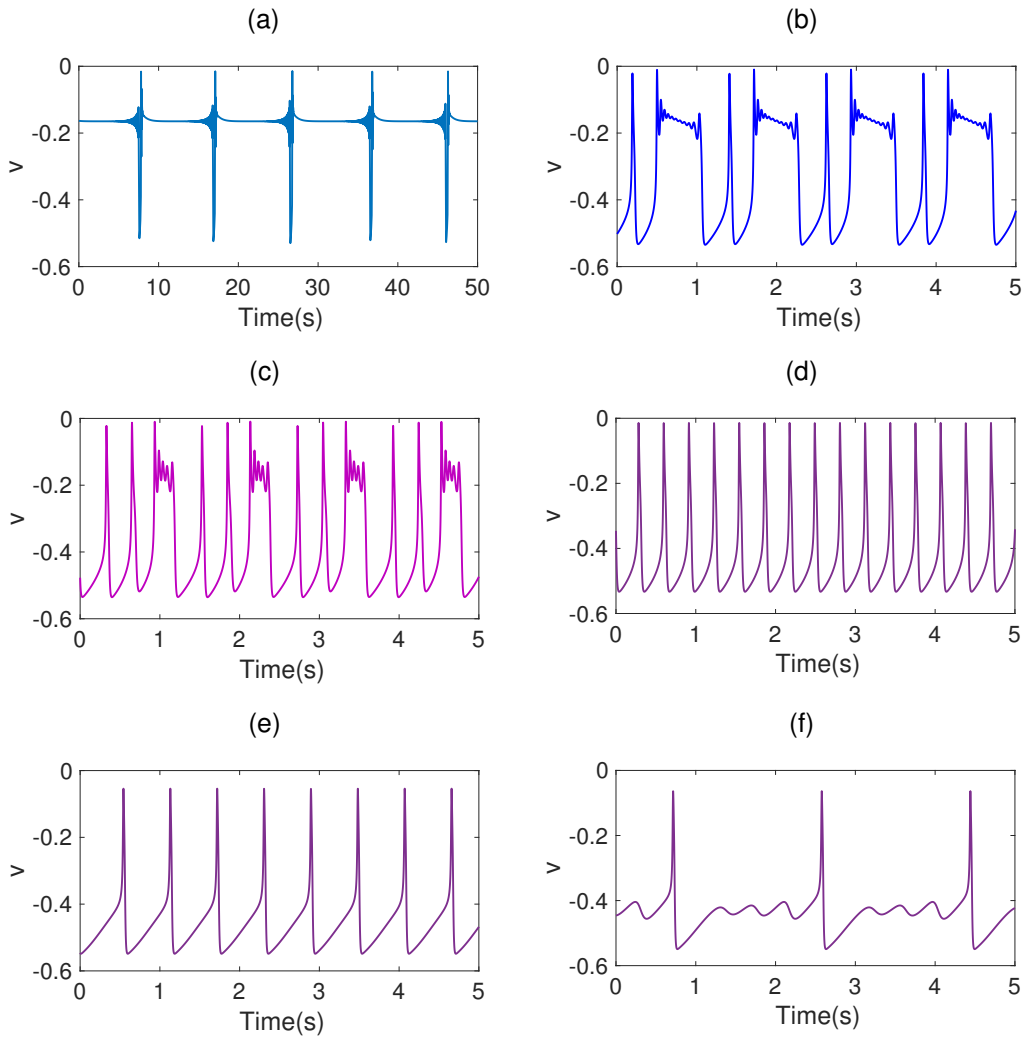

FIGURE 4.1. Time series of periodic orbits for (a) f_c= 0.000235, (b) f_c= 0.0004, (c) f_c= 0.0006, (d) f_c= 0.001, (e) f_c= 0.00235 and (f) f_c= 0.00244.

In Figure 4.1, we plot the time series solutions of some of the periodic orbits. As f_c

increases, the model produces complex solutions with one large spike and different numbers of small spikes (from *1+11* to *1+4* solutions). Furthermore, the model also produces complex periodic orbits having two large spikes followed by a burst, for example *2+5*, *2+4* and *2+3*. We plot the complex periodic orbit *2+5* as a representative time series for such model solutions, which is computed at f_c= 0.0006. For a large range of the bifurcation parameter f_c values, the model produces single spike solutions (for instance f_c= 0.001 and f_c= 0.00235 in Figure 4.1(d)-(e)). We note that for f_c= 0.00244 in Figure 4.1(f), the periodic orbit is a combination of large and small oscillations, but different from the complex periodic orbits in Figure 4.1(b)-(c). Next we apply a slow-fast analysis in an attempt to gain further insight into the behaviour of the periodic solutions described above.

Slow-fast analysis of the reduced IHC model

In Section 3.1.2, we estimated the time scale constants for the rate of change of the variables in (4.2). Considering the scaling parameters Q_{v}=100 mV, Q_{c}=1 μM, $Q_{\mathrm{t}} = 1$ s discussed in Section 4.1.1 and using the parameter values given in Table 1.1 in Chapter 1, the time constants of the reduced IHC model are $\hat{\tau}_v = 0.000394$, $\hat{\tau}_n = 0.0051$, $\hat{\tau}_c = 2.417$ and $\epsilon = 0.000162$ when the bifurcation parameter values are given by g_{Ca}=2.4, $g_{\mathrm{K_{Ca}}}$=18, p_{ER}=0.00097 and $f_c = 0.000235$. We see that the variables v and n evolve on time scales that are much faster than the variable c. Therefore, for the given parameter values, we can define that v and n are the fast variables and c is the slow variable in the model.

We consider the singular limit $\epsilon = 0$ in (4.6) to obtain the fast subsystem or layer equations of the reduced IHC model

$$\begin{aligned}
\frac{\mathrm{d}v}{\mathrm{d}\tilde{\tau}} &= -\hat{I}_{\mathrm{Ca}}(v,c) - \hat{I}_{\mathrm{K}}(v,n) - \hat{I}_{\mathrm{K_{Ca}}}(v,c) - \hat{I}_{\mathrm{leak}}(v) \\
\frac{\mathrm{d}n}{\mathrm{d}\tilde{\tau}} &= \frac{\hat{T}_n C_{\mathrm{m}}}{g_{\max}} \left(\frac{n_\infty(vQ_{\mathrm{v}}) - n}{\hat{\tau}_{\mathrm{n}}(v)} \right) \\
\frac{\mathrm{d}c}{\mathrm{d}\tilde{\tau}} &= 0
\end{aligned} \tag{4.15}$$

Since $\frac{dc}{d\tilde{\tau}} = 0$, we can treat c as a parameter in the fast subsystem. Then, using the fast subsystem bifurcation structure, we will attempt to interpret the dynamics of the periodic solutions of the reduced IHC model.

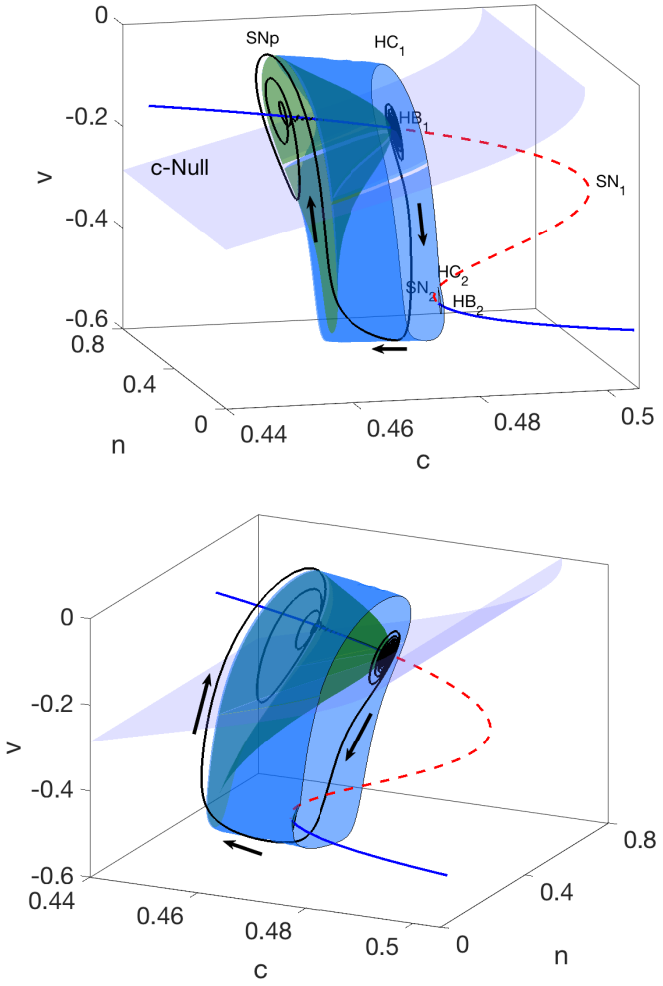

FIGURE 4.2. Three dimensional views of the fast subsystem in (4.15) when $f_c = 0.000235$. The bursting periodic orbit shown in Figure 4.1(a) is superimposed on the figure. The blue solid curves represent the stable equilibria and the red dashed curve represents unstable equilibria. The blue and green surfaces represent the stable and unstable periodic orbits, respectively. The transparent surface is the c-nullcline. HB: Hopf bifurcation, SN: Saddle-node bifurcation of equilibria, SNp: Saddle-node bifurcation of periodic orbits, HC: Homoclinic bifurcation.

In Figure 4.2, we plot two different views of the bifurcation diagram of the fast subsystem

using c as a bifurcation parameter of the reduced (3D) IHC model. As the bifurcation parameter c increases, the stable equilibria (solid blue curve) of the fast subsystem undergoes a sub-critical Hopf bifurcation (HB_1) and loses stability (dashed red curve). The branch of equilibria regains stability at another sub-critical Hopf bifurcation (HB_2) obtained for larger values of c. A branch of unstable limit cycles (green surface) emanates from (HB_1) and gains stability (blue surface) at a saddle-node bifurcation (SNp). This branch of stable limit cycles terminates at a homoclinic orbit (HC_1).

A periodic orbit computed for $f_c = 0.000235$ of the full (3D) IHC model, whose time series is shown in Figure 4.1(a), is superimposed on the fast subsystem bifurcation diagram in Figure 4.2. Above the c-nullcline, which is indicated by c-Null, c increases since $\frac{\mathrm{d}c}{\mathrm{d}\bar{\tau}} > 0$. Additionally, the amplitude of the small spikes within the bursting part of the periodic solution decreases until HB_1. This behaviour can be understood in terms of the type of the fast system equilibria, which are stable foci. As the trajectory of the full system moves away from HB_1 the amplitude of the small spikes within the burst starts to increase as the stability of the equilibria in the fast subsystem has changed and these are now unstable foci. However, since the c-nullcline is very close to the Hopf bifurcation HB_1, the slow passage through Hopf [5] occurs in a very narrow range of c. As the amplitude of the small spikes increases the trajectory of the full system crosses the c-nullcline, the direction of the flow is reversed and is attracted to the other stable regime of the fast subsystem, which is stable limit cycles. Crossing the c-nullcline, c starts decreasing ($\frac{\mathrm{d}c}{\mathrm{d}\bar{\tau}} < 0$) while the trajectory follows the stable limit cycles region (blue surface). When the trajectory crosses the saddle node bifurcation of periodic (SNp), it is attracted back to the stable equilibria region.

In Figure 4.3, we plot fast subsystem bifurcation diagrams for different values of f_c. As f_c increases, the reduced IHC model solutions do not follow the stable regions of the fast subsystem as closely as the bursting solution described above. Therefore, we can no longer apply 2-slow/1-fast analysis when f_c is large. Additionally, the typical time scale constants we estimated in Section 4.1.1 imply that, depending upon the

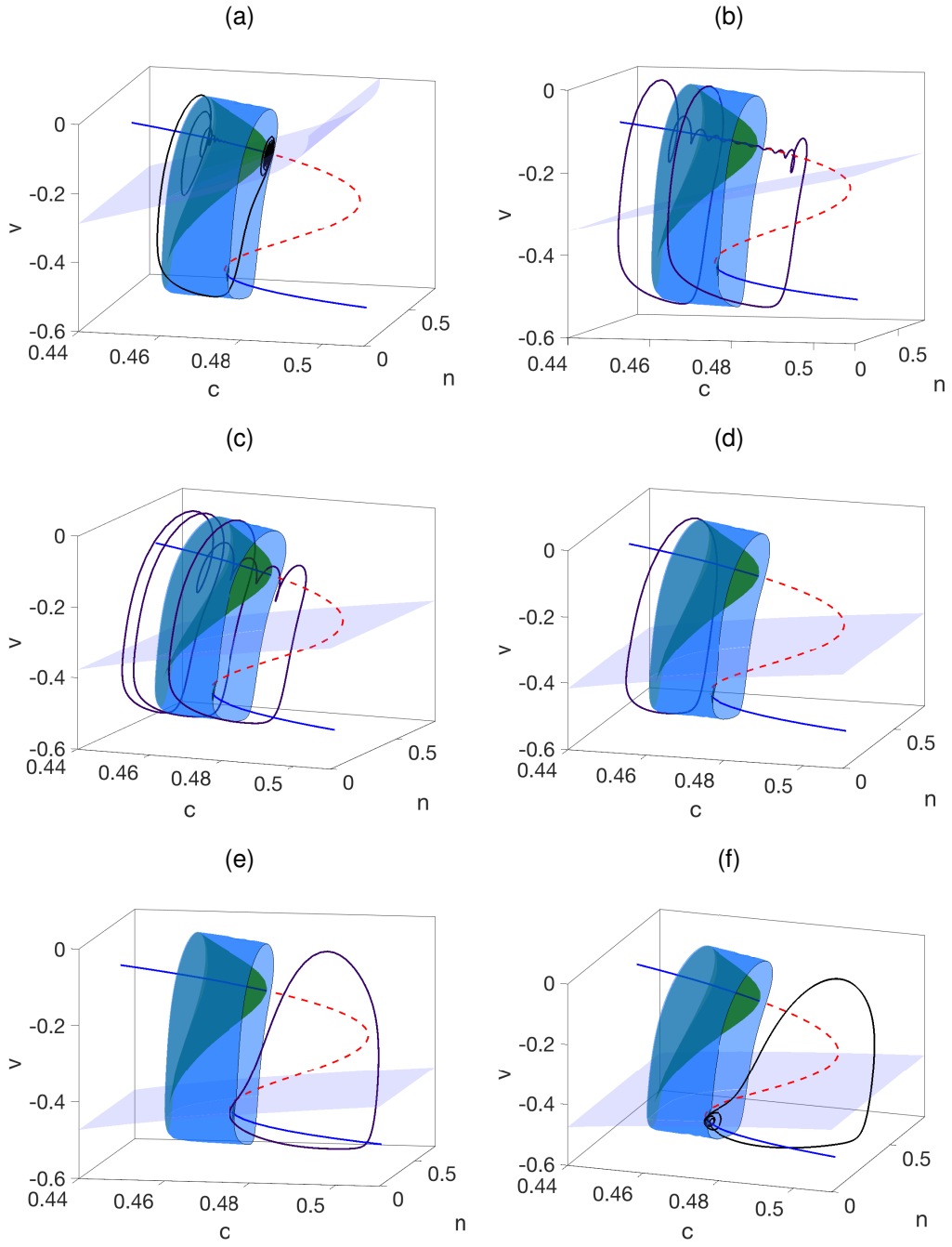

FIGURE 4.3. Bifurcation diagrams of the fast subsystem in (4.15) and superimposed periodic orbits when (a) f_c= 0.000235 (Bursting), (b) f_c= 0.0004 (Complex: *1+11*), (c) f_c= 0.0006 (Complex: *2+5*), (d) f_c= 0.001 (Single spike), (e) f_c= 0.00235 (Single spike) and (f) f_c= 0.00244.

parameter values, the model could also be seen as having one fast and two slow variables, which could be the case when f_c is increased. We investigate this in the next section.

4.2.2 Two Slow-One Fast Analysis

Above we showed that the 2-slow/1-fast analysis does not explain the full system behaviour sufficiently when we increase f_c in Figure 4.3. In terms of time scales, when f_c increases, the slow time scale $\hat{\tau}_c$ becomes smaller, therefore the slow variable c becomes faster. Thus, the model now has two slow variables (n and c) and one fast variable (v).

As we reviewed in Section 4.1.3, the S-shaped critical manifold is defined by the set

$$S := \{(v,n,c) \in \mathbb{R}^3 \quad | \quad F(v,n,c) = 0\}$$

where $F(v,n,c) := -\hat{I}_{\mathrm{Ca}}(v,c) - \hat{I}_{\mathrm{K}}(v,n) - \hat{I}_{\mathrm{K_{Ca}}}(v,c) - \hat{I}_{\mathrm{leak}}(v)$. The critical manifold in Figure 4.4 has two fold curves (lower F^l and upper F^u) that separate the repelling and attracting sheets of the manifold.

In Figure 4.4, we plot the critical manifold for f_c=0.00244. The trajectories of the desingularised slow flow, which was defined in (4.14), are shown on the figure as thin cyan curves and arrows are the direction of the slow flow. We magnified the regions of the lower F^l and upper F^u fold curves.

On the lower fold curve, there is a folded singularity, denoted by a green circle, where the trajectories of the slow flow switch from incoming to outgoing [16], satisfies

i) $F(v,n,c)\Big|_{p_*} = 0$,

ii) $\frac{\partial F(v,n,c)}{\partial v}\Big|_{p_*} = 0$, $\frac{\partial^2 F(v,n,c)}{\partial v^2}\Big|_{p_*} \neq 0$

iii) $D_{(n,c)}F(v,n,c)\Big|_{p_*}$ has full rank one, and

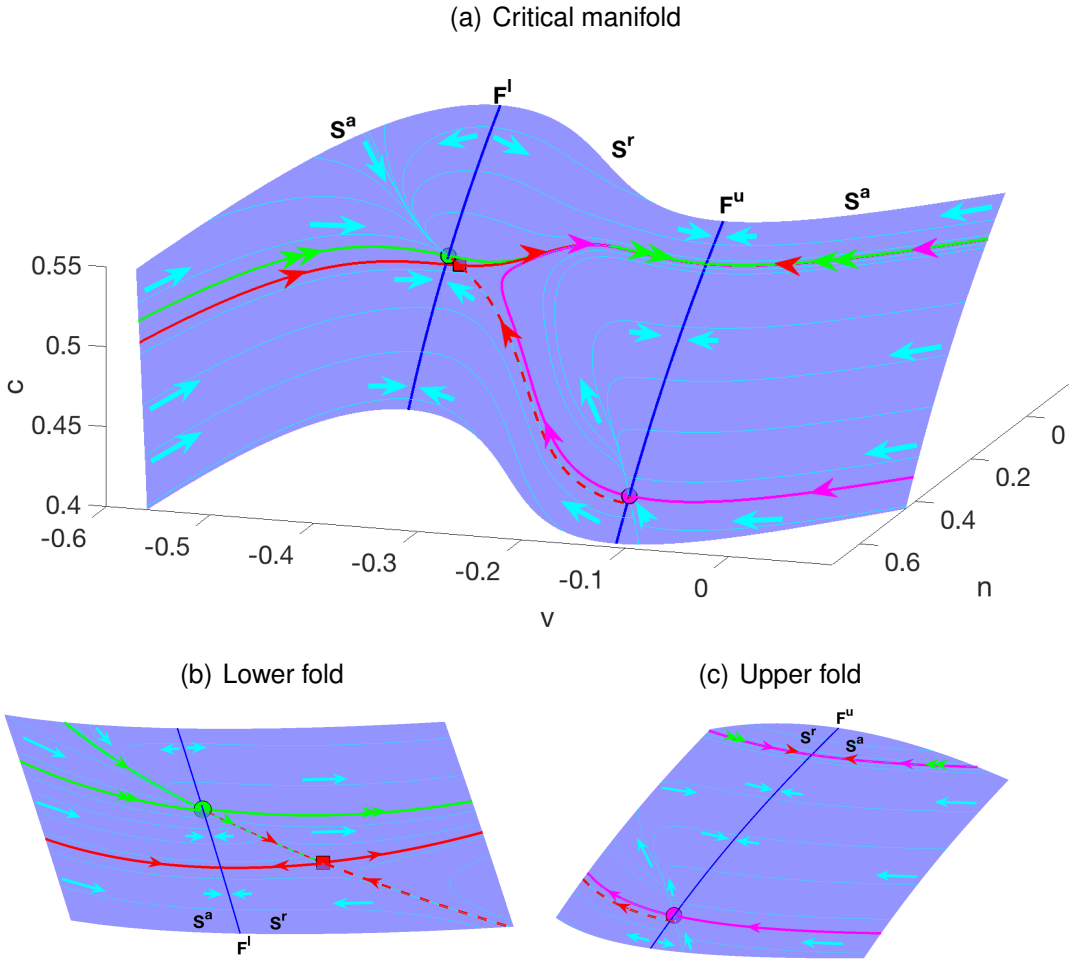

FIGURE 4.4. The critical manifold in (4.11) when f_c=0.00244. The thin cyan curves are the trajectories of the slow flow in (4.14). The green curves are strong (double arrows) and weak (single arrows) stable manifold of the node (green circle) on the lower fold curve (F^l). The red curves are the stable (solid) and unstable (dashed) manifolds of the saddle equilibrium on the repelling sheet (S^r) at the critical manifold. The magenta curve is the strong manifold of the node on the upper fold curve (F^u).

iv) $\left(\frac{\partial F(v,n,c)}{\partial n}\Big|_{p_*}\left(\frac{n_\infty(v)-n(v,c)}{\hat{\tau}_n(v)}\right)\Big|_{p_*}\right)+\left(\frac{\partial F(v,n,c)}{\partial n}\Big|_{p_*}\left(-\bar{I}_c(v,c)-\zeta_1\bar{\phi}(c)c-\zeta_2 c+\zeta_3\right)\Big|_{p_*}\right)=0$

where $p_* \in F^l$ on S. This implies p_* is *a folded singularity* [7, 16].

Additionally, the eigenvalues of the Jacobian matrix of the desingularised system

$$\begin{aligned} \frac{dv}{d\hat{t}} &= F(v,c) \\ \frac{dc}{d\hat{t}} &= -\left(-\bar{I}_{\mathrm{c}}(v,c) - \zeta_1 \bar{\phi}(c)c - \zeta_2 c + \zeta_3\right)\frac{\partial F}{\partial v} \end{aligned} \tag{4.16}$$

are σ_1=-0.51 and σ_1=-0.11 with the given model parameters. These real positive eigenvalues indicate that p_* is a folded node [16, 17].

The green curves are the strong (double arrows) and weak (single arrow) stable manifolds of the node p_*. We must note that the slow flow reverses on the repelling branch of the critical manifold due to the time rescaling $\hat{t} := -\left(\frac{\partial F}{\partial v}\right)^{-1} d\tilde{t}$ discussed in Section 4.1.3.

Moreover, there is another equilibrium point of the desingularised system in (4.16). This is a saddle equilibrium shown as a red square on the repelling part, which is also an equilibrium (saddle focus) of the full model. We plot the stable (solid red curve) and unstable (dashed red curve) manifolds of the saddle equilibrium of the desingularised system by reversing the direction of the slow flow on the repelling sheet of the critical manifold.

Similar to the lower fold, there is a folded node singularity on the upper fold curve, which is denoted by a magenta circle, whose strong stable manifold is shown by the magenta coloured curve on the manifold.

Next, we would like to interpret the behaviour of the full model periodic orbit at f_c=0.00244 in terms of the slow flow on the critical manifold shown in Figure 4.4. Therefore, we superimposed the periodic orbit (black coloured) on the critical manifold in Figure 4.5.

The S-shaped critical manifold is the blue surface in Figure 4.5. The manifold has two fold curves; at $v \approx -0.45$ (lower) and $v \approx -0.11$ (upper). The middle surface between fold curves is repelling S^r, and the top and bottom surfaces separated by the two fold

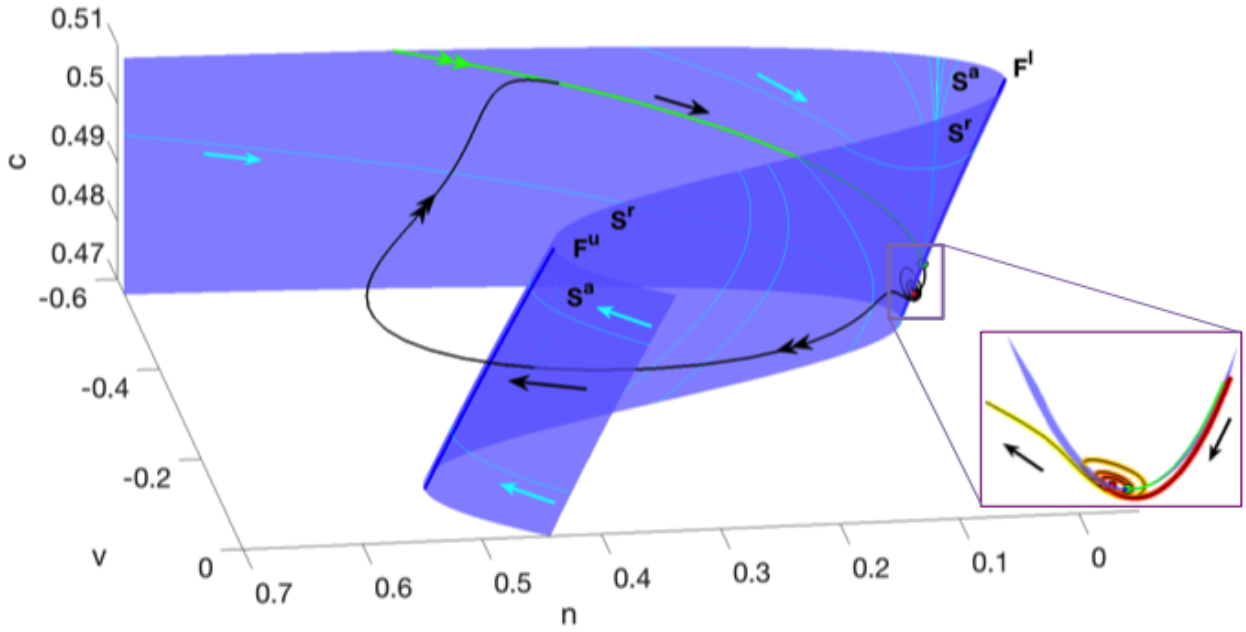

FIGURE 4.5. The periodic orbit when f_c=0.00244 is superimposed on the critical manifold in (4.11). The green curve is the strong manifold of the node on the lower fold curve (F^l). The region of small oscillations around the saddle-focus equilibrium of the full model is magnified. The colour code on the orbit around the small oscillations represents the time along the periodic orbit i.e. time increases from red to yellow.

curves of the manifold are attracting. The saddle-focus equilibrium [33], indicated by a red square in Figure 4.5, has a pair of unstable complex conjugate eigenvalues ($\lambda_{1,2} = 1.21 \pm i16.65$) and a real negative eigenvalue ($\lambda_3 = -6.56$).

The interplay of the periodic orbit shown in Figure 4.1(f) with the desingularised slow flow gives an insight into the overall structure of the periodic orbit superimposed in Figure 4.5.

On the lower attracting sheet of the critical manifold S^a, the periodic orbit follows the strong stable manifold (green curve) of the folded node singularity on F^l. We colour code time when presenting the periodic orbit around the lower fold F^l (see the magnified region in Figure 4.5). As time increases, which is indicated by the colour

change from red to yellow on the periodic orbit, the small oscillations become larger around the saddle-focus equilibrium [33] on the repelling sheet, which repeatedly intersect the repelling and attracting sheets of the manifold. Then, it jumps to the upper attracting part of the critical manifold, where the attraction is not as strong as on the lower sheet. After the trajectory passes the upper fold, it jumps to the lower attraction sheet of the critical manifold and returns to the region near the singularity. Hence, it makes a full limit cycle and continues the periodic motion.

4.2.3 Slow-Fast Analysis of Complex Periodic Solutions

We have shown that the reduced (3D) IHC model can have two fast (v and n) and one slow variables (c) when f_c=0.000235 (bursting). However, as f_c increases, the model now has one fast (v) and two slow variables (n and c) when f_c= 0.00244 (MMO). Morever, for the values between $0.000235 < f_c < 0.00244$ the model produces complex solutions as shown in Figures 4.1(b) and 4.1(c).

In fact the time scales for each of the variables in the IHC model vary along the limit cycle solutions. So far we have used estimates of constant time scales based on consideration of certain bounds. In the case of complex solutions however, it appears that the variation of time scales along periodic orbit trajectories might be significant. Hence taking time scale bounds and using classic slow-fast analysis is not sufficient to explain the behaviour of the model. We attempt to illustrate this by plotting the fast subsystem bifurcation diagram in Figure 4.6(a) considering v and n are fast and c is slow. Additionaly, we plot the critical manifold in Figure 4.6(d) considering v is the fast, and n and c are the slow variables.

The fast subsystem diagram in Figures 4.6(a) and 4.6(b) somewhat indicates that the bursting part of the complex solutions follows the upper equilibria. Since the upper stable equilibria curve (solid blue) is a stable focus, the amplitude of the oscillations around this curve become smaller until Hopf biurcation. Then, as a result of the unstable equilibria (focus) curve after the Hopf bifurcation (dashed red), the amplitude

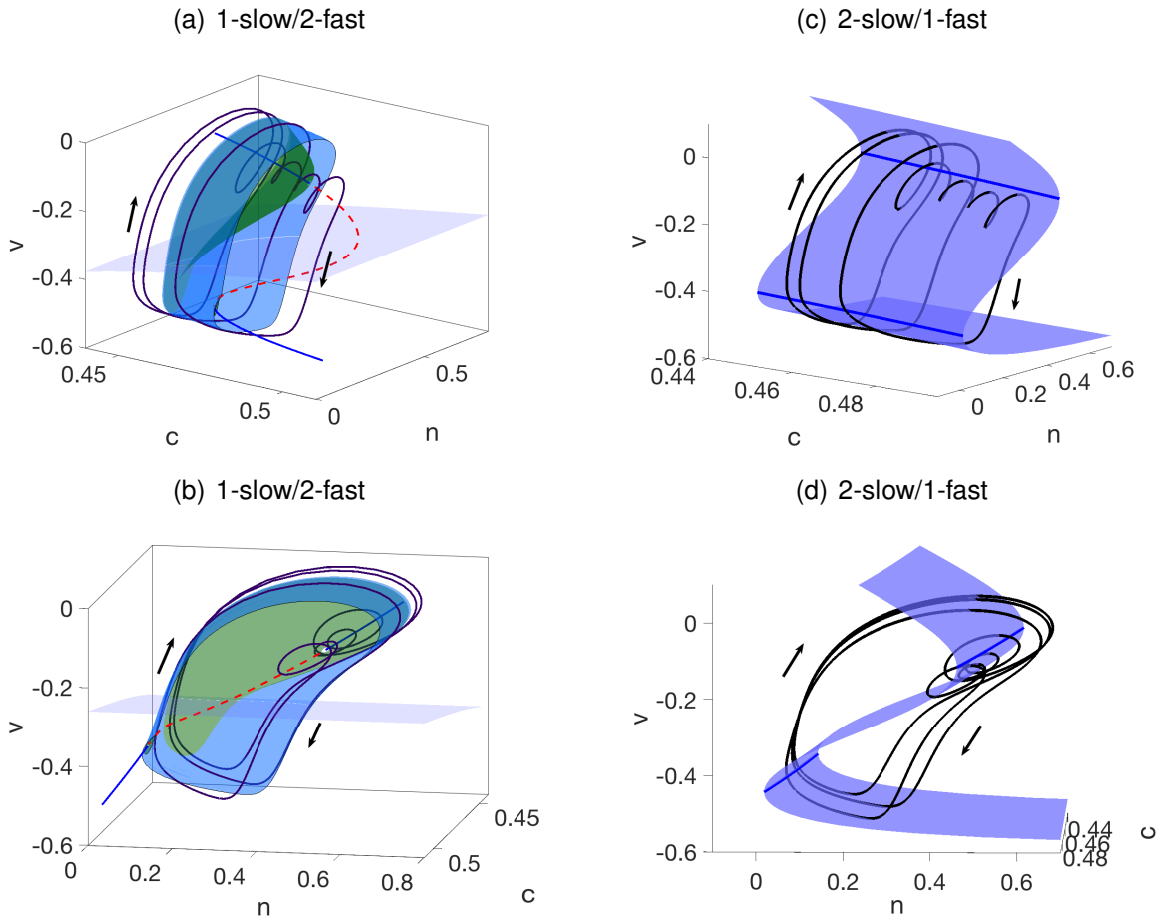

FIGURE 4.6. Different views of the fast subsystem in (4.15) (a)-(b) and Critical manifold in (4.11) (c)-(d) of the model when f_c= 0.0006.

of oscillations becomes larger as they move away from the Hopf bifurcation. Crossing the c-nullcline, the trajectory is attracted to the stable limit cycle manifold (blue surface), where the large single spikes are observed. However, the fast subsystem cannot explain the behaviour below the c-nullcline well, where the trajectory does not follow the stable limit cycle region as seen in Figures 4.6(a) and 4.6(b).

In Figures 4.6(c) and 4.6(d) we superimposed the complex orbit on the critical manifold. It is shown that the silent phase part of the trajectory is attracted to the lower attracting sheet of the critical manifold. The trajectory follows this invariant object and leaves when it crosses the fold curve.

Therefore, neither the 1-slow/2-fast nor the 2-slow/1-fast analysis can fully explain the mechanism of complex solutions. So far, we have considered the time scale constants calculated by the nondimensionalisation of the model. These constants are the lower bounds of the time scales of the state variables. However, the time scales of these variables change over time. For example, the time scale function of the variable n was introduced in the model equation, given by

$$\tau_n(v) = 0.0022 + 0.0029e^{-(vQ_v)/14.3} \tag{4.17}$$

In Figure 4.7, we plot the dynamic time scale function of n over the period of the complex solution shown in Figure 4.1(c) when f_c= 0.0006. The time scale range is $0.006 < \tau_n(v) < 0.126$. The lower bound of this range ($O(10^{-2})$) agrees with the estimated value from the time scale constant given by $\hat{\tau}_n := \frac{1}{\hat{T}_n Q_t}$, which is equal to 0.0051 ($O(10^{-2})$). However, the time scale function seen in Figure 4.7 shows rapid changes that correspond to the large spikes of complex solutions. This indicates that further research is needed in order to understand the mechanisms of such complex solutions according to the changes of the dynamic time scales.

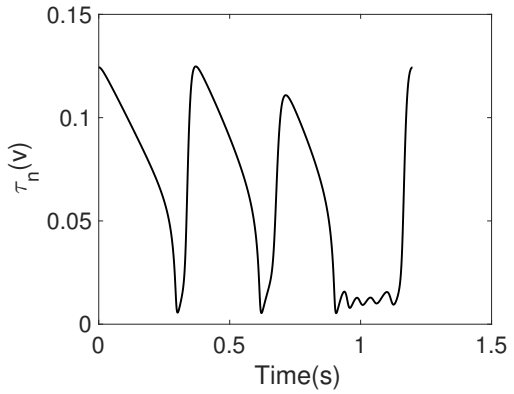

FIGURE 4.7. Dynamic time scale function $\tau_n(v)$ along the period of the solution when f_c= 0.0006.

We studied the parameter dependence of the (4D) and (3D) IHC models in Chapters 2 and 3, respectively. We investigated the single, bursting and complex oscillatory regions according to the changes of parameters g_{Ca}, $g_{\mathrm{K_{Ca}}}$ and p_{ER}. The time scale

constants calculated by nondimensionalisation indicate that the parameter g_{Ca} is inversely proportional to the time scales $\hat{\tau}_v$ and $\hat{\tau}_c$. In the following, we will investigate the effects of this parameter on the time scales and corresponding model solutions.

4.2.4 Effects of Varying g_{Ca} on the Time Scales

In the previous section, we investigated the full system periodic solutions in terms of slow-fast analysis as we varied the parameter f_c. However, in the previous chapters (particularly in Chapters 2 and 3) we considered the parameters g_{Ca}, $g_{\mathrm{K_{Ca}}}$ and p_{ER} that are directly involved in controlling the intracellular calcium dynamics of the IHC model. Specifically we showed how the model solutions depend on the physical parameters of the model, in particular the calcium conductance g_{Ca}, for the full IHC model (4D) in Chapter 2 and the reduced IHC model (3D) in Chapter 3. In this section, we investigate the role of g_{Ca} on the time scale constants and apply the slow-fast analysis to gain insight into the behaviour of the model solutions as this parameter changes.

The characteristic time scales of the reduced (3D) IHC model were estimated in Section 4.1.1 as

$$\hat{\tau}_v = \frac{C_{\mathrm{m}}}{Q_{\mathrm{t}} g_{\mathrm{max}}}, \quad \hat{\tau}_n = \frac{1}{\hat{T}_n Q_{\mathrm{t}}}, \quad \hat{\tau}_c = \frac{Q_{\mathrm{c}}}{Q_{\mathrm{t}} f_{\mathrm{c}} \alpha g_{\mathrm{Ca}} Q_{\mathrm{v}}}$$

The calcium conductance g_{Ca} affects time scale constants of the intracellular calcium ($\hat{\tau}_c$) and the membrane voltage ($\hat{\tau}_v$) in the case when g_{Ca} is the maximum of the conductances i.e. $g_{\mathrm{Ca}} > 2.85$. Moreover, g_{Ca} is inversely proportional to both $\hat{\tau}_v$ and $\hat{\tau}_c$. Thus, increasing g_{Ca} makes both the fast variable (v) and the slow variable (c) faster by decreasing their time scale constants.

We plot a one-parameter bifurcation diagram using g_{Ca} as the bifucation parameter in Figure 4.8 when $g_{\mathrm{K_{Ca}}}$=2, $p_{\mathrm{ER}} = 0.0015$ and $f_c = 0.004$. For small values of the control parameter, the stable equlibria (blue curve) undergo a a supercritical Hopf bifurcation (HB_1), at which a family of stable limit cycles is born. The inset in Figure 4.8 zooms

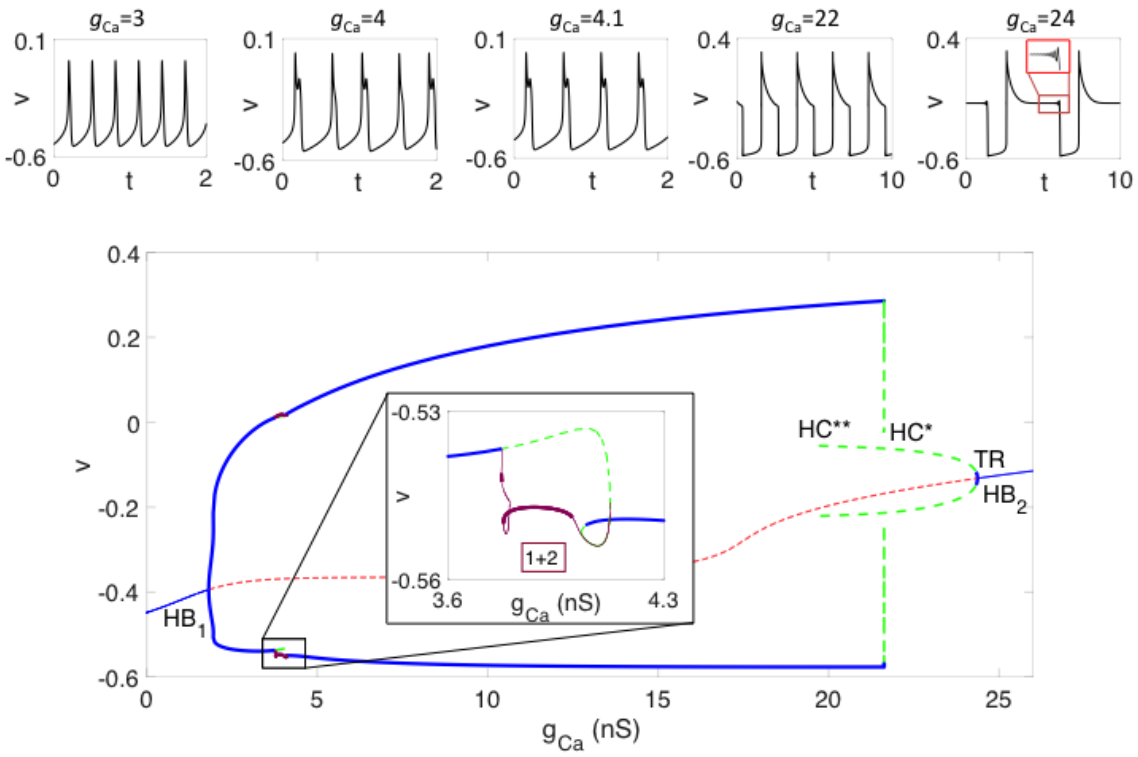

FIGURE 4.8. One parameter bifurcation diagram of the reduced (3D) IHC model for the parameters $g_{K_{Ca}}$=2, $p_{ER} = 0.00015$ and $f_c = 0.004$. We plot the time series solutions of some of the representative periodic orbits when g_{Ca}=3 (single spike), g_{Ca}=4 (complex: *1+2*), g_{Ca}=4.1 (bursting: *0+2*), g_{Ca}=22 (large periodic orbit) and g_{Ca}=24 (MMO) above the bifurcation diagram. Canard explosion, a sudden growth in the amplitude of the limit cycles [12], occurs near the second Hopf bifurcation (HB_2).

the family of complex periodic orbits (*1+2*). As g_{Ca} increases, the reduced IHC model exhibits single spike solutions that terminate at a homoclinic bifurcation HC*.

In Figure 4.9, we plot the fast subsystems and critical manifolds of the model for g_{Ca}=4 and g_{Ca}=4.1. It appears that we cannot apply the slow-fast analysis in these cases since the limit cycles of the full model do not follow the manifolds of fast and slow subsystems.

Table 4.1 shows the typical time scale constants for some representative periodic orbits, which are g_{Ca}=3 for a small single limit cycle, g_{Ca}=4 for the complex periodic

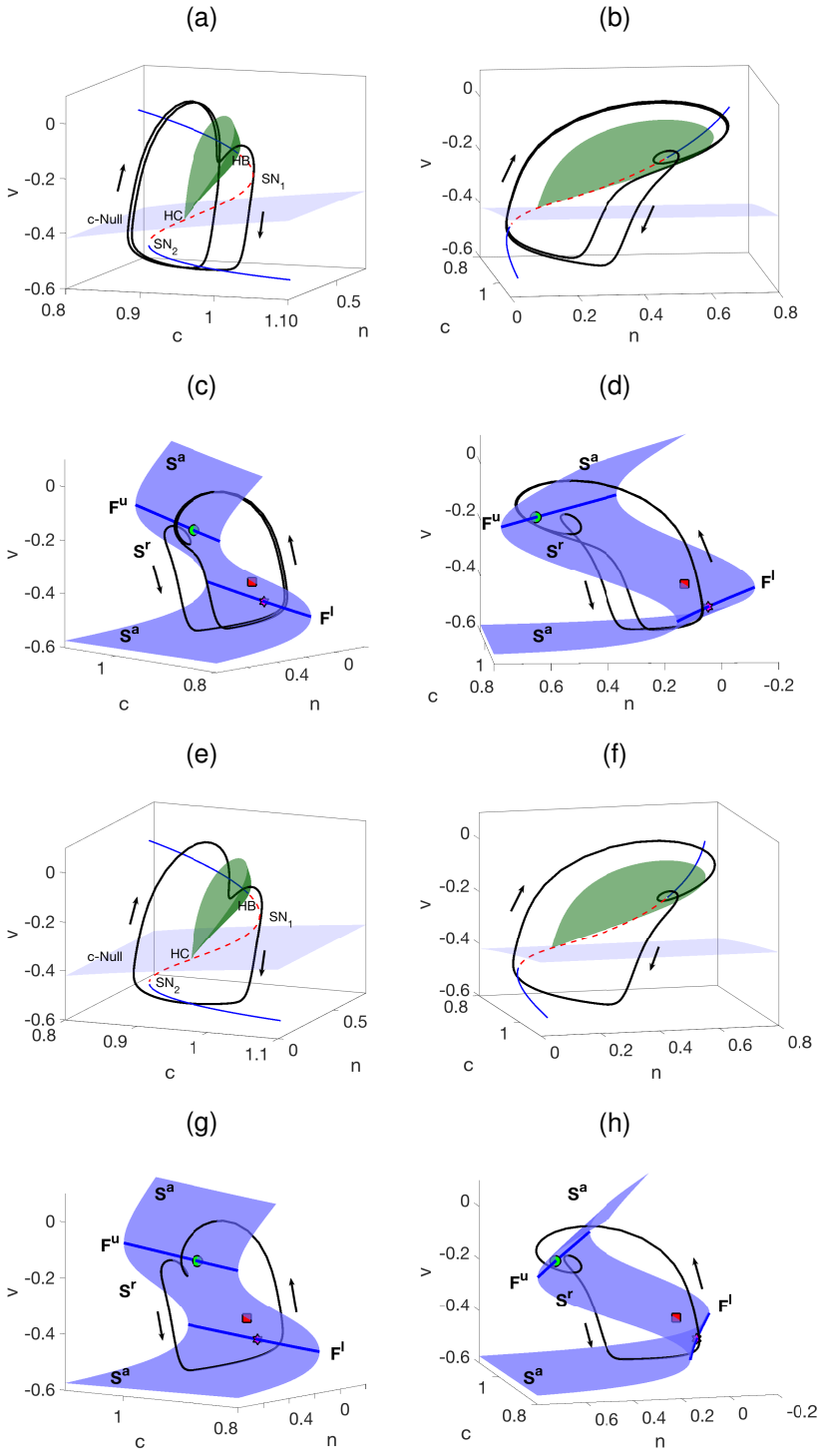

FIGURE 4.9. Different views of the bifurcation diagrams of the fast subsystem in (4.15) and critical manifolds in (4.11) respectively when g_{Ca}=4 (a)-(d) and g_{Ca}=4.1 (e)-(h).

orbit $1+2$, g_{Ca}=4.1 for a bursting solution with two small spikes, g_{Ca}=22 for a large single limit cycle and g_{Ca}=24 for a MMO (see the full model bifurcation diagram in Figure 4.8).

If $g_{\mathrm{Ca}} > 2.85 = g_{\mathrm{K}}$, then g_{Ca} becomes the maximum conductance in the model. Therefore, increasing g_{Ca} will affect the time scale constants of the variables v and c. The time scale constants in Table 4.1 clearly show that the time scale constant of c becomes smaller and of the same order ($O(10^{-2})$) as the variable n when g_{Ca}=22 and g_{Ca}=24. Additionally, the time scale constant of the fast variable becomes smaller ($O(10^{-4})$). Therefore, the reduced IHC model has one fast variable (v) and two slow variables (n and c) with the given set of parameters when g_{Ca}=22 and g_{Ca}=24 near the second Hopf bifurcation (HB_2) where a sudden growth in the amplitude of the limit cycles occur, which is called a canard explosion [12].

	g_{Ca}=3	g_{Ca}=4	g_{Ca}=4.1	g_{Ca}=22	g_{Ca}=24
$\hat{\tau}_v$	0.0024 [$O(10^{-3})$]	0.0018 [$O(10^{-3})$]	0.0017 [$O(10^{-3})$]	0.0003 [$O(10^{-4})$]	0.0003 [$O(10^{-4})$]
$\hat{\tau}_n$	0.0051 [$O(10^{-2})$]	0.0051 [$O(10^{-2})$]	0.0051 [$O(10^{-2})$]	0.0051 [$O(10^{-2})$]	0.0051 [$O(10^{-2})$]
$\hat{\tau}_c$	0.1137 [$O(10^{-1})$]	0.0853 [$O(10^{-1})$]	0.0832 [$O(10^{-1})$]	0.0155 [$O(10^{-2})$]	0.0142 [$O(10^{-2})$]

Table 4.1: Time scale constants for g_{Ca}=3, g_{Ca}=4, g_{Ca}=4.1, g_{Ca}=22 and g_{Ca}=24.

Since the reduced IHC model has one fast (v) and two slow (n and c) variables when g_{Ca}=22 and g_{Ca}=24, we investigate the behaviour of the periodic orbit in terms of a slow-fast analysis (2-slow/1-fast case) similar to the analysis of MMO in the previous section.

The critical manifold is defined by the set

$$S := \{(v,n,c) \in \mathbb{R}^3 \quad | \quad F(v,n,c) = 0\}$$

where $F(v,n,c) := -\hat{I}_{\mathrm{Ca}}(v,c) - \hat{I}_{\mathrm{K}}(v,n) - \hat{I}_{\mathrm{K_{Ca}}}(v,c) - \hat{I}_{\mathrm{leak}}(v)$, which represents a surface in the (c,n,v)-coordinate system.

We plot the critical manifold and the slow flow of the desingularised system in Figure 4.10. The thin cyan coloured curves are the trajectories of the slow flow on the

(a) Critical manifold

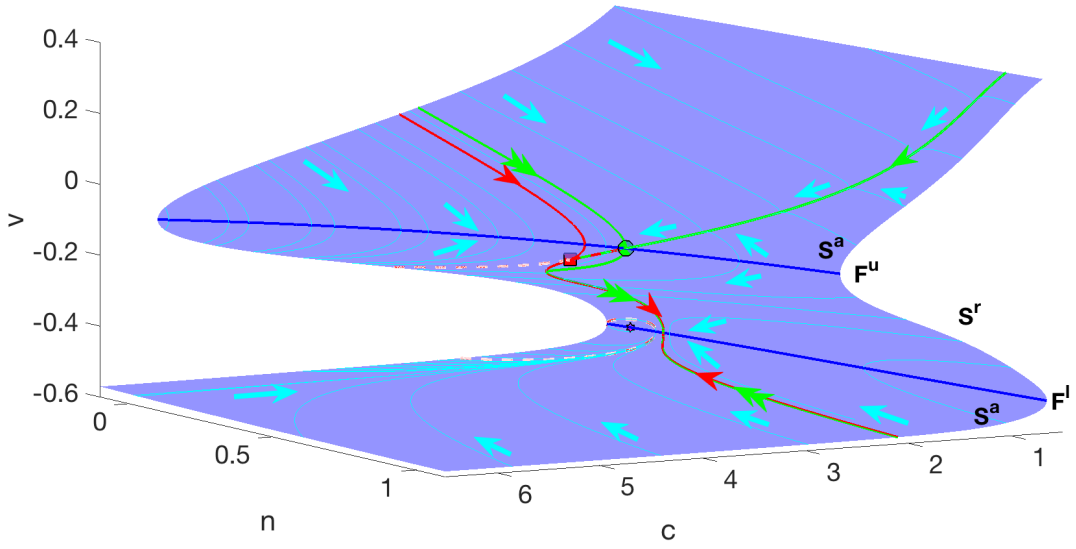

(b) Upper fold

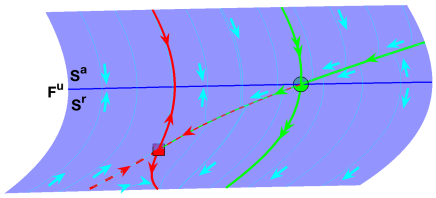

(c) Lower fold

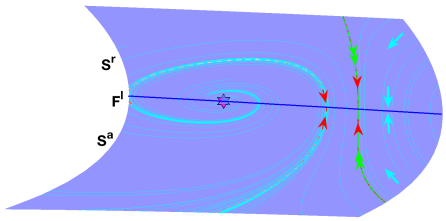

FIGURE 4.10. The critical manifold in (4.11) when g_{Ca}=22. The thin cyan curves are the trajectories of the slow flow in (4.14).The green curves are strong (double arrows) and weak (single arrows) stable manifold of the node (green circle) on the lower fold curve (F^l). The red curves are the stable (solid) and unstable (dashed) manifolds of the saddle equilibrium on the repelling sheet (S^r) at the critical manifold. The magenta star is the folded focus on the lower fold curve (F^l).

critical manifold. The green curves are the strong (double arrows) and weak (single arrow) stable manifolds of the folded node on F^u denoted by a green circle. Additionally, there is another folded singularity on the lower fold curve, which is denoted by a magenta star. The eigenvalues of the Jacobian matrix of the desingularised system evoluated at this folded singularity are $\sigma_{1,2} = -0.0164 \pm i0.076$. Thus, this is a

(a) Critical manifold

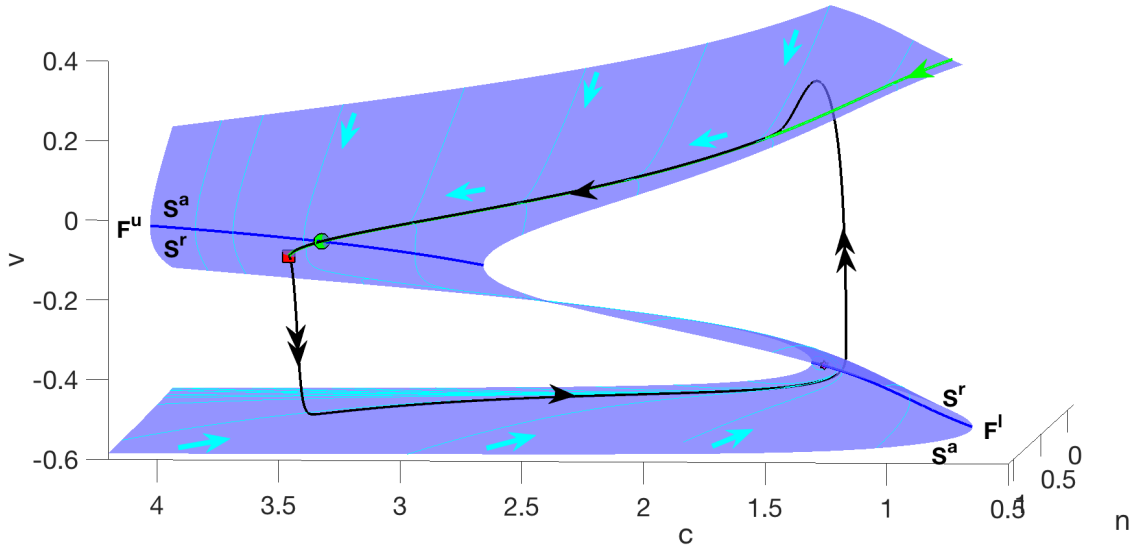

(b) Upper fold

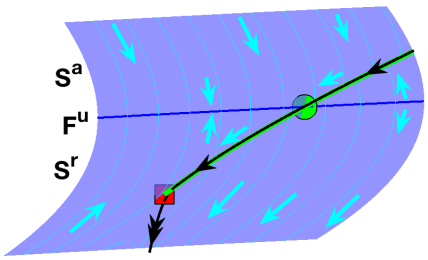

(c) Lower fold

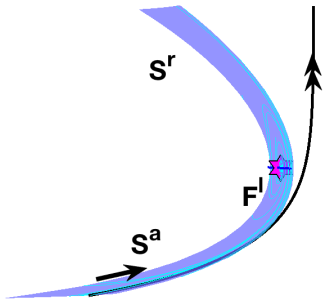

FIGURE 4.11. The periodic orbit when g_{Ca}=22 is superimposed on the critical manifold in (4.11). The trajectory follows the repelling part of the critical manifold as shown in (b), which is called a canard segment.

folded-focus [16].

Also, there is another equilibrium point of the desingularised system. This is a saddle-node equilibrium shown as a red square on the repelling part, which is also an equilibrium (saddle) of the full model. We plot the stable (solid red curve) and unstable (dashed red curve) manifolds of the saddle-node equilibrium of the desingularised system by reversing the direction of the slow flow on the repelling branch of the critical manifold.

In Figure 4.11, we superimposed the periodic orbit when g_{Ca}=22 on the critical manifold. On the lower attracting sheet of the critical manifold, the orbit moves following the slow flow (denoted by cyan coloured single arrows). As it gets closer to the lower fold (F^l), the attraction becomes weaker and the orbit jumps up to the upper attracting sheet of the manifold (denoted by double arrows). Once the orbit reaches the upper attracting sheet, it follows the slow flow. The green curve on the upper sheet is the weak stable manifold of the node (green circle) on the upper fold (F^u). The orbit continues following the weak stable manifold after the node until near the saddle equilibrium denoted by a red square (also a saddle equilibrium of the full model), where this path on the repelling sheet is also part of the two-dimensional unstable manifold of the saddle of the full model. Once the orbit gets closer to the saddle equilibrium, it moves to the lower attracting sheet of the critical manifold and completes the cycle.

As we increase g_{Ca} from 22 to 24, we showed that the model still has one fast (v) and two slow (n and c) variables. The time series of the periodic orbits at g_{Ca}=22 and g_{Ca}=24 are shown in Figure 4.8. At g_{Ca}=24, the small oscillations occurs at the end of the active phase of the bursting which was not seen at the periodic orbit when g_{Ca}=22.

The structure of the equilibria of the desingularised system when g_{Ca}=24 shown in Figure 4.12 is the same as the desingularised system when g_{Ca}=22 (see Figure 4.10). Both have a folded node on F^u, a folded focus on F^l and a saddle equilibria of the desingularised system on the repelling sheet of the critical manifold. However, although the equilibrium of the full model when g_{Ca}=22 is a saddle, whose eigenvalues are λ_1=99.29, λ_2=46.28 and λ_3=-12.14, the equilibrium of the full model when g_{Ca}=24 is a saddle-focus, whose eigenvalues are $\lambda_{1,2} = 10.34 \pm i123.62$ and λ_3=-5.31. These equilibria are saddle equilibria of the desingularised systems when g_{Ca}=22 and g_{Ca}=24, which are shown as red squares in Figures 4.10 and 4.12.

If we superimpose the periodic orbit when g_{Ca}=24 on the critial manifold in Figure 4.13, we note that the orbit behaves similarly as the orbit when g_{Ca}=24 shown in Figure 4.11.

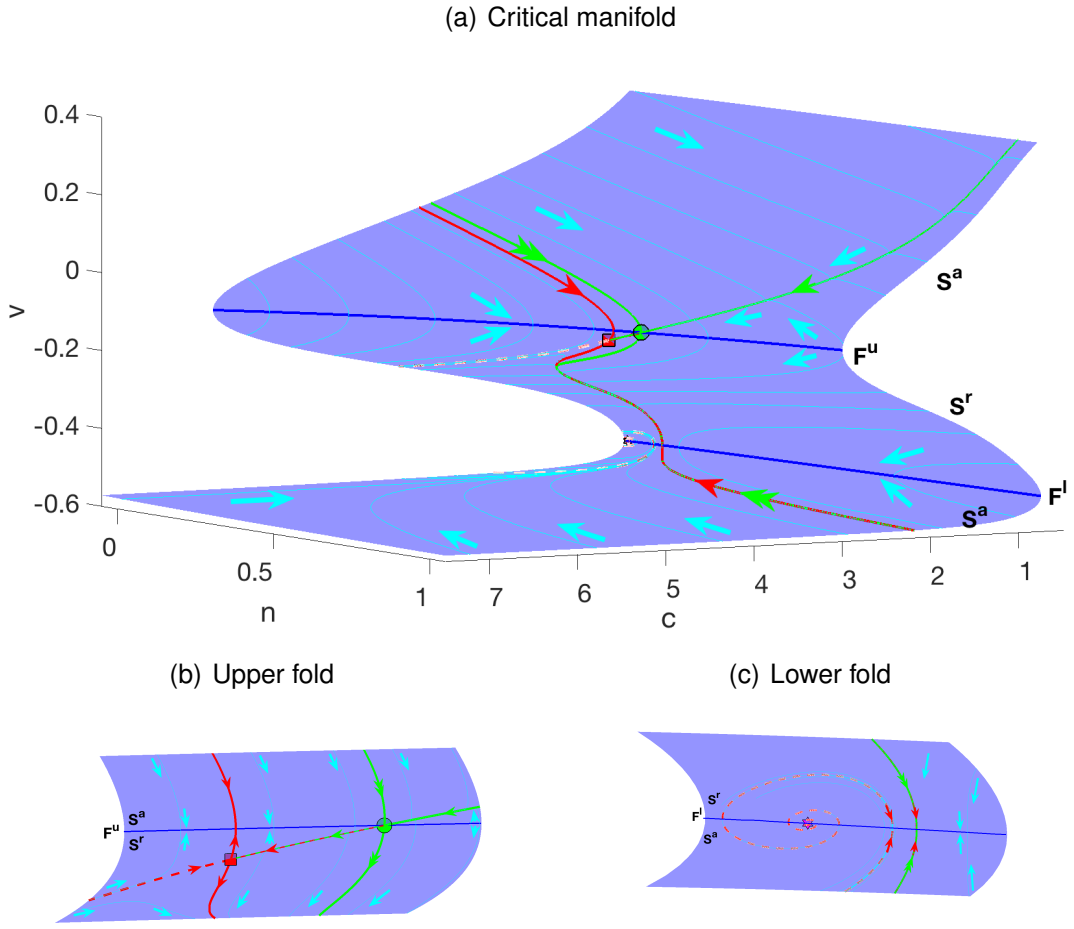

FIGURE 4.12. The critical manifold in (4.11) when g_{Ca}=24. The thin cyan curves are the trajectories of the slow flow in (4.14). The green curves are strong (double arrows) and weak (single arrows) stable manifold of the node (green circle) on the lower fold curve (F^l). The red curves are the stable (solid) and unstable (dashed) manifolds of the saddle equilibrium on the repelling sheet (S^r) at the critical manifold. The magenta star is the folded focus on the lower fold curve (F^l).

The orbit moves according to the slow flow on the lower attracting sheet of the critical manifold. As it gets closer to the lower fold (F^l), the attraction becomes weaker and the trajectory jumps up to the upper attracting sheet. Once it reaches the upper attracting sheet, it follows the weak stable manifold (green curve) of the node on F^u.

In Figure 4.13, the small oscillations or the periodic orbit when g_{Ca}=24 are seen near

(a) Critical manifold

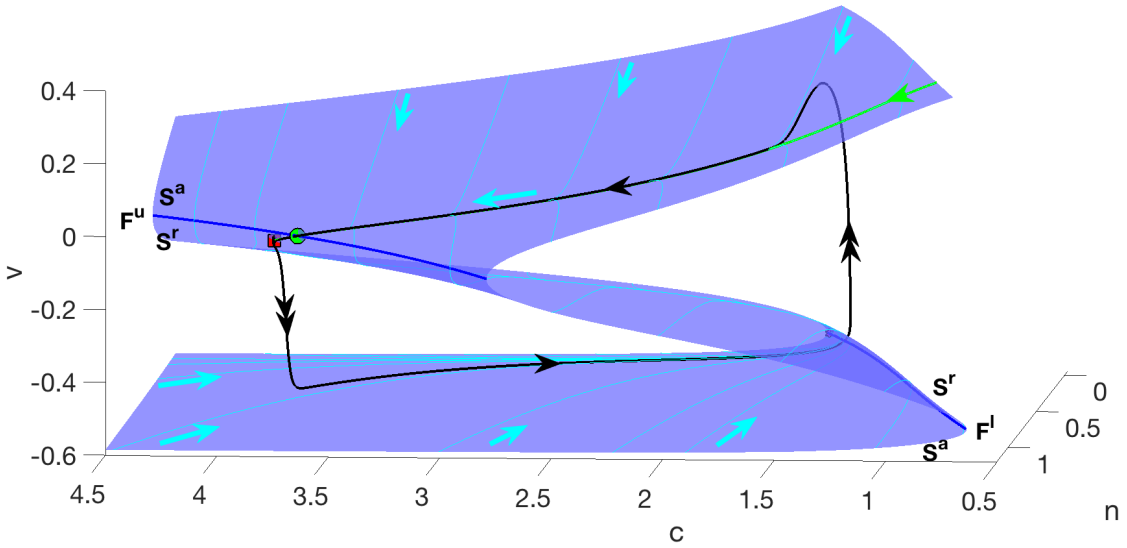

(b) Upper fold

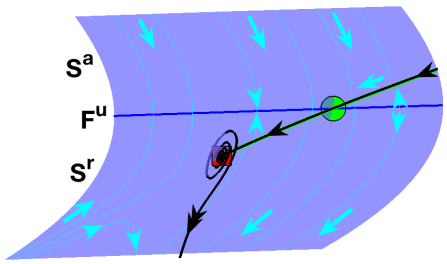

(c) Lower fold

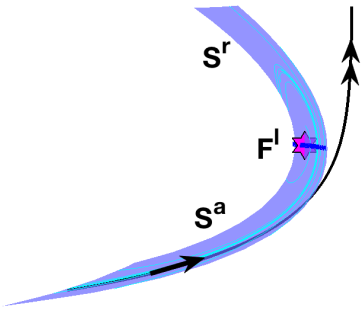

FIGURE 4.13. The periodic orbit when g_{Ca}=24 is superimposed on the critical manifold in (4.11). In (b) the trajectory follows the repelling part of the critical manifold i.e a canard segment.

the saddle on the repelling sheet of the manifold (S^r). Since this is a saddle-focus equilibrium of the full model, the small oscillations spiral away from the equilibrium along its two dimensional unstable manifold [16]. As the oscillations grow and repeatedly intersect the repelling sheet, the trajectory of the orbit moves the lower attracting sheet of the critical manifold and completes the cycle.

4.3 Conclusion

In this chapter, we have investigated the dynamics underlying the oscillations of the reduced (3D) IHC model applying a slow-fast analysis. In Chapter 3, we showed the characteristic time scale constants of the dynamic variables of the model that enables us to estimate the speed of the state variables according to the changes of the model parameters.

Although we have not studied the effect of varying the parameter f_c (the fraction of free to total cytosolic calcium) on the original and reduced IHC model solutions in Chapters 2 and 3, the characteristic time scales of the model reveal that the parameter f_c appears only in the time scale constant of the variable c. Therefore, we varied parameter f_c and showed that the reduced IHC model exhibits bursting solutions, complex solutions with one and two large spikes, normal spiking and MMOs. Hence we investigated the underlying mechanisms of these solutions according to the differences between time scales.

First, we showed that the model has two fast (v and n) and one slow (c) variables when f_c is small (f_c=0.000235) where the model exhibits bursting oscillations. We applied the classical 1-slow/2-fast analysis [78] to interpret the periodic orbit of the reduced model by its fast-subsystem structure. On the other hand, as f_c increases one order of magnitude (f_c=0.00244), the slowest variable becomes faster and the model has one fast (v) and two slow (n and c) variables. We showed how the periodic orbit (mixed mode oscillations (MMOs)) when f_c=0.00244 interacts with the critical manifold and slow flow using the 2-slow/1-fast analysis [16].

The model exhibits complex solutions for intermediate values of f_c (for instance, solution *1+11* when f_c=0.0004 and *2+5* when f_c=0.0006). However, neither the 1-slow/2-fast nor the 2-slow/1-fast analyses could explain sufficiently well the dynamic mechanisms underlying these complex solutions. Instead of the typical time scale constant of n, we plotted a time series solution of the time scale n along the complex

periodic orbit. It revealed that the amplitude of time scale function rapidly changes during the large (normal) spiking of complex solutions. However, the characteristic time scale constants calculated by the nondimensionalisation are lower bounds of these dynamics time scales functions. These rapid changes could be explained considering the model evolving on three-time scales. Different parts of complex solutions could be governed by different subsystems and evolved under the fast, slow and super-slow flows [69, 101]. Therefore, a further research is needed in order to understand fully the mechanisms of such complex solutions according to the changes of the dynamic time scales. We can summarise the results in Table 4.2.

Parameter	Type of pattern	$\hat{\tau}_c$	Type of analysis
f_c=0.000235	Bursting	2.4184	Studied by 1-slow/2-fast analysis. Its fast subsystem diagram is shown in Figure 4.2.
f_c=0.0006	Complex (*2+5*) solution	0.9474	1-slow/2-fast and 2-slow/1-fast analyses can partially explain the mechanism. Its fast and slow subsystem diagrams are shown in Figure 4.6.
f_c=0.00244	MMO	0.2330	Studied by 2-slow/1-fast analysis. Its S-shaped critial manifold and the trajectories of the slow flow are shown in Figure 4.5.

Table 4.2: Summary of the slow-fast analysis of the three representative model solutions shown in Figure 4.1. The time scale constants for the variables v and c are $\hat{\tau}_v = 0.0004$ and $\hat{\tau}_n = 0.0051$, respectively.

In Chapters 2 and 3, we investigated the effect of varying the parameter g_{Ca} on the model solutions and showed that for larger values of g_{Ca}, the plateau oscillations of bursting solutions become harder to visualise. Also, the time scale constants indicate that the parameter g_{Ca} is inversely proportional to both time scales of the variables v and c when $g_{\mathrm{Ca}} > 2.85$. Therefore, we investigated the model solutions considering g_{Ca} as the maximum conductance in the model. Since large values of g_{Ca} correspond

to a faster speed of both v and c, the variables c evolves on a similar time scale as n ($O(10^{-2})$) that is much slower than the variable v ($O(10^{-4})$). Hence, the periodic orbits observed at high values of g_{Ca} can also be studied by a 2-slow/1-fast analysis. However, when g_{Ca} is small, the time scales of v, n and c are of an order $O(10^{-3})$, $O(10^{-2})$ and $O(10^{-1})$, respectively. Similarly to the periodic solutions for intermediate values of f_c, the periodic orbits when g_{Ca} is small could also be studied by considering three-time scales.

We also studied MMOs observed at larger g_{Ca} whose small oscillations occur at the end of the active phase of bursting. We showed that although the dynamic structures of the desingularised systems are the same for different values of g_{Ca} (large periodic orbit when g_{Ca}=22 and MMOs when g_{Ca}=24), the full model equilibrium could help us to explain the behaviour of the periodic orbits near the equilibrium. The main difference between the periodic solutions at g_{Ca}=22 and g_{Ca}=24 is the equilibrium points of their full model. The equilibrium when g_{Ca}=22 is a saddle. Thus, the trajectory of the orbit on the repelling sheet of the critical manifold directly moves to the lower attracting sheet near the saddle-focus. However, the trajectory of the MMO on the repelling sheet spirals away from a saddle-focus equilibrium and moves to the lower attracting sheet in the case of g_{Ca}=24.

We calculated such MMOs at larger values of g_{Ca} by direct numerical integration [22], which are close to the torus bifurcation originating from the Hopf bifurcation. However, at larger values of g_{Ca} we could not continue such MMOs as g_{Ca} varies to reveal the organisation of such branches according to the number of their small oscillations so that we could investigate the subsequent period-doubling and torus bifurcations resulting in chaotic MMOs [26].

CHAPTER 5

CONCLUSION

In this chapter, we summarise the main results we have obtained, discuss the challenges we have faced performing this research and suggest future investigations.

5.1 Summary and Discussions

The aim of this thesis is to gain deeper knowledge of the electrical activity and Ca^{2+} signalling during the development of inner hair cells (IHCs) from a mathematical point of view. We applied nonlinear dynamical systems theory to explain the oscillatory behaviour of these cells.

There are three parameters in the IHC model that control calcium regulation, namely $g_{K_{Ca}}$ (the maximum Ca^{2+}-activated K^+ channel conductance), p_{ER} (the rate of Ca^{2+}-induced calcium release (CICR)) and g_{Ca} (the maximum calcium channel conductance). The upstroke of the action potential in immature IHCs is generated by a calcium influx through calcium channels on the cell membrane and results in a rise in intracellular calcium [38, 63, 75]. The IHC model supports periodic and chaotic solutions of complex (mixed) type, that are composed of single (normal) spikes and pseudo-plateau

burstings, similar to the experimental data [31, 90].

Although previous studies [31, 90] investigated the effects of the parameters $g_{\mathrm{K_{Ca}}}$ and p_{ER}, the effects of varying the parameter g_{Ca} on model solutions had not yet been addressed. Therefore, we performed a further numerical bifurcation analysis in order to gain an insight into the effect of changing the maximum calcium channel conductance and to present a more complete characterisation of the relative contributions of these three parameters in Chapter 2.

In Chapter 2, we demonstrate that the number of large (normal) spikes of complex periodic orbits decreases and, eventually, complex solutions become pseudo-plateau bursting solutions as g_{Ca} increases. For larger values of g_{Ca}, the plateau oscillations of bursting solutions become harder to visualise and the amplitude and duration of the intracellular Ca^{2+} increases significantly.

We also confirmed that the periodic orbits, whose total number of oscillations is fixed, lie on the same isolated solution branches (or isolas [90]) that are disconnected from the other branches originated from Hopf bifurcations, which gives an indication that those periodic orbits belong to a continuous family of periodic solutions sharing the same total number of spikes. We computed a broad range of periodic attractors, which are normal spiking, pseudo-plateau bursting with several plateau oscillations and complex solutions with one and two large (normal) spikes, and continued the bifurcations that result in a change of the stability of the periodic solutions, which are period-doubling (PD) and saddle-node bifurcation of periodic solutions (SNp), into two parameters. Thus, we characterised the behaviour of stable periodic orbits according to changes of the three parameters using several two-parameter bifurcation diagrams. These two-parameter sections of the three-parameter space enabled us to estimate the changes in the asymptotic behaviour of the IHC model.

Our numerical bifurcation analysis in Chapter 2 reveals the parameter regions for different types of solutions in the IHC model according to the variations of these three

parameters. If we increase the parameter g_{Ca} in the model, the parameter p_{ER} must be increased while the parameter $g_{\mathrm{K_{Ca}}}$ decreases accordingly in order to get similar behaviour such as normal spiking pattern, pseudo-plateau burstings and complex solutions with one or two large spikes. For instance, Table 5.1 shows the parameter ranges of $g_{\mathrm{K_{Ca}}}$ and p_{ER} for two different values of g_{Ca} i.e. g_{Ca}=2.4 and g_{Ca}=6, where the IHC model exhibits complex solutions with one large (normal) spike and several plateau oscillations. Similar estimations can be done for the parameters $g_{\mathrm{K_{Ca}}}$ and p_{ER} using these two-parameter bifurcation diagrams.

	$g_{\mathrm{K_{Ca}}}$	p_{ER}
g_{Ca}=2.4	[1.5, 40]	[0, 0.0005]
g_{Ca}=6	[0.6, 0.7]	[0.0028, 0.0030]

Table 5.1: The ranges of the parameters $g_{\mathrm{K_{Ca}}}$ and p_{ER} for different values of g_{Ca} having complex solutions with one large spike and several small spikes.

In Chapter 3, we propose a reduction of the four-dimensional IHC model. Identifying the slowest variable, which is the inactivation variable associated with the voltage-gated K^+ channels (h), we were able to reduce the dimension of the IHC model by considering h as a fixed quantity resulting in a reduced (three-dimensional) IHC model.

In order to verify that we do not lose the essential dynamic features of the original IHC model by fixing the slowest variable h, we presented a characterisation of the relative contributions of the three parameters on the reduced IHC model solutions, which is a similar analysis to that in Chapter 2 for the original IHC model. The two-parameter bifurcation diagrams of the reduced IHC model confirm the qualitative agreement between the reduced and the original models. Therefore, we conclude that we could investigate the simpler (3D) model without losing the dynamic properties of the original (4D) model. Additionally, we no longer have to use projections of the original model in the visualisations of the reduced model solutions [104]. This allows us to capture the true representation of the trajectories in three dimensions and how various periodic orbits are organised without projections.

Moreover, the nondimensionalisation of the IHC model provides the typical time scale constants of the dynamic variables that enable us to classify the state variables as fast and slow according to the changes of the model parameters. Hence, having identified differences between the time scales of the reduced (3D) IHC model, we are able to apply slow-fast analysis in order to better understand the mechanisms underlying the dynamics of the model solutions in Chapter 4.

The typical time scale constants reveal the contribution of the model parameters on the speed of the state variables. It was shown that the parameter f_c (the fraction of free to total cytosolic calcium) appears only in the time scale of the variable c. Therefore, varying f_c directly affects the speed of c. We demonstrate that the reduced IHC model exhibits bursting solutions, complex solutions with one and two large spikes, normal spiking and MMOs as the parameter f_c increases, which makes the slow variable faster. Thus, it was shown that the model produces a broad range of periodic orbits varying a single parameter f_c. Next, we consider the speed of the variables for such periodic orbits in order to apply slow-fast analysis.

The typical time scale constants also indicate that the reduced IHC model can be characterised by two fast (v and n) and one slow (c) or one fast (v) and two slow (n and c) variables depending on the choice of parameters. In particular, we show that the mechanism underlying the bursting solutions can be understood by considering the fast subsystem dynamics i.e. the 1-slow/2-fast analysis when f_c is small. If we make the slow variable c faster by increasing the parameter f_c, the model exhibits MMOs, which can be studied by the 2-slow/1-fast analysis.

Also, the typical time scale constants reveal that the parameter g_{Ca} is inversely proportional to the time scales of both c and v when it dominates the other conductances in the model. When g_{Ca} is large, the slow variable (c) evolves at the same time scales as n ($O(10^{-2})$) and the fast variable v evolves at a much faster time scale ($O(10^{-4})$). Therefore, the model has one fast (v) and two slow (n and c) variables. Hence, the pe-

riodic orbits observed at high values of g_{Ca}, where the plateau oscillations of bursting solutions become harder to visualise, can also be studied by a 2-slow/1-fast analysis.

We also studied a MMO observed at larger g_{Ca}, which is close to a torus bifurcation on the branch of small amplitude limit cycles originating from the Hopf bifurcation. The small oscillations of such MMOs occur at the end of the active phase of bursting. In the review article [16], MMOs are studied with a three-dimensional model of chemical reactors introduced by Koper [48, 51], where they observed two small oscillation epochs near the maximum and minimum of large spikes in a narrow parameter region. In this thesis we investigated that MMOs, where the small oscillations are found at the end of the active phase of bursting. We show that such solutions are organised by a folded node of the desingularised system and a saddle-focus equilibrium of the full model. We also show that although the dynamic structures of the desingularised system are the same for different values of g_{Ca}, the type of the full model equilibrium (i.e. focus or saddle-focus) can help to explain the overall behaviour of the periodic orbits. In particular, the small oscillations of such MMOs when g_{Ca} is large can be interpreted by considering the saddle-focus equilibrium of the full model.

However, there are still limitations in our understanding this type of MMOs. For instance, we solved numerically the model equation to find such MMOs that are not found on solution branches originating from the Hopf bifurcations. Therefore, we do not know how the solution branches of these MMOs are organised according to the number of their small spikes although direct numerical integration shows the number of small oscillations increases as the parameter g_{Ca} gets closer the torus bifurcation in the full IHC model for large values of g_{Ca}.

5.2 Future Direction for Investigation

In Chapters 2 and 3, we verified the periodic solutions of the original (4D) and reduced (3D) IHC models whose total number of oscillations is equal (for instance *2+5* solutions

and *1+6* solutions shown in Figure 2.3) lie on the same isolated solution branch, which indicate they belong to the same family of periodic solutions. The isolas are interrupted on their unstable parts by homoclinic bifurcations at some parameter sets. We continued the PD and SNp bifurcations in two-parameters to indicate the stable regions of such periodic attractors. However, we have not continued the homoclinic bifurcations in the two-parameters. Thus, we do not know if these bifurcations explain the relation between the branches originating from Hopf bifurcations and isolas as well as the origin of the pseudo-plateau and complex solutions. Since these solutions with same number of spikes are connected in the parameter space sharing the same isola, the isola center [15] of the family of isolas could explain the origin of such periodic orbits.

Additionally, we showed several two-parameter sections of the three-dimensional parameter space to give an indication about the organisation of the periodic solutions with different number of large and small spikes of the original (4D) and reduced (3D) IHC models at the (g_{Ca}, $g_{\mathrm{K_{Ca}}}$, p_{ER})-space. Although these maps indicate the parameter regions for various periodic orbits of the models according to the variations of these three parameters, we did not compute a complete view of solutions in 3D-space to display how these solutions connect and disconnect [4] when they have different numbers of large and small spikes. This, on the other hand, will make the visulalisation of the regions of solutions harder due to the complicated organisational structure of the solutions as indicated by slices of three-parameter space. However, since the periodic solutions are born as a result of Hopf bifurcations and isolas are found between two Hopfs in the models, such a complete view could give an insight into how the periodic orbits having various numbers of total spikes appear and disappear in the parameter space.

Also, we identified the parameter regions (white regions in the two-parameter bifurcation diagrams) where the original (4D) and the reduced (3D) IHC models exhibit irregular (chaotic) mixed firing patterns (see Figures 2.10 and 3.9) that were also seen

in the experiments (see Figure 1.5). Although we discussed possible dynamic mechanisms underlying the aperiodic trajectories found in the model, a deeper investigation of the routes to chaos, such as period-doubling cascades, quasi-periodic motions or other mechanisms in the IHC model, is left for future studies.

We showed the Poincaré sections of these irregular trajectories of model solutions in order to give an indication about chaotic behaviour in the model. However, chaos is associated with exponential growth of infinitesimal perturbations, which is characterized by the spectrum of Lyapunov exponents [20, 28]. Therefore, calculating Lyapunov exponents gives more information about the nature of such trajectories i.e. Kaplan-Yorke dimension, dissipation rate etc. [42, 57, 107] and could help gaining an insight into the mixed firing pattern observed in the experiments since experimental time series can be used to compute the embedding dimension and delay time in phase space reconstruction [1, 59, 60] to calculate their maximal Lyapunov exponent [106].

In Figure 5.1 (a), we show a chaotic time series of the reduced (3D) IHC model when g_{Ca}=2.6, , $g_{\mathrm{K_{Ca}}}$=0.65 and p_{ER}=0.001 with the given parameters in Chapter 1. The positive exponent λ_1 indicates the chaotic motion. Additionally, the experiments also show irregular mixed firing patterns. Such time series is embedded into a delay reconstructed phase space to calculate their maximal Lyapunov exponent shown in Figure 5.1 (b).

The chaotic regions appear in two-parameter bifurcation diagrams of both the original and reduced IHC model discussed in Chapters 2 and 3, respectively. Investigating various regions of chaotic solutions could help us to understand if there are any similarities and differences between those regions and the experimental data sets.

In Chapter 4, we tried to understand the dynamics of the complex periodic orbits of the IHC model using 1-slow/2-fast or 2-slow/1-fast analysis. However, neither the 1-slow/2-fast nor the 2-slow/1-fast analysis can fully explain the mechanism of complex solutions. The time scale constants calculated by the nondimensionalisation of the

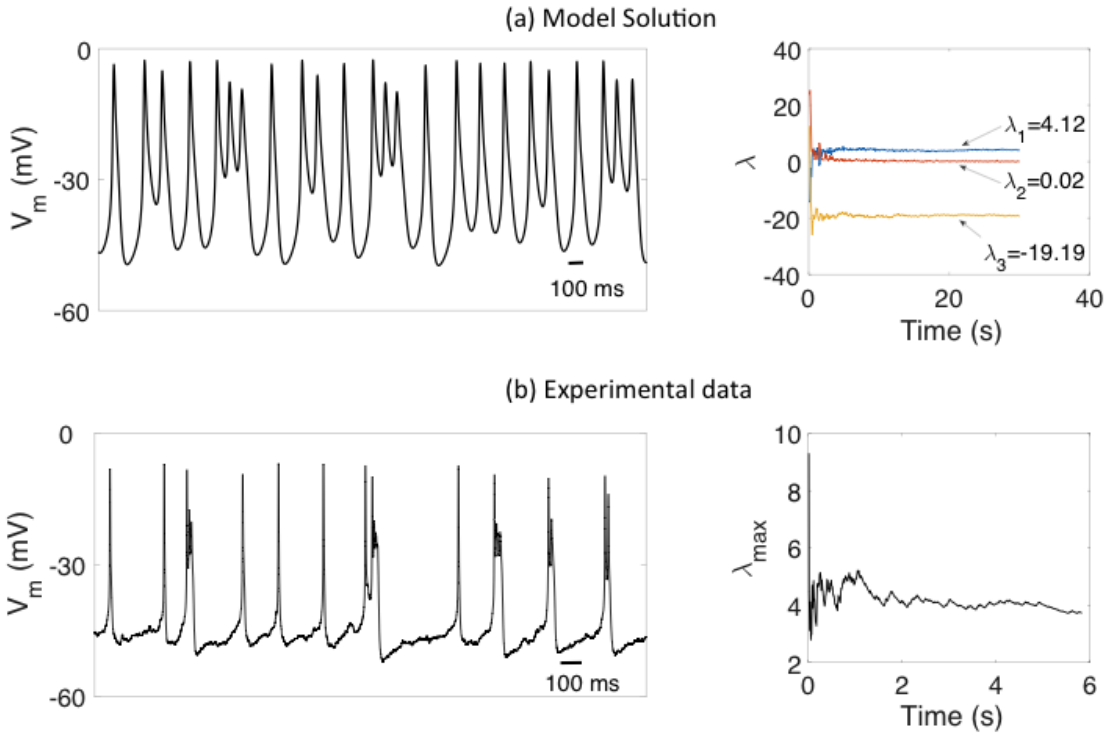

FIGURE 5.1. (a) Chaotic time series of the reduced IHC model when g_{Ca}=2.6, $g_{K_{Ca}}$=0.65, p_{ER}=0.001 and its dynamic Lyapunov spectrum. (b) Experimental data obtained from immature IHCs and its maximal Lyapunov exponent.

model are the lower bounds of the time scales of the state variables. However, the time scales of these variables change over time. We plotted a time series solution of the time scale of n $(\tau_n(v))$ for a complex solution in Figure 4.7. The time scale function shows rapid changes that correspond to the large (normal) spiking of complex solutions.

As seen in [101], trajectories of a three-time scale model could be explained locally by the interactions of two-time scales groups of the full three-time scale system. Additionally, the classical slow-fast analysis developed for two-time scale systems can be extended to three-time scale systems. In [69], a three-time scale model were

studied by reduced and layer problems as well as one fast-slow and a slow-superslow. They showed how the orbits of the full system are governed by the subsystems and evolved under the fast, slow and superslow flows. Since the time scales of complex solutions of the IHC model show rapid changes, this could be studied as a three-time scale phenomena. Therefore, further research is required in order to understand the mechanisms of the complex solutions in the IHC model according to the changes of the dynamic time scales.

APPENDIX A

CALCULATING AN AVERAGE VALUE FOR THE SLOWEST VARIABLE h

In Chapter 3, we discuss the simplification of the original (4D) IHC model. We show that the slowest variable in the IHC model is the inactivation variable h for the voltage-gated K^+ channel. In order to determine the range of the variable h over a large span of the parameter space for which the IHC model exhibits various types of periodic solutions, we consider three parameter sets for performing a bifurcation analysis. Then, we calculate an average value of h using the one-parameter bifurcation diagrams shown in Figures A.1, A.2 and A.3.

The dynamic value of the inactivation variable h varies between 0 and 1 since it represents the probability of the gate being open, which depends on the membrane potential V_{m}, and changes along periodic orbits. We plotted dynamic values of the variable h on the y axis at these bifurcation diagrams where periodic orbits of the IHC model are in the form of single spikes, pseudo-plateau bursting and mixed type (complex) solutions with different numbers of spikes. The average value is calculated considering the midrange values between the maximums and minimums (i.e. $(h_{\mathrm{Max}} +$

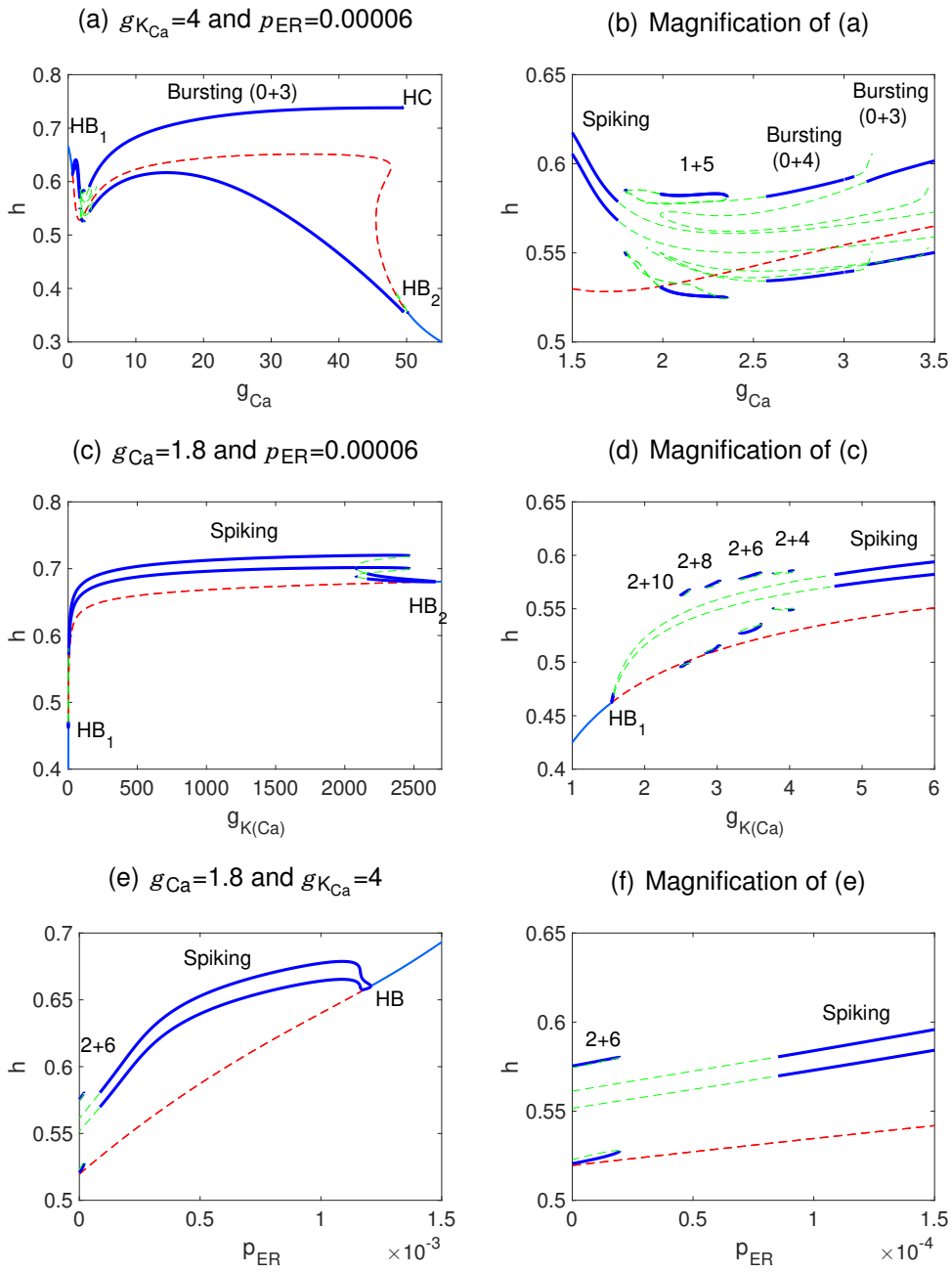

FIGURE A.1. One-parameter bifurcation diagrams. The parameters for the parameter set 1 are g_{Ca}=1.8, $g_{K_{Ca}}$=4 and p_{ER}=0.00006. Blue solid and green dashed curves represent stable and unstable periodic orbit branches, respectively. Solid aqua and dashed red curves represent stable and unstable equilibrium branches, respectively.

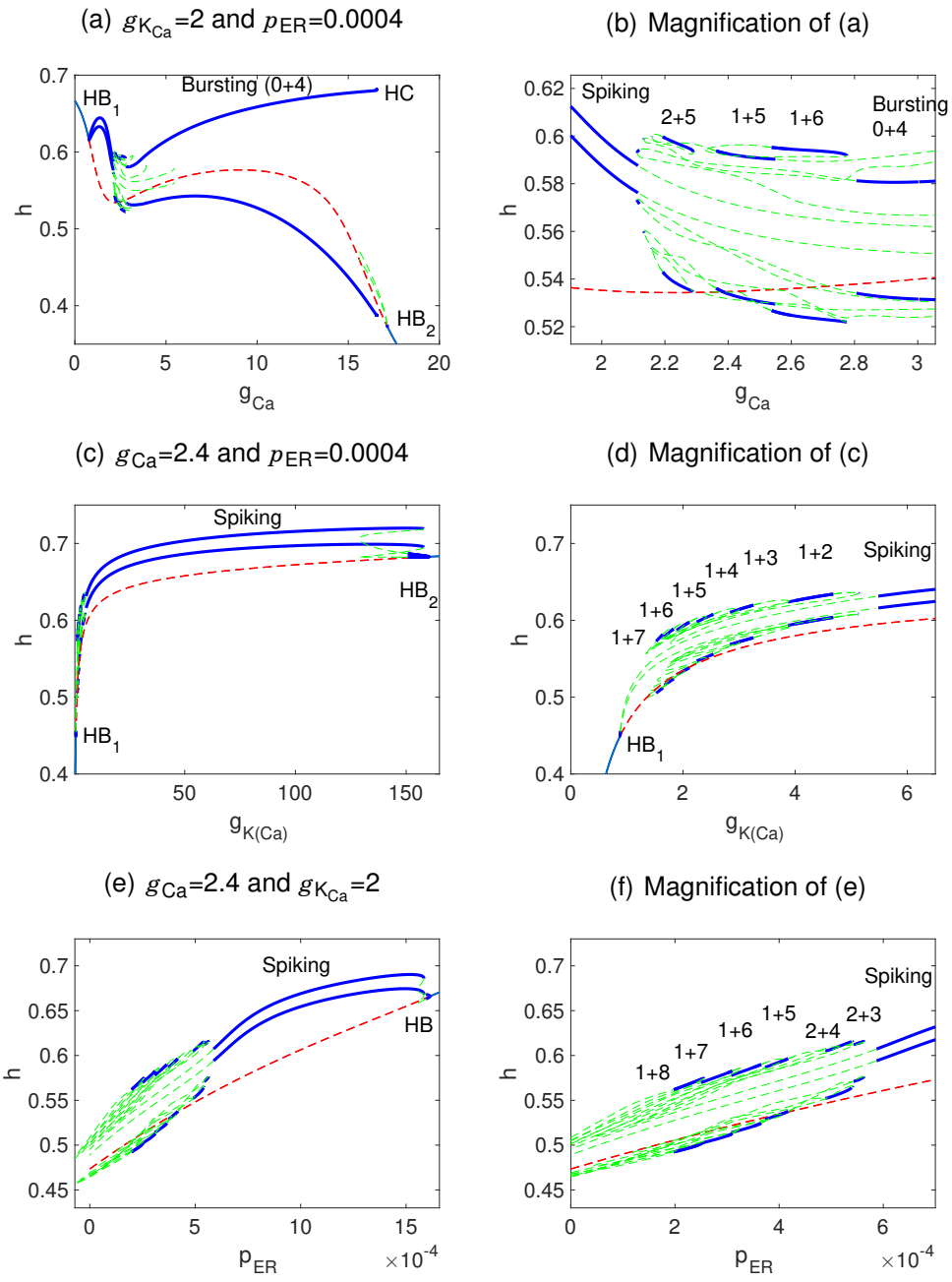

FIGURE A.2. One-parameter bifurcation diagrams. The parameters for the parameter set 2 are g_{Ca}=2.4, $g_{K_{Ca}}$=2 and p_{ER}=0.0004. Blue solid and green dashed curves represent stable and unstable periodic orbit branches, respectively. Solid aqua and dashed red curves represent stable and unstable equilibrium branches, respectively.

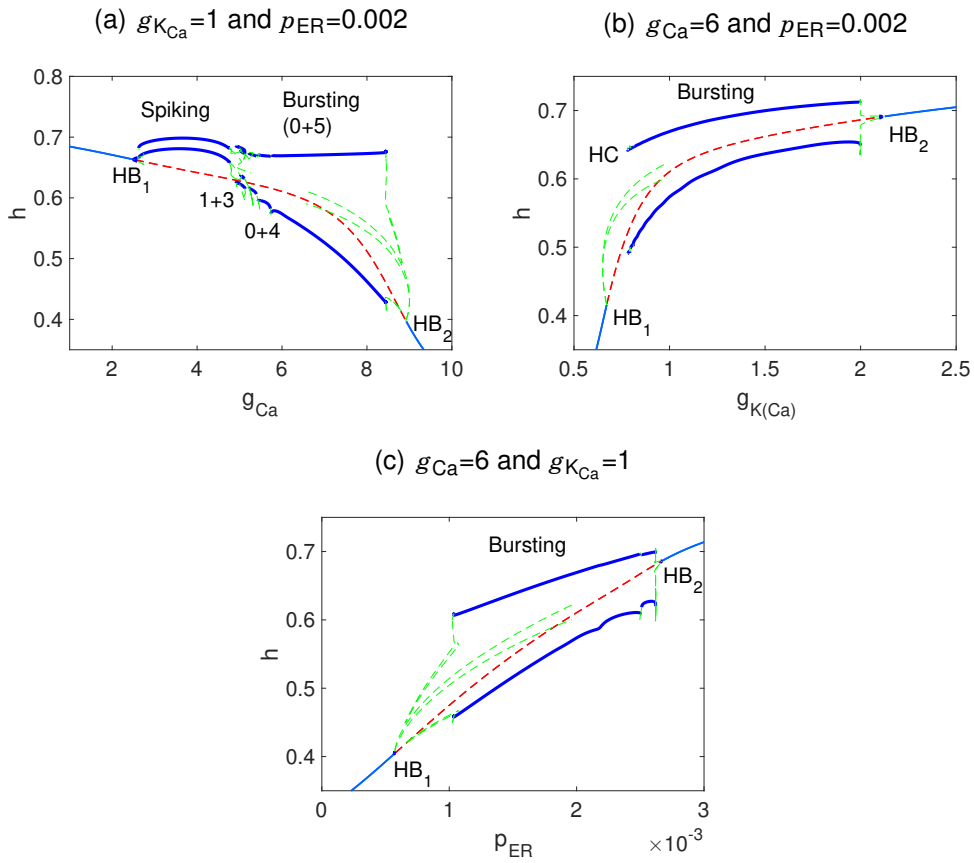

FIGURE A.3. One-parameter bifurcation diagrams. The parameters for the parameter set 3 are g_{Ca}=6, $g_{K_{Ca}}$=1 and p_{ER}=0.002. Blue solid and green dashed curves represent stable and unstable periodic orbit branches, respectively. Solid aqua and dashed red curves represent stable and unstable equilibrium branches, respectively.

h_{Min})/2) of various periodic orbits. Then, we consider the midrange value of all the averages we computed.

The average values for the variable h considering the bifurcation diagrams for the paramater set 1 (g_{Ca}=1.8, $g_{K_{Ca}}$=4 and p_{ER}=0.00006) in Figure A.1, set 2 (g_{Ca}=2.4, $g_{K_{Ca}}$=2 and p_{ER}=0.0004) in Figure A.2 and set 3 (g_{Ca}=6, $g_{K_{Ca}}$=1 and p_{ER}=0.002) in Figure A.3 are calculated as 0.5628, 0.5796 and 0.5774, respectively. Thus, we calculate the average value of these as h=0.5732. This constant value will be used in the reduced IHC model in Chapters 3 and 4.

APPENDIX B

AUTO CONTINUATION

In this chapter, we will give a brief overview of the mathematical formulation of AUTO continuation [18] that we heavily use throughout this thesis.

We will consider the dynamical system in the form of

$$u'(t) = F(u(t), \lambda) \tag{B.1}$$

where $u \in \mathbb{R}^n$, $F : \mathbb{R}^n \to \mathbb{R}^n$ and $\lambda \in \mathbb{R}$.

We would like to compute the *solution branches* of (B.1), which are the solutions of $F(u(t), \lambda) = 0$. A solution (u_0, λ_0) of $F(u(t), \lambda) = 0$ is called *regular* if Rank$[F_u(u_0, \lambda_0)] = n$ i.e. the Jacobian $F_u(u_0, \lambda_0)$ is nonsingular. According to the Implicit Function Theorem (IFT), near the regular solution (u_0, λ_0) there exists a unique solution branch $(u(s), \lambda(s))$ with $(u(0), \lambda(0)) = (u_0, \lambda_0)$.

B.1 Parameter Continuation

Suppose we have a solution u_0 of $F(u, \lambda) = 0$ at λ_0 and its derivative with respect to the parameter λ i.e. $\dot{u}_0 = \frac{du}{d\lambda}$. In order to find the solution u_1 at $\lambda_1 = \lambda_0 + \Delta\lambda$, we use

Newton's method to solve $F(u_1, \lambda_1) = 0$ for u_1,

$$\begin{aligned} F_u(u_1^{(v)}, \lambda_1)\Delta u_1^{(v)} &= -F(u_1^{(v)}, \lambda_1) \\ u_1^{(v+1)} &= u_1^{(v)} + \Delta u_1^{(v)} \quad , \quad v = 0, 1, 2, ... \end{aligned} \tag{B.2}$$

with the initial approximation $u_1^{(0)} = u_0 + \Delta\lambda\dot{u}_0$. The graphical illustration of the parameter continuation is represented in Figure **??**.

The Newton's theory guarantees that this iteration will converge if $F_u(u_1, \lambda_1)$ is nonsingular and $\Delta\lambda$ is sufficiently small [9]. Therefore, the new derivative vector $\dot{u}_1$ can be computed by differentiating $F(u(\lambda), \lambda) = 0$ with respect to λ at $\lambda = \lambda_1$ i.e. by solving

$$F_u(u_1, \lambda_1)\dot{u}_1 = -F_\lambda(u_1, \lambda_1). \tag{B.3}$$

The same procedure is repeated to find u_2, u_3 and so on.

B.2 Pseudo-Arclength Continuation

If there is a fold on the solution branch, then the derivative F_u is singular. Therefore, the continuation method fails and we can no longer apply the parameter continuation. However, AUTO [18] uses a method, called *Keller's pseudo-arclength continuation* [44], which allows us to compute the continuation of solutions passes a fold. The graphical illustration of the pseudo-arclength continuation is represented in Figure **??**.

Unlike the parameter continuation, the bifurcation curve is parameterised by its arc length, s, in pseudo-arclength continuation. Suppose a regular solution (u_0, λ_0) and its derivative vector $(\dot{u}_0, \dot{\lambda}_0)$ are known. Pseudo-arclength continuation consists of solving the following equations for u_1 and λ_1:

$$\begin{aligned} F_u(u_1, \lambda_1) &= 0 \\ (u_1 - u_0)^* \dot{u}_0 + (\lambda_1 - \lambda_0)\dot{\lambda}_0 - \Delta s &= 0 \end{aligned} \tag{B.4}$$

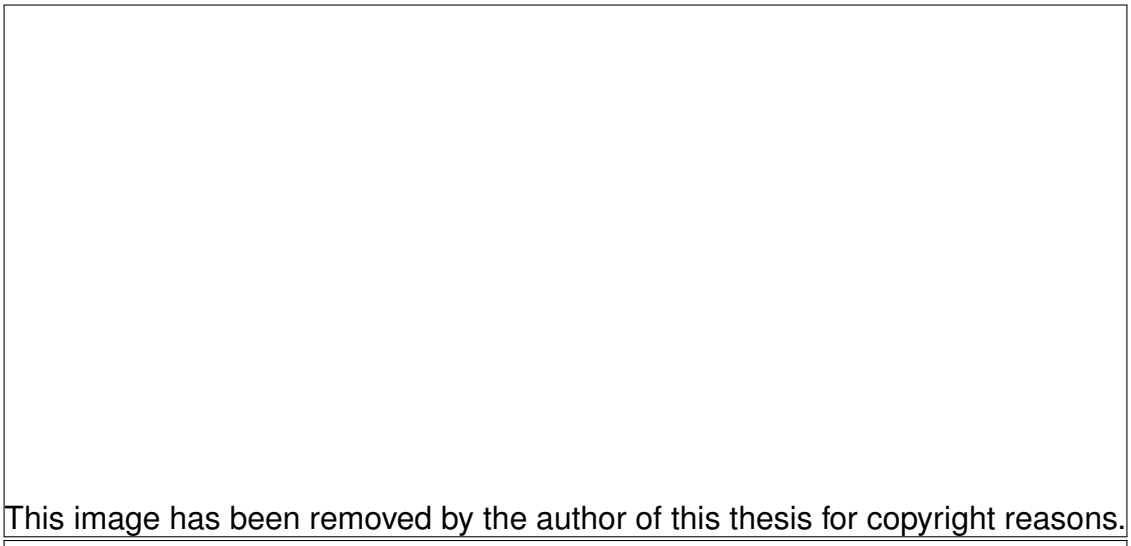

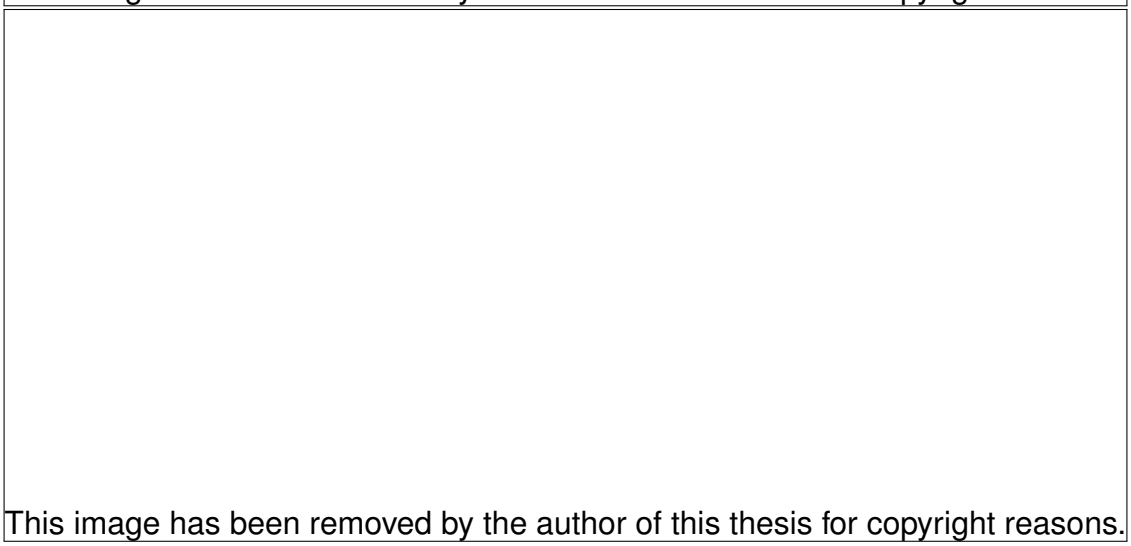

FIGURE B.1. Graphical interpretations of (a) parameter and (b) pseudo-arclength continuations. Images from [70].

Newton's method for solving those equations becomes

$$\begin{pmatrix} (F_u^1)^{(v)} & (F_\lambda^1)^{(v)} \\ \dot{u}_0 & \dot{\lambda}_0 \end{pmatrix} \begin{pmatrix} \Delta u_1^{(v)} \\ \Delta \lambda_1^{(v)} \end{pmatrix} = - \begin{pmatrix} F_u(u_1^{(v)}, \lambda_1^{(v)}) \\ -(u_1^{(v)} - u_0)^* \dot{u}_0 + (\lambda_1^{(v)} - \lambda_0)\dot{\lambda}_0 - \Delta s \end{pmatrix} \tag{B.5}$$

where F_u^1 and F_λ^1 denote the derivative of F with respect to u and λ evaluated at

(u_1, λ_1). After convergence, the new derivative vector can be obtained by solving

$$\begin{pmatrix} F_u^1 & F_\lambda^1 \\ \dot{u}_0 & \dot{\lambda}_0 \end{pmatrix} \begin{pmatrix} \dot{u}_1 \\ \dot{\lambda}_1 \end{pmatrix} = \begin{pmatrix} 0 \\ 1 \end{pmatrix}. \tag{B.6}$$

B.3 Continuation of Periodic Solutions

In this section, we will discuss computing periodic solutions of a dynamical system given in (B.1) and to follow such periodic solutions as the parameter λ varies.

AUTO uses a boundary value approach [70] to compute periodic solutions of a dynamical system. Since the period T of a periodic solution varies as the parameter λ changes, we fix the interval of periodicity by the transformation $t \to t/T$. Then, the equation (B.1) becomes

$$u'(t) = TF(u(t), \lambda). \tag{B.7}$$

where T is one of the unknowns. Now, we investigate solutions of period 1 i.e. $u(0) = u(1)$. However, since u and T are not uniquely specified, a *phase condition* is needed. AUTO uses *integral phase condition* [18], which is a numerically more suitable phase condition [70] given by

$$\int_0^1 u_k(t)^* u'_{k-1}(t) dt = 0. \tag{B.8}$$

By Keller's method, the pseudo-arclength continuation for periodic solutions takes the form

$$\int_0^1 (u_k(t) - u_{k-1}(t))^* u_{k-1}(t) dt + (\lambda_k - \lambda_{k-1})\dot{\lambda}_{k-1} = \Delta s \tag{B.9}$$

To sum up, if u_{k-1}, T_{k-1} and λ_{k-1} are given, AUTO solves the system

$$\begin{aligned} &u_k'(t) = TF(u_k(t), \lambda_k) \\ &u_k(0) = u_k(1) \\ &\int_0^1 u_k(t)^* u_{k-1}'(t) dt = 0 \\ &\int_0^1 (u_k(t) - u_{k-1}(t))^* u_{k-1}(t) dt + (\lambda_k - \lambda_{k-1})\dot{\lambda}_{k-1} = \Delta s \end{aligned} \tag{B.10}$$

where $u, F \in \mathbb{R}^n$ and $\lambda, T \in \mathbb{R}$.

BIBLIOGRAPHY

[1] H. D. ABARBANEL, R. BROWN, J. J. SIDOROWICH, AND L. S. TSIMRING, *The analysis of observed chaotic data in physical systems*, Reviews of Modern Physics, 65 (1993), p. 1331.

[2] J. ARGYRIS, G. FAUST, M. HAASE, AND R. FRIEDRICH, *An Exploration of Dynamical Systems and Chaos: Completely Revised and Enlarged Second Edition*, Springer Berlin Heidelberg, 2015.

[3] I. ATWATER, C. M. DAWSON, A. SCOTT, G. EDDLESTONE, AND E. ROJAS, *The nature of the oscillatory behaviour in electrical activity from pancreatic beta-cell*, Biochemistry Biophysics of the Pancreatic Beta Cell, (1980), pp. 100 – 107.

[4] D. AVITABILE, M. DESROCHES, AND S. RODRIGUES, *On the numerical continuation of isolas of equilibria*, International Journal of Bifurcation and Chaos, 22 (2012), p. 1250277.

[5] S. M. BAER, T. ERNEUX, AND J. RINZEL, *The slow passage through a Hopf bifurcation: delay, memory effects, and resonance*, SIAM Journal on Applied mathematics, 49 (1989), pp. 55–71.

[6] A. BALANOV, N. JANSON, D. POSTNOV, AND O. SOSNOVTSEVA, *Synchronization: From Simple to Complex*, Springer Series in Synergetics, Springer Berlin Heidelberg, 2008.

[7] R. BERTRAM, J. TABAK, W. TEKA, T. VO, M. WECHSELBERGER, V. KIRK, AND A. J. R. SNEYD, *Mathematical Analysis of Complex Cellular Activity*, Springer International Publishing, 2015.

[8] D. BEUTNER AND T. MOSER, *The presynaptic function of mouse cochlear inner hair cells during development of hearing*, Journal of Neuroscience, 21 (2001), pp. 4593–4599.

[9] W.-J. BEYN, A. CHAMPNEYS, E. DOEDEL, W. GOVAERTS, Y. A. KUZNETSOV, AND B. SANDSTEDE, *Numerical continuation, and computation of normal forms*, in In Handbook of Dynamical Systems III: Towards applications, Citeseer, 2001.

[10] A. G. BLANKENSHIP AND M. B. FELLER, *Mechanisms underlying spontaneous patterned activity in developing neural circuits*, Nature Reviews Neuroscience, 11 (2010), pp. 18–29.

[11] G. E. BRIGGS AND J. B. S. HALDANE, *A note on the kinetics of enzyme action*, Biochemical Journal, 19 (1925), pp. 338–339.

[12] M. BRØNS AND K. BAR-ELI, *Canard explosion and excitation in a model of the Belousov-Zhabotinskii reaction*, The Journal of Physical Chemistry, 95 (1991), pp. 8706–8713.

[13] T. R. CHAY AND J. KEIZER, *Minimal model for membrane oscillations in the pancreatic beta-cell.*, Biophysical Journal, 42 (1983), pp. 181–190.

[14] S. G. CLARKE, M. S. SCARNATI, AND K. G. PARADISO, *Neurotransmitter release can be stabilized by a mechanism that prevents voltage changes near the end of action potentials from affecting calcium currents*, Journal of Neuroscience, 36 (2016), pp. 11559–11572.

[15] D. DELLWO, H. B. KELLER, B. J. MATKOWSKY, AND E. L. REISS, *On the birth of isolas*, SIAM Journal on Applied Mathematics, 42 (1982), pp. 956–963.

[16] M. DESROCHES, J. GUCKENHEIMER, B. KRAUSKOPF, C. KUEHN, H. M. OSINGA, AND M. WECHSELBERGER, *Mixed-mode oscillations with multiple time scales*, SIAM Review, 54 (2012), pp. 211–288.

[17] M. DESROCHES, A. GUILLAMON, E. PONCE, R. PROHENS, S. RODRIGUES, AND A. E. TERUEL, *Canards, folded nodes, and mixed-mode oscillations in piecewise-linear slow-fast systems*, SIAM Review, 58 (2016), pp. 653–691.

[18] E. J. DOEDEL, *Auto: A program for the automatic bifurcation analysis of autonomous systems*, Congr. Numer, 30 (1981), pp. 265–284.

[19] R. E. DOLMETSCH, K. XU, AND R. S. LEWIS, *Calcium oscillations increase the efficiency and specificity of gene expression*, Nature, 392 (1998), pp. 933 – 936.

[20] J. P. ECKMANN AND D. RUELLE, *Ergodic theory of chaos and strange attractors*, Springer New York, New York, NY, 2004, pp. 273–312.

[21] C. EGRI AND P. C. RUBEN, *Action potentials: Generation and propagation*, e LS, (2001).

[22] B. ERMENTROUT, *Simulating, Analyzing, and Animating Dynamical Systems: A Guide To XPPAUT for Researchers and Students*, Society for Industrial and Applied Mathematics, Philadelphia, PA, USA, 2002.

[23] N. FENICHEL, *Geometric singular perturbation theory for ordinary differential equations*, Journal of Differential Equations, 31 (1979), pp. 53–98.

[24] E. GLOWATZKI AND P. A. FUCHS, *Cholinergic synaptic inhibition of inner hair cells in the neonatal mammalian cochlea*, Science, 288 (2000), pp. 2366–2368.

[25] L. GRANT AND P. FUCHS, *Calcium- and calmodulin-dependent inactivation of calcium channels in inner hair cells of the rat cochlea*, Journal of Neurophysiology, 99 (2008), pp. 2183–2193.

[26] J. GUCKENHEIMER, *Singular Hopf bifurcation in systems with two slow variables*, SIAM Journal on Applied Dynamical Systems, 7 (2008), pp. 1355–1377.

[27] J. E. HANSEN, L. H. HARTLEY, AND R. HOGAN, *Arterial oxygen increase by high-carbohydrate diet at altitude.*, Journal of Applied Physiology, 33 (1972), pp. 441–445.

[28] R. HEGGER, H. KANTZ, AND T. SCHREIBER, *Practical implementation of nonlinear time series methods: The TISEAN package*, Chaos: An Interdisciplinary Journal of Nonlinear Science, 9 (1999), pp. 413–435.

[29] R. HILBORN, *Chaos and Nonlinear Dynamics: An Introduction for Scientists and Engineers*, Oxford University Press, 1994.

[30] A. L. HODGKIN AND A. F. HUXLEY, *A quantitative description of membrane current and its application to conduction and excitation in nerve*, The Journal of Physiology, 117 (1952), pp. 500–544.

[31] R. IOSUB, D. AVITABILE, L. GRANT, K. TSANEVA-ATANASOVA, AND H. J. KENNEDY, *Calcium-induced calcium release during action potential firing in developing inner hair cells*, Biophysical Journal, 108 (2015), pp. 1003 – 1012.

[32] E. M. IZHIKEVICH, *Neural excitability, spiking and bursting*, International Journal of Bifurcation and Chaos, 10 (2000), pp. 1171–1266.

[33] E. M. IZHIKEVICH, *Dynamical Systems in Neuroscience*, MIT Press, 2007.

[34] S. L. JOHNSON, J. P. ADELMAN, AND W. MARCOTTI, *Genetic deletion of SK2 channels in mouse inner hair cells prevents the developmental linearization in the Ca^{2+} dependence of exocytosis*, The Journal of Physiology, 583 (2007), pp. 631–646.

[35] S. L. JOHNSON, T. ECKRICH, S. KUHN, V. ZAMPINI, C. FRANZ, K. M. RANATUNGA, T. P. ROBERTS, S. MASETTO, M. KNIPPER, C. J. KROS, AND

W. MARCOTTI, *Position-dependent patterning of spontaneous action potentials in immature cochlear inner hair cells*, Nature Neuroscience, 14 (2011), pp. 711 – 717.

[36] S. L. JOHNSON, H. J. KENNEDY, M. C. HOLLEY, R. FETTIPLACE, AND W. MARCOTTI, *The resting transducer current drives spontaneous activity in prehearing mammalian cochlear inner hair cells*, Journal of Neuroscience, 32 (2012), pp. 10479–10483.

[37] S. L. JOHNSON, S. KUHN, C. FRANZ, N. INGHAM, D. N. FURNESS, M. KNIPPER, K. P. STEEL, J. P. ADELMAN, M. C. HOLLEY, AND W. MARCOTTI, *Presynaptic maturation in auditory hair cells requires a critical period of sensory-independent spiking activity*, Proceedings of the National Academy of Sciences, 110 (2013), pp. 8720–8725.

[38] S. L. JOHNSON AND W. MARCOTTI, *Biophysical properties of CaV1.3 calcium channels in gerbil inner hair cells*, The Journal of Physiology, 586 (2008), pp. 1029–1042.

[39] S. L. JOHNSON, W. MARCOTTI, AND C. J. KROS, *Increase in efficiency and reduction in Ca^{2+} dependence of exocytosis during development of mouse inner hair cells*, The Journal of physiology, 563 (2005), pp. 177–191.

[40] T. A. JONES, P. A. LEAKE, R. L. SNYDER, O. STAKHOVSKAYA, AND B. BONHAM, *Spontaneous discharge patterns in cochlear spiral ganglion cells before the onset of hearing in cats*, Journal of Neurophysiology, 98 (2007), pp. 1898–1908.

[41] K. KANDLER, A. CLAUSE, AND J. NOH, *Tonotopic reorganization of developing auditory brainstem circuits*, Nature Neuroscience, 12 (2009), pp. 711–717.

[42] J. L. KAPLAN AND J. A. YORKE, *Chaotic behavior of multidimensional difference equations*, in Functional Differential Equations and Approximation of Fixed Points, Springer Berlin Heidelberg, 1979, pp. 204–227.

[43] J. KEENER AND J. SNEYD, *Mathematical Physiology: I: Cellular Physiology*, Interdisciplinary Applied Mathematics, Springer, 2009.

[44] H. B. KELLER, *Numerical solution of bifurcation and nonlinear eigenvalue problems*, Application of Bifurcation Theory, (1977), pp. 359–384.

[45] H. J. KENNEDY, *New developments in understanding the mechanisms and function of spontaneous electrical activity in the developing mammalian auditory system*, Journal of the Association for Research in Otolaryngology, 13 (2012), pp. 437–445.

[46] H. J. KENNEDY AND R. W. MEECH, *Fast Ca^{2+} signals at mouse inner hair cell synapse: a role for Ca^{2+}-induced Ca^{2+} release*, The Journal of Physiology, 539 (2002), pp. 15–23.

[47] C. KENNETH, C. ELLIS, AND M. MARIO, *Differential Equations And Applications To Biology And To Industry - Proceedings Of The Claremont International Conference Dedicated To The Memory Of Starvros Busenberg (1941 - 1993)*, World Scientific Publishing Company, 1995.

[48] M. T. KOPER, *Bifurcations of mixed-mode oscillations in a three-variable autonomous Van der Pol-Duffing model with a cross-shaped phase diagram*, Physica D: Nonlinear Phenomena, 80 (1995), pp. 72–94.

[49] C. KROS, J. P. RUPPERSBERG, AND A. RÜSCH, *Expression of a potassium current in inner hair cells during development of hearing in mice*, Nature, 394 (1998), pp. 281–284.

[50] C. J. KROS, *How to build an inner hair cell: challenges for regeneration*, Hearing Research, 227 (2007), pp. 3–10.

[51] M. KRUPA, N. POPOVIĆ, AND N. KOPELL, *Mixed-mode oscillations in three time-scale systems: a prototypical example*, SIAM Journal on Applied Dynamical Systems, 7 (2008), pp. 361–420.

[52] C. KUEHN, *Multiple Time Scale Dynamics*, Applied Mathematical Sciences, Springer International Publishing, 2015.

[53] Y. KUZNETSOV, *Elements of Applied Bifurcation Theory*, Applied Mathematical Sciences, Springer New York, 2004.

[54] Y. A. KUZNETSOV, H. G. MEIJER, AND L. VAN VEEN, *The fold-flip bifurcation*, International Journal of Bifurcation and Chaos, 14 (2004), pp. 2253–2282.

[55] R. N. LEÃO, M. M. NAVES, K. E. LEÃO, AND B. WALMSLEY, *Altered sodium currents in auditory neurons of congenitally deaf mice*, European Journal of Neuroscience, 24 (2006), pp. 1137–1146.

[56] R. N. LEAO, H. SUN, K. SVAHN, A. BERNTSON, M. YOUSSOUFIAN, A. G. PAOLINI, R. E. FYFFE, AND B. WALMSLEY, *Topographic organization in the auditory brainstem of juvenile mice is disrupted in congenital deafness*, The Journal of Physiology, 571 (2006), pp. 563–578.

[57] F. LEDRAPPIER AND L.-S. YOUNG, *Dimension formula for random transformations*, Communications in Mathematical Physics, 117 (1988), pp. 529–548.

[58] C. LI, M. DONIZELLI, N. RODRIGUEZ, H. DHARURI, L. ENDLER, V. CHELLIAH, L. LI, E. HE, A. HENRY, M. I. STEFAN, ET AL., *Biomodels database: An enhanced, curated and annotated resource for published quantitative kinetic models*, BMC Systems Biology, 4 (2010), p. 92.

[59] W. LIEBERT AND H. SCHUSTER, *Proper choice of the time delay for the analysis of chaotic time series*, Physics Letters A, 142 (1989), pp. 107–111.

[60] H.-G. MA AND C.-Z. HAN, *Selection of embedding dimension and delay time in phase space reconstruction*, Frontiers of Electrical and Electronic Engineering in China, 1 (2006), pp. 111–114.

[61] W. MARCOTTI, S. L. JOHNSON, M. C. HOLLEY, AND C. KROS, *Developmental changes in the expression of potassium currents of embryonic, neonatal*

and mature mouse inner hair cells, The Journal of Physiology, 548 (2003), pp. 383–400.

[62] W. MARCOTTI, S. L. JOHNSON, AND C. KROS, *A transiently expressed SK current sustains and modulates action potential activity in immature mouse inner hair cells*, The Journal of Physiology, 560 (2004), pp. 691–708.

[63] W. MARCOTTI, S. L. JOHNSON, A. RÜSCH, AND C. KROS, *Sodium and calcium currents shape action potentials in immature mouse inner hair cells*, The Journal of Physiology, 552 (2003), pp. 743–761.

[64] A. MEDIO AND G. GALLO, *Chaotic dynamics: Theory and applications to economics*, Cambridge University Press, 1995.

[65] R. M. MIURA, *Analysis of excitable cell models*, Journal of Computational and Applied Mathematics, 144 (2002), pp. 29 – 47.

[66] S. P. MOSTAFAPOUR, S. L. COCHRAN, N. M. DEL PUERTO, AND E. W. RUBEL, *Patterns of cell death in mouse anteroventral cochlear nucleus neurons after unilateral cochlea removal*, Journal of Comparative Neurology, 426 (2000), pp. 561–571.

[67] J. MURRAY, *Mathematical Biology: I. An Introduction*, Interdisciplinary Applied Mathematics, Springer New York, 2002.

[68] H. NAGASHIMA AND Y. BABA, *Introduction to Chaos: Physics and Mathematics of Chaotic Phenomena*, CRC Press, 1998.

[69] P. NAN, Y. WANG, V. KIRK, AND J. E. RUBIN, *Understanding and distinguishing three-time-scale oscillations: Case study in a coupled Morris–Lecar system*, SIAM Journal on Applied Dynamical Systems, 14 (2015), pp. 1518–1557.

[70] H. OSINGA AND J. G.-V. B. KRAUSKOPF, *Numerical Continuation Methods for Dynamical Systems*, Springer, 2007.

[71] H. M. OSINGA AND K. T. TSANEVA-ATANASOVA, *Dynamics of plateau bursting depending on the location of its equilibrium*, Journal of Neuroendocrinology, 22 (2010), pp. 1301–1314.

[72] J. PICKLES, *An Introduction to the Physiology of Hearing*, Emerald, 2012.

[73] R. PLANT, *The effects of calcium++ on bursting neurons. a modeling study*, Biophysical Journal, 21 (1978), pp. 217 – 237.

[74] R. E. PLANT, *Bifurcation and resonance in a model for bursting nerve cells*, Journal of Mathematical Biology, 11 (1981), pp. 15–32.

[75] J. PLATZER, J. ENGEL, A. SCHROTT-FISCHER, K. STEPHAN, S. BOVA, H. CHEN, H. ZHENG, AND J. STRIESSNIG, *Congenital deafness and sinoatrial node dysfunction in mice lacking class D L-type Ca^{2+} channels*, Cell, 102 (2000), pp. 89 – 97.

[76] D. PURVES, D. FITZPATRICK, L. KATZ, A. LAMANTIA, J. MCNAMARA, S. WILLIAMS, AND G. AUGUSTINE, *Neuroscience*, Sinauer Associates, 2001.

[77] K. RENNIE, K. MANNING, AND A. RICCI, *Mechano-electrical transduction in the turtle utricle.*, Biomedical Sciences Instrumentation, 40 (2004), pp. 441–446.

[78] J. RINZEL, *Bursting oscillations in an excitable membrane model*, Springer Berlin Heidelberg, Berlin, Heidelberg, 1985, pp. 304–316.

[79] J. RINZEL, *A Formal Classification of Bursting Mechanisms in Excitable Systems*, Springer Berlin Heidelberg, Berlin, Heidelberg, 1987, pp. 267–281.

[80] J. RINZEL AND Y. S. LEE, *On Different Mechanisms for Membrane Potential Bursting*, Springer Berlin Heidelberg, Berlin, Heidelberg, 1986, pp. 19–33.

[81] R. ROMAND AND I. VARELA-NIETO, *Development of Auditory and Vestibular Systems*, Elsevier Science, 2014.

[82] D. H. ROTHMAN, *Nonlinear dynamics 1: Chaos*, Fall 2006. Massachusetts Institute of Technology: MIT OpenCourseWare.

[83] I. ROUX, E. WERSINGER, J. M. MCINTOSH, P. A. FUCHS, AND E. GLOWATZKI, *Onset of cholinergic efferent synaptic function in sensory hair cells of the rat cochlea*, Journal of Neuroscience, 31 (2011), pp. 15092–15101.

[84] J. SNEYD, *An Introduction to Mathematical Modeling in Physiology, Cell Biology, and Immunology*, American Mathematical Society, 2002.

[85] T. J. SNOWDEN, P. H. VAN DER GRAAF, AND M. J. TINDALL, *Methods of model reduction for large-scale biological systems: A survey of current methods and trends*, Bulletin of Mathematical Biology, 79 (2017), pp. 1449–1486.

[86] N. C. SPITZER, N. J. LAUTERMILCH, R. D. SMITH, AND T. M. GOMEZ, *Coding of neuronal differentiation by calcium transients*, BioEssays, 22 (2000), pp. 811–817.

[87] J. V. STERN, H. M. OSINGA, A. LEBEAU, AND A. SHERMAN, *Resetting behavior in a model of bursting in secretory pituitary cells: distinguishing plateaus from pseudo-plateaus*, Bulletin of Mathematical Biology, 70 (2008), pp. 68–88.

[88] C. STEVE AND B. PAUL, *Bursting: The Genesis Of Rhythm In The Nervous System*, World Scientific Publishing Company, 2005.

[89] S. STROGATZ, *Nonlinear Dynamics And Chaos*, Studies in Nonlinearity, Sarat Book House, 2007.

[90] R. SZALAI, K. TSANEVA-ATANASOVA, M. E. HOMER, A. R. CHAMPNEYS, H. J. KENNEDY, AND N. P. COOPER, *Nonlinear models of development, amplification and compression in the mammalian cochlea*, Philosophical Transactions of the Royal Society of London A: Mathematical, Physical and Engineering Sciences, 369 (2011), pp. 4183–4204.

[91] J. TABAK, N. TOPORIKOVA, M. E. FREEMAN, AND R. BERTRAM, *Low dose of dopamine may stimulate prolactin secretion by increasing fast potassium currents*, Journal of Computational Neuroscience, 22 (2007), pp. 211–222.

[92] W. TEKA, *Nonlinear Dynamics Underlying Fast Bursting in Pituitary Cells*, PhD thesis, Florida State University, 2012.

[93] W. TEKA, J. TABAK, T. VO, M. WECHSELBERGER, AND R. BERTRAM, *The dynamics underlying pseudo-plateau bursting in a pituitary cell model*, The Journal of Mathematical Neuroscience, 1 (2011), p. 12.

[94] W. TEKA, K. TSANEVA-ATANASOVA, R. BERTRAM, AND J. TABAK, *From plateau to pseudo-plateau bursting: Making the transition*, Bulletin of Mathematical Biology, 73 (2011), pp. 1292–1311.

[95] V. THIERRY, *Handbook of Mathematics*, HDBoM, 2017.

[96] T. S. TIERNEY, F. A. RUSSELL, AND D. R. MOORE, *Susceptibility of developing cochlear nucleus neurons to deafferentation-induced death abruptly ends just before the onset of hearing*, Journal of Comparative Neurology, 378 (1997), pp. 295–306.

[97] N. X. TRITSCH, A. RODRÍGUEZ-CONTRERAS, T. T. CRINS, H. C. WANG, J. G. G. BORST, AND D. E. BERGLES, *Calcium action potentials in hair cells pattern auditory neuron activity before hearing onset*, Nature neuroscience, 13 (2010), pp. 1050–1052.

[98] N. X. TRITSCH, E. YI, J. E. GALE, E. GLOWATZKI, AND D. E. BERGLES, *The origin of spontaneous activity in the developing auditory system*, Nature, 450 (2007), pp. 50–55.

[99] K. TSANEVA-ATANASOVA, H. M. OSINGA, T. RIEβ, AND A. SHERMAN, *Full system bifurcation analysis of endocrine bursting models*, Journal of Theoretical Biology, 264 (2010), pp. 1133–1146.

[100] T. VO, *Geometric singular perturbation analysis of mixed-mode dynamics in pituitary cells*, PhD thesis, University of Sydney, 2014.

[101] T. VO, R. BERTRAM, AND M. WECHSELBERGER, *Multiple geometric viewpoints of mixed mode dynamics associated with pseudo-plateau bursting*, SIAM Journal on Applied Dynamical Systems, 12 (2013), pp. 789–830.

[102] H. C. WANG, C.-C. LIN, R. CHEUNG, Y. ZHANG-HOOKS, A. AGARWAL, G. ELLIS-DAVIES, J. ROCK, AND D. E. BERGLES, *Spontaneous activity of cochlear hair cells triggered by fluid secretion mechanism in adjacent support cells*, Cell, 163 (2015), pp. 1348–1359.

[103] T. WANG, *Studies on the Action Potential From a Thermodynamic Perspective*, PhD thesis, University of Copenhagen, 2017.

[104] R. WEGENKITTL, H. LOFFELMANN, AND E. GROLLER, *Visualizing the behaviour of higher dimensional dynamical systems*, in Visualization'97., Proceedings, IEEE, 1997, pp. 119–125.

[105] C. WICHMANN AND T. MOSER, *Relating structure and function of inner hair cell ribbon synapses*, Cell and Tissue Research, 361 (2015), pp. 95–114.

[106] A. WOLF, J. B. SWIFT, H. L. SWINNEY, AND J. A. VASTANO, *Determining Lyapunov exponents from a time series*, Physica D: Nonlinear Phenomena, 16 (1985), pp. 285–317.

[107] L. S. YOUNG, *Dimension, entropy and Lyapunov exponents*, Ergodic Theory and Dynamical Systems, 2 (1982), pp. 109–124.

[108] V. ZAMPINI, S. L. JOHNSON, C. FRANZ, N. D. LAWRENCE, S. MÜNKNER, J. ENGEL, M. KNIPPER, J. MAGISTRETTI, S. MASETTO, AND W. MARCOTTI, *Elementary properties of CaV1.3 Ca^{2+} channels expressed in mouse cochlear inner hair cells*, The Journal of Physiology, 588 (2010), pp. 187–199.